# Reconstruction of temperature, accumulation rate, and layer thinning from an ice core at South Pole using a statistical inverse method

Emma C. Kahle[1,1,1], Eric J. Steig[1,1,1], Tyler R. Jones[2,2,2], T.J. Fudge[1,1,1], Michelle Rebecca Koutnik[1,1,1], Valerie Morris[2,2,2], Bruce Vaughn[2,2,2], Andrew Schauer[1,1,1], C. Max Stevens[3,3,3], Howard Conway[1,1,1], Edwin D Waddington[1,1,1], Christo Buizert[4,4,4], Jenna Epifanio[4,4,4], and James W.C. White[2,2,2]

[1]University of Washington
[2]University of Colorado Boulder
[3]University of Washignton
[4]Oregon State University

November 30, 2022

**Abstract**

Data from the South Pole ice core (SPC14) are used to constrain climate conditions and ice-flow-induced layer thinning for the last 54,000 years. Empirical constraints are obtained from the SPC14 ice and gas timescales, used to calculate annual-layer thickness and the gas-ice age difference (Δage), and from high-resolution measurements of water isotopes, used to calculate the water-isotope diffusion length. Both Δage and diffusion length depend on firn properties and therefore contain information about past temperature and snow-accumulation rate. A statistical inverse approach is used to obtain an ensemble of reconstructions of temperature, accumulation-rate, and thinning of annual layers in the ice sheet at the SPC14 site. The traditional water-isotope/temperature relationship is not used as a constraint; the results therefore provide an independent calibration of that relationship. The temperature reconstruction yields a glacial-interglacial temperature change of 6.7 ± 1.0 °C at the South Pole. The sensitivity of δ180 to temperature is 0.99 ± 0.03 significantly greater than the spatial slope of ˜0.8 East Antarctic ice core records. The reconstructions of accumulation rate and ice thinning show millennial-scale variations in the thinning function as well as decreased thinning at depth compared to the results of a 1-D ice flow model, suggesting influence of bedrock topography on ice flow.

# Reconstruction of temperature, accumulation rate, and layer thinning from an ice core at South Pole, using a statistical inverse method

**Emma C. Kahle[1], Eric J. Steig[1], Tyler R. Jones[2], T.J. Fudge[1], Michelle R. Koutnik[1], Valerie A. Morris[2], Bruce H. Vaughn[2], Andrew J. Schauer[1], C. Max Stevens[1], Howard Conway[1], Edwin D. Waddington[1], Christo Buizert[3], Jenna Epifanio[3], James W. C. White[2]**

[1]Department of Earth and Space Sciences, University of Washington, Seattle WA 98195, USA
[2]Institute of Arctic and Alpine Research, University of Colorado, Boulder CO 80309, USA
[3]College of Earth Ocean and Atmospheric Sciences, Oregon State University, Corvallis OR 97331, USA

**Key Points:**

- An inverse method using a firn model with isotope diffusion provides self-consistent temperature, accumulation rate, and thinning histories.
- Glacial-interglacial temperature change at the South Pole was 6.7 +/- 1.0 K. The d18O/T sensitivity is 0.99 +/- 0.03 permille/K.
- Reconstruction of ice thinning shows millennial-scale variations in thinning function and decreased thinning at depth compared to 1-D model.

Corresponding author: Emma C. Kahle, `eckahle@uw.edu`

## Abstract

Data from the South Pole ice core (SPC14) are used to constrain climate conditions and ice-flow-induced layer thinning for the last 54,000 years. Empirical constraints are obtained from the SPC14 ice and gas timescales, used to calculate annual-layer thickness and the gas-ice age difference ($\Delta$age), and from high-resolution measurements of water isotopes, used to calculate the water-isotope diffusion length. Both $\Delta$age and diffusion length depend on firn properties and therefore contain information about past temperature and snow-accumulation rate. A statistical inverse approach is used to obtain an ensemble of reconstructions of temperature, accumulation-rate, and thinning of annual layers in the ice sheet at the SPC14 site. The traditional water-isotope/temperature relationship is not used as a constraint; the results therefore provide an independent calibration of that relationship. The temperature reconstruction yields a glacial-interglacial temperature change of 6.7±1.0°C at the South Pole. The sensitivity of $\delta^{18}0$ to temperature is 0.99±0.03‰°C$^{-1}$, significantly greater than the spatial slope of 0.8‰°C$^{-1}$ that has been used previously to determine temperature changes from East Antarctic ice core records. The reconstructions of accumulation rate and ice thinning show millennial-scale variations in the thinning function as well as decreased thinning at depth compared to the results of a 1-D ice flow model, suggesting influence of bedrock topography on ice flow.


## 1 Introduction

Ice cores from polar ice sheets provide important records of past changes in climate and ice dynamics. Temperature and snow-accumulation rate are critical targets for reconstruction from ice-core data (Lorius et al., 1990). The traditional approach to reconstructing temperature is the use of water isotope ratios ($\delta^{18}$O, $\delta$D), calibrated using empirical relationships (Dansgaard, 1964; Jouzel et al., 1993). Another approach is borehole thermometry, which provides a direct measurement of the modern temperature profile of the ice sheet that can be related to surface temperature history through a heat advection-diffusion model (Cuffey et al., 1995; Dahl-Jensen et al., 1998). Finally, measurements of $\delta^{15}$N of $N_2$ in trapped air bubbles provide information about the thickness of the firn layer and past abrupt temperature changes that produce thermal gradients (Sowers et al., 1992; Schwander, 1989; Severinghaus et al., 1998). Because firn thickness is a function of accumulation rate and temperature, $\delta^{15}$N can be used to provide constraints on both variables through modeling of the firn densification process (Huber et al., 2006; Guillevic et al., 2013; Kindler et al., 2014). With independent constraints on the ice-core depth-age relationship, in particular from annual-layer counting, these approaches can be combined to produce robust estimates of temperature and accumulation rate through time. Results from Greenland (Buizert et al., 2014) and the West Antarctic Ice Sheet (WAIS) Divide ice core (Cuffey et al., 2016) provide recent examples.

In comparison with locations in West Antarctica and Greenland, ice-core sites in East Antarctica pose special challenges. The low accumulation rates typical of the East Antarctic plateau are less favorable for borehole thermometry; high accumulation rates and locations near ice divides, where horizontal velocities are low, are generally necessary for preservation of detectable thermal anomalies. Additionally, some recent studies have questioned the validity of firn models at the typically very cold temperatures during the glacial period in East Antarctica (Freitag et al., 2013; Bréant et al., 2017), since many of the models are calibrated with or designed for warmer conditions. One approach that may help to address such challenges is to use the "diffusion length," a measure of the spectral properties of high-depth-resolution measurements of water-isotope ratios. Water-isotope diffusion length reflects the vertical diffusion experienced by water molecules through the firn column (Johnsen, 1977; Whillans and Grootes, 1985; Cuffey and Steig, 1998; Johnsen et al., 2000). While diffusion length has primarily been used as a proxy for temperature (e.g., Simonsen et al., 2011; Gkinis et al., 2014; van der Wel et al., 2015; Holme et al., 2018; Gkinis et al., 2021), it is sensitive to both temperature and accumulation rate through their influence on the firn density profile and tortuosity, and is also affected by vertical strain (Gkinis et al., 2014; Jones et al., 2017a). Diffusion length thus provides an independent constraint on several important ice-core properties: temperature, accumulation rate, and the thinning history due to ice deformation.

Here, we present data from a new ice core (SPC14) from the South Pole, East Antarctica, and we use a novel approach to combine multiple data sets to constrain temperature, accumulation-rate, and ice-thinning histories. We take advantage of two timescales for SPC14, one for the ice (Winski et al., 2019) and one for the gas enclosed within it (Epifanio et al., 2020), to obtain an empirical measure of the gas-age ice-age difference ($\Delta$age). We also use high-resolution measurements of $\delta^{17}$O, $\delta^{18}$O, and $\delta$D of ice (Steig et al., 2021) to obtain water-isotope diffusion lengths.

We use a statistical inverse approach to obtain optimized, self-consistent reconstructions of temperature and accumulation rate using a combined firn-densification and water-isotope diffusion model. We exclude gas isotope ($\delta^{15}$N) data and use the water-isotope values only for calculating diffusion length, reserving these variables for comparison and validation. This approach allows us to produce a novel and independent calibration of the traditional isotope paleothermometer without the use of borehole thermometry. We also obtain an independent constraint on the thinning of annual layers. This is important at South Pole because the location of the site is about 200 km from the ice divide and the ice-flow history is not well known at ages earlier than the Holocene (Lilien et al., 2018).

## 2 Data from the South Pole Ice Core

The South Pole Ice Core (SPC14) was obtained from 2014 to 2016 at 89.9889°S, 98.1596°W, approximately 2 km from the geographic South Pole. SPC14 was drilled to a depth of 1751 m, equivalent to an age of approximately 54 ka (Winski et al., 2019). Compared to other East Antarctic plateau ice-core sites, South Pole has a relatively high annual accumulation rate (8 cm w.e. a$^{-1}$) (Casey et al., 2014) given its low mean-annual air temperature of -49°C (Lazzara et al., 2012). The mean firn temperature is -51°C (Severinghaus et al., 2001). The modern surface ice velocity is 10 m a$^{-1}$ (Casey et al., 2014).

The data sets used in our analysis are developed from the independent ice and gas timescales for SPC14 described previously by Winski et al. (2019) and Epifanio et al. (2020), respectively, and water-isotope measurements obtained at high depth resolution by continuous-flow analysis, as described in Steig et al. (2021). We briefly summarize the information obtained directly from the ice-core measurements as well as the data sets derived from that information (annual-layer thickness, $\Delta$age, and water-isotope diffusion length).

### 2.1 Ice Timescale and Annual-Layer Thickness

The SP19 ice timescale was constructed by stratigraphic matching of 251 volcanic tie points between SPC14 and WAIS Divide (Winski et al., 2019). Between tie points, identification of individual layers from seasonal cycles in sodium and magnesium ions was used to produce an annually-resolved timescale for most of the Holocene. For ages greater than 11.3 ka, despite lack of annual resolution, the uncertainty of the timescale is estimated to be within 124 years relative to WD2014 (Winski et al., 2019). Annual-layer thickness is given by the depth between successive years on the SP19 timescale. For ages older than 11.3 ka where annual layers could not be identified, Winski et al. (2019) found the smoothest annual-layer thickness which matched 95% of the volcanic tie points to within one year. Based on the uncertainty associated with interpolation between sparse tie points (Fudge et al., 2014), we estimate the uncertainty in annual-layer thickness (two standard deviations, hereafter s.d.) to be $\pm$3% of the value in the Holocene, increasing to $\pm$10% of the value at earlier ages.

## 2.2 Gas Timescale and Δage

Epifano et al. (2020) developed the SPC14 gas timescale through stratigraphic matching of features in the high-resolution $CH_4$ records of the SPC14 and WAIS Divide cores. The difference in age between the ice and gas timescales, Δage, is a measure of the ice age at the lock-in depth, which depends on the rate of firn densification (Schwander and Stauffer, 1984; Schwander et al., 1988; Blunier and Schwander, 2000). Epifanio et al. (2020) determined Δage empirically at each of the $CH_4$ tie points and used a cubic spline fit to derive a continuous Δage curve for all depths. Due to the empirical nature of the gas timescale, the SPC14 Δage record is determined without the use of a firn-densification model. Moreover, the SPC14 Δage was obtained without relying on the additional constraint of $\delta^{15}$N to determine lock-in depth.

We assign an age to each empirical Δage estimate as the mid-point between the gas-age and ice-age timescales from which Δage is calculated. This approximation is justified by results from a dynamic densification model (Stevens et al., 2020), which show that at a site like South Pole the timescale on which Δage responds to climate variations is a time interval shorter than Δage itself. Uncertainty in Δage depends on uncertainty in the match between the WAIS Divide and SPC14 gas timescales, the uncertainty associated with interpolation between tie points, and uncertainty in the Δage for WAIS Divide. Because Δage is an order of magnitude smaller at WAIS Divide than at South Pole, that source of uncertainty is the smallest. The uncertainty estimated by Epifanio et al. (2020) ranges from ±1% to ±8% (two s.d.) of the value of Δage.

## 2.3 Water-Isotope Measurements and Diffusion Length

We measured water-isotope ratios at an effective resolution of 0.5 cm using continuous flow analysis (CFA), following the methods described in Jones et al. (2017b) and Steig et al. (2021). We measured $\delta^{18}$O and $\delta$D for the entirety of the core and $\delta^{17}$O from a depth of 556 m through the bottom of the core. We used Picarro Inc. cavity ring-down laser spectroscopy (CRDS) instruments, including both a model L2130-i (for $\delta^{18}$O and $\delta$D) and a model L2140-i for $\delta^{17}$O (Steig et al., 2014). We use the standard notation for $\delta^{18}$O:

$$\delta^{18}O_{sample} = \left(\frac{^{18}O}{^{16}O}\right)_{sample} \Big/ \left(\frac{^{18}O}{^{16}O}\right)_{VSMOW} - 1,$$

where VSMOW is Vienna Standard Mean Ocean Water. $\delta^{17}$O and $\delta$D are defined similarly. These measurements were used to calculate the water-isotope diffusion length. Figure 1 shows the $\delta^{18}$O measurements at 100-year-mean resolution as a function of age.

After deposition as snow on the ice-sheet surface, water isotopologues diffuse through interconnected air pathways among ice grains in the firn, driven by isotope-concentration gradients in the vapor phase (Johnsen, 1977; Whillans and Grootes, 1985; Cuffey and Steig, 1998). In solid ice below the firn column, diffusion continues, but at a rate orders of magnitude slower than in the firn (Johnsen et al., 2000). The extent of diffusion is quantified as the diffusion length, the mean cumulative diffusive-displacement in the vertical direction of water molecules relative to their original location in the firn.

Diffusion length is determined from spectral analysis of the high-resolution water-isotope data, following the methods described in Kahle et al. (2018). We use discrete data sections of 250 years. We calculate the diffusion length, $\sigma$, for each section by fitting its power spectrum with a model of a diffused power spectrum and a two-component model of the measurement system noise:

$$P = P_0 \exp(-k^2\sigma^2) + P_0' \exp(-k^2(\sigma')^2) + |\hat{\eta}|^2, \tag{1}$$

where $k$ is the wavenumber, $|\hat{\eta}|^2$ is the measurement noise, and $P_0$, $P_0'$, and $\sigma'$ are variable fitting parameters. The second term ($P_0' \exp(-k^2(\sigma')^2)$) accounts for the influence

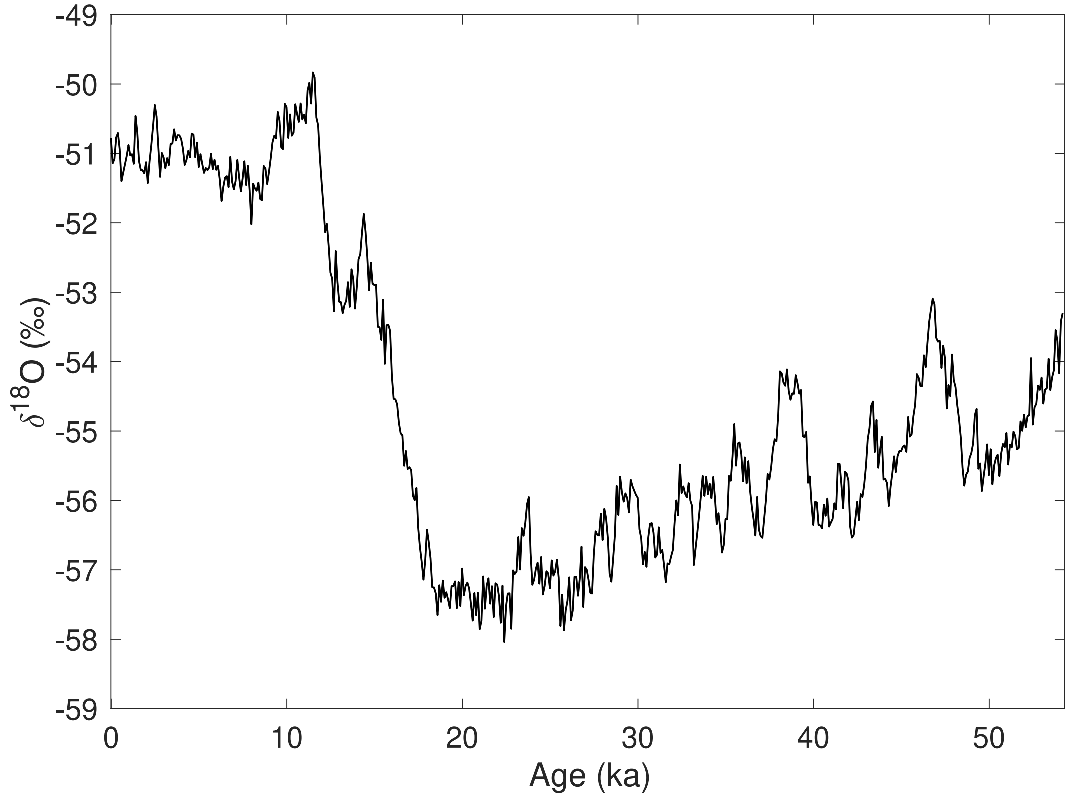


Figure 1: High-resolution $\delta^{18}$O record (Steig et al., 2021) from the South Pole ice core (SPC14), shown as discrete 100-year averages for clarity, on the SP19 ice timescale (Winski et al., 2019).

of the CFA measurement system on the water-isotope data spectrum. Kahle et al. (2018) found that this term does not completely eliminate the effect of system smoothing on the spectrum; we therefore make an additional correction, based on the sequential measurement of ice standards of known and differing isotopic composition, following Jones et al. (2017b). This correction is small, accounting for only $\sim$4% of the total diffusion length throughout the core. The uncertainty on $\sigma$ is estimated conservatively as described in Kahle et al. (2018) and varies from $\pm$4% to $\pm$66% (two s.d.) of the value throughout the core.

Additionally, we correct the diffusion-length estimates to account for diffusion in the solid ice, following Gkinis et al. (2014). This effect is also small, accounting for a maximum of 4% of the total diffusion length at the bottom of the core. To calculate the solid-ice diffusion length, we assume the modern borehole temperature profile $T(z)$ remains constant through time to find the diffusivity profile $D_{ice}(z)$, following Gkinis et al. (2014). We use borehole temperature measurements from the nearby neutrino observatory (Price et al., 2002). We assume a simple thinning function from a 1-D ice-flow model (Dansgaard and Johnsen, 1969) with a kink-height $h_0 = 0.2$ for this calculation; the error in this assumption is negligible for the small deviations in total thinning we are calculating. We subtract both the solid-ice and CFA diffusion lengths from the observations in quadrature to produce our final diffusion-length data set. Further details on both corrections are provided in the Supporting Information, Section S1.1.

We calculate the diffusion length for each of the three water-isotope ratios measured on the core. To combine the information from each isotope, we convert $\delta^{17}$O and $\delta$D diffusion lengths to equivalent values for $\delta^{18}$O. For example, the $\delta^{18}$O-equivalent diffusion length ($\sigma_{18\,from\,17}$) from the $\delta^{17}$O diffusion length ($\sigma_{17}$) is:

$$\sigma^2_{18\,from\,17} = \sigma^2_{17}\ \frac{D_{18}}{\alpha_{18}} \Big/ \frac{D_{17}}{\alpha_{17}}, \tag{2}$$

where $D$ and $\alpha$ are the corresponding air diffusivity and solid-vapor fractionation factor for each isotope. Values for $D$ and $\alpha$ are given in the Supporting Information, Section S1.2 (Majoube, 1970; Barkan and Luz, 2007; Luz and Barkan, 2010; Lamb et al., 2017). For the single diffusion-length record used in our analysis, we take the mean of these three estimates for $\sigma_{18}$.

## 3 Forward Model

We use a forward model to relate the observational data sets to the variables of interest. Figure 2 summarizes the data sets obtained from the ice-core measurements and the calculations described above: $\Delta$age, water-isotope diffusion length, and annual-layer thickness. We use these three data sets as our "observations" in a statistical inverse approach to infer temperature, accumulation rate, and ice-thinning function.

Figure 3 illustrates the structure of the forward model, including a firn-densification component, a water-isotope diffusion component, and a vertical strain (ice thinning) component. We describe the individual components below.

### 3.1 Firn Densification

The firn layer comprises the upper few tens of meters of the ice sheet where snow is progressively densifying into solid ice. As successive layers of snow fall on the surface of the ice sheet, the increase in overburden pressure causes the underlying ice crystals to pack closer together. The firn matrix densifies through this packing and through metamorphism of the crystal fabric. The rate of densification is determined primarily by temperature and accumulation rate. The Herron and Langway (1980) (HL) firn-densification model is a benchmark empirical model, based on depth-density data from Greenland and Antarctic ice cores (Lundin et al., 2017). We model the depth-density profile of the firn using the HL framework due to its simplicity and its good match with measurements of the modern South Pole firn density. We also evaluate the impact that using different firn models would have on our results (Section 5.1).

We use a surface density $\rho_0 = 350$ kg m$^{-3}$, consistent with measured values at the SPC14 site, and assume it remains constant through time (Fausto et al., 2018). We assess the sensitivity of our results to this assumption in Section 5.1. The bottom of the firn is constrained by a close-off density $\rho_{co}$, which we define as a function of temperature (Martinerie et al., 1994). As temperature varies between -50 and -60°C, close-off density varies in a small range between 831.5 and 836.4 kg m$^{-3}$.

We use the analytical formulation of the HL model, which assumes an isothermal firn. If either temperature or accumulation rate changes on short timescales, a transient formulation of the model would be required to reflect propagation through the firn column. Although our temperature and accumulation-rate inputs vary through time, the timescale of those variations (*i.e.,* 10 ka for ∼6°C change in temperature) is large enough that the steady-state approximation is acceptable. To test this assumption, we ran our forward model with a transient formulation of the HL model (Stevens et al., 2020) and found no difference in the results when we account for the advection time through the firn, as we do in our inverse approach. Since the transient model is more computationally expensive, we use the analytical formulation.

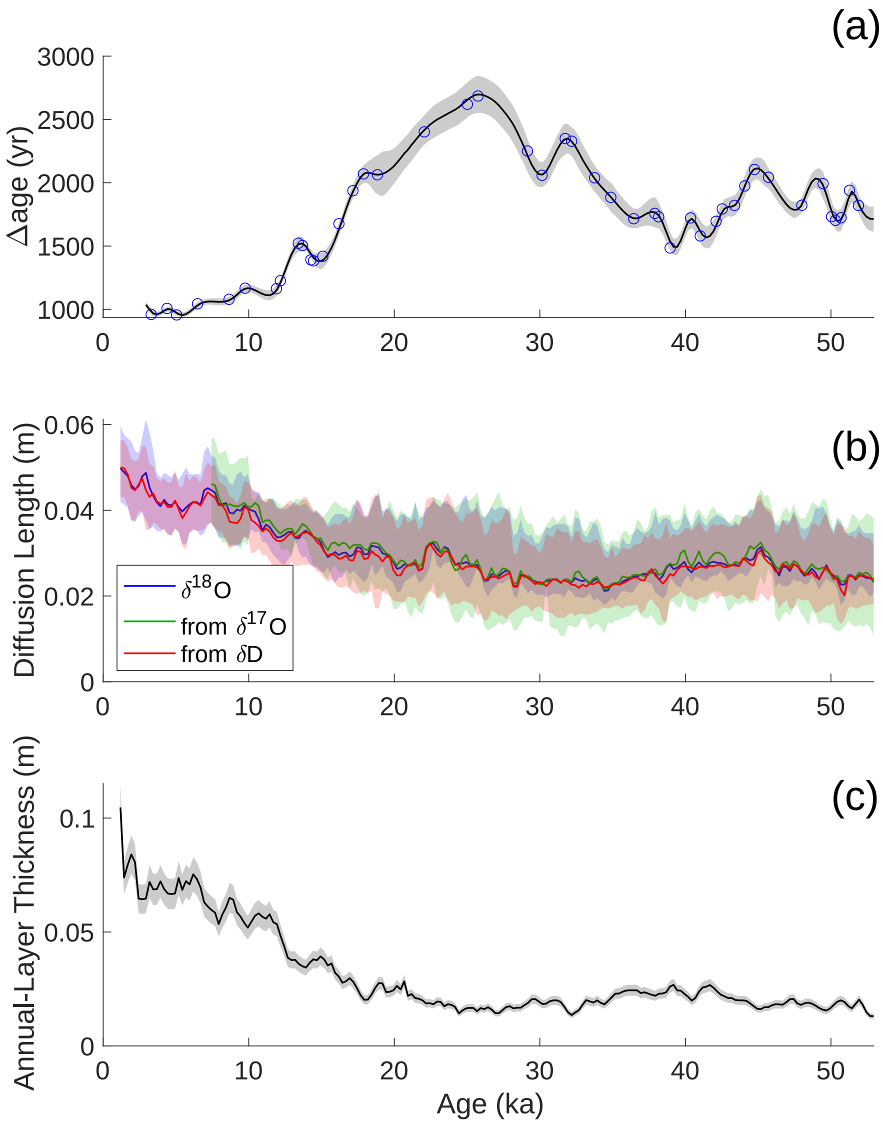


Figure 2: Data sets from SPC14 used to optimize the inverse problem, each averaged over bins of 250 years and plotted with uncertainty representing two s.d. Panel (a) shows Δage with tie points marked in blue circles, panel (b) shows water-isotope diffusion lengths, and panel (c) shows annual-layer thickness data. Diffusion lengths from $\delta^{17}O$ (green) and $\delta D$ (red) have been converted to $\delta^{18}O$-equivalent values.

### 3.2 Modeling Δage

Modeled Δage is given by the difference in the modeled age of the ice and the gas at the lock-in depth. We define the lock-in depth at a density of 10 kg m$^{-3}$ less than the close-

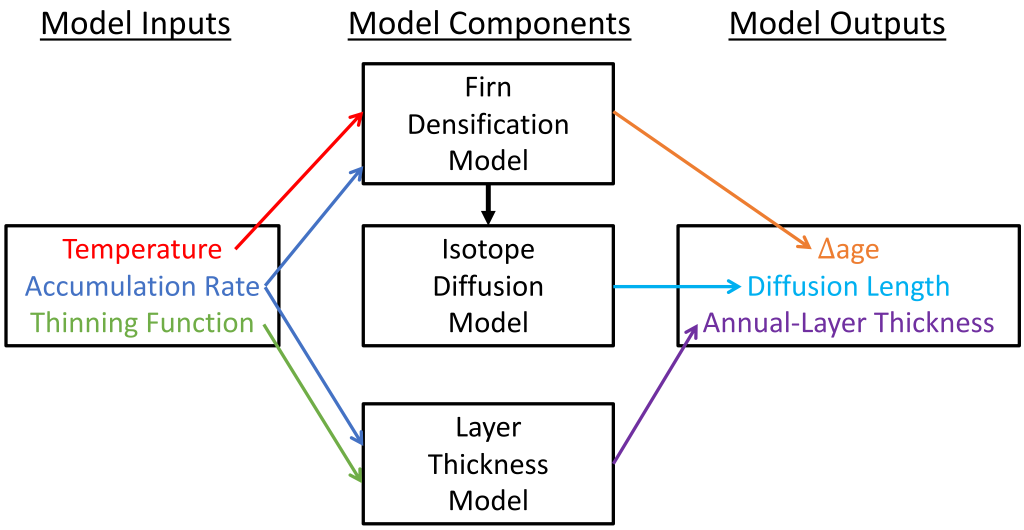


Figure 3: Illustration of the forward model components, which include firn densification (Section 3.1/3.2), water-isotope diffusion (Section 3.3), and a model of layer thickness (Section 3.4). Together, these components relate the variables of interest (temperature, accumulation rate, and thinning function) to the observational data sets (Δage, layer thickness, and diffusion length) shown in Figure 2.

off density (Blunier and Schwander, 2000). The age of the ice at this depth is estimated directly from the age-density profile from the firn-densification model. We estimate the age of the gas at the lock-in depth (LID) using the parameterization in Buizert et al. (2013):

$$\text{gas age}(\rho_{\text{LID}}) = \frac{1}{1.367}\left(0.934 \times \frac{(\text{DCH})^2}{D^0_{CO_2}} + 4.05\right), \tag{3}$$

where DCH is the diffusive column height given in units of m, defined as the lock-in depth minus a 3 m convective zone at the surface where firn air is well-mixed with the atmosphere. $D^0_{CO_2}$ is the free air diffusivity of $CO_2$ defined in Schwander et al. (1988) and Buizert et al. (2012) and given in units of $m^2$ $a^{-1}$. The lock-in depth is defined as the depth at which the effective molecular diffusivity of the gas is reduced to one thousandth of the free air diffusivity (Buizert et al., 2013).

### 3.3 Modeling Diffusion Length

The combined effects on the initial isotope profile ($\delta = \delta(z, 0)$) due to diffusion and firn densification are given by:

$$\frac{\partial \delta}{\partial t} = D\frac{\partial^2 \delta}{\partial z^2} - \dot{\epsilon} z \frac{\partial \delta}{\partial z}, \tag{4}$$

where $\delta(z', t)$ is the resulting smoothed and compressed isotope profile after time $t$ since deposition, $D$ is the diffusivity coefficient, $\dot{\epsilon}$ is the vertical strain rate, and $z$ is the vertical coordinate assuming an origin fixed on an arbitrary sinking layer of firn (Johnsen, 1977; Johnsen et al., 2000; Whillans and Grootes, 1985). Note that $z'$ accounts for the vertical compression of the original profile (Johnsen et al., 2000). Equation 4 is valid where the isotopic exchange between firn grains and the surrounding vapor is rapid, where the firn grains are well mixed and in isotopic equilibrium with the vapor, and where $\delta \ll 1000‰$.

The diffusivity coefficient $D_x$ of each isotope $x$ depends on the temperature and density profile of the firn column Whillans and Grootes (1985); Johnsen et al. (2000):

$$D_x = \frac{m\,p\,D_x^{air}}{RT\,\alpha_x\,\tau}\left(\frac{1}{\rho} - \frac{1}{\rho_{ice}}\right), \tag{5}$$

where $m$ is the molar weight of water, $p$ is the saturation pressure of water vapor over ice at temperature $T$ and with gas constant $R$, $D_x^{air}$ is the diffusivity of each isotopologue through air, $\alpha_x$ is the fractionation factor for each isotopic ratio in water vapor over ice, $\tau$ is the tortuosity of the firn, $\rho$ is the firn density, and $\rho_{ice}$ is the density of ice. Values for these parameters are given in the Supporting Information, Section S1.2.

Using the output from the firn-densification model, we calculate water-isotope diffusion through the depth-density profile. First, the density profile is used to calculate the diffusivity of each isotope based on Equation 5. We then solve for the diffusion length $\sigma_{firn}$ of a particular isotope ratio in terms of its effective diffusivity coefficient $D$ and the firn density $\rho$ (Gkinis et al., 2014):

$$\sigma_{firn}^2(\rho) = \frac{1}{\rho^2}\int_{\rho_0}^{\rho} 2\rho^2 \left(\frac{d\rho}{dt}\right)^{-1} D(\rho)d\rho, \tag{6}$$

where $\rho_0$ is the surface density and $\frac{d\rho}{dt}$ is the material derivative of the density. To calculate the diffusivity $D$, we use an atmospheric pressure of 0.7 atm, the ambient pressure at the SPC14 site (Severinghaus et al., 2001), which we assume to be constant through time.

Cumulative vertical strain significantly thins layers in the ice. The thinning function is defined as the fractional amount of thinning that has occurred at a given depth in the ice sheet. We account for the effects of vertical strain on our modeled firn diffusion length, $\sigma_{firn}$, using a thinning function $\Gamma$. We model the diffusion length measured in the ice core as $\sigma_{icecore}$:

$$\sigma_{icecore} = \sigma_{firn} \times \Gamma. \tag{7}$$

Recall that when we compare the modeled diffusion length with the observations, the observations have been corrected for diffusion in solid ice.

### 3.4 Modeling Annual-Layer Thickness

Annual-layer thickness $\lambda$ is given by the accumulation rate $\dot{b}$, in ice-equivalent m a$^{-1}$, multiplied by the thinning function $\Gamma$:

$$\lambda = \dot{b} \times \Gamma. \tag{8}$$

## 4 Inverse Framework and Results

### 4.1 Initialization

We use a Bayesian statistical approach to produce an ensemble of possible solutions to our inverse problem. Through many iterations, we use the forward model described above to solve our forward problem and determine the range of possible model inputs. This forward problem is described by the following equation, where the forward model, $G$, calculates the modeled observables, or data parameters, $d$ as a function of unknown input variables, or model parameters, $m$:

$$G(m) = d. \tag{9}$$

Our forward model $G$ is nonlinear and cannot be solved analytically. Instead, we use a Monte Carlo approach to solve the inverse problem by testing many instances of $m$ through the forward model $G$ to find the output $d$ that best matches the observations $d_{obs}$. The theory and practical implementation of this approach are detailed in the Supporting Information, Section S2 (Tarantola, 1987; Mosegaard and Tarantola, 1995; Gelman et al., 1996; Mosegaard, 1998; Khan et al., 2000; Mosegaard and Sambridge, 2002; Mosegaard and Tarantola, 2002; Steen-Larsen et al., 2010).

We incorporate *a priori* information about model parameters based on their modern values and our best estimate of how they have varied through time. We include this *a priori* information by creating bounds on the allowable model space to explore and use the Metropolis algorithm to randomly create perturbations that sample within the bounded model space (Metropolis et al., 1953). If the algorithm proposes a solution $m_x$ that falls outside of our bounded model space, $m_x$ is disregarded and another solution is evaluated. Because we expect the parameters to vary smoothly through time, proposed perturbations are smoothed with a lowpass filter to prevent spurious high-frequency noise from being introduced. Temperature and accumulation-rate perturbations are smoothed with a lowpass filter with a cutoff period of 3000 years, which corresponds to the maximum value of $\Delta$age and thus the limit of natural smoothing we expect from the ice-core data. We expect the thinning function to be even smoother and apply a lowpass filter with a cutoff period of 10,000 years to those perturbations.

We also determine initial guesses $m_1$ for each parameter. Initializing the problem at what is judged to be a reasonable solution $m_1$ helps to avoid non-physical solutions (MacAyeal, 1993; Gudmundsson and Raymond, 2008). We design initial guesses for each parameter that are simplified versions of our best initial guess, allowing higher-frequency information to be inferred from the optimization. The initial guess of temperature is a step-function version of the water-isotope record. The initial guess for the thinning function is the output of a Dansgaard and Johnsen (1969) (DJ) ice-flow model. This simple model produces an approximation of the dynamics acceptable at many ice-core sites (Hammer et al., 1978). We use a kink height of $h_0 = 0.2$ to simulate the flank flow at the SPC14 site. To produce an initial guess for accumulation rate, we divide the layer-thickness data by this thinning function and approximate the result with a simplified step function.

Each parameter is bounded based on naïve expectations for its variability. For temperature, we bound the model space with an upper and lower scaling of the step-function initial guess version of the water-isotope record. We create an envelope based on previous estimates of glacial-interglacial temperature change in Antarctica, which allows for solutions with glacial-interglacial changes as small as 0.5°C and as large as 15°C. For accumulation rate, the bounded model-parameter range is an envelope about our initial guess defined as $\pm 0.02$ m a$^{-1}$. Given the surface and Holocene accumulation-rate fluctuations at South Pole described in Lilien et al. (2018), this range is a reasonable limit on accumulation rate, while still allowing variation in the values tested in each $m$. For the ice-equivalent thinning function, we enforce a value of one at the surface but do not provide further constraints on the model space because it is effectively constrained by the bounds on accumulation rate and layer thickness.

### 4.2 *A posteriori* Distributions

The resulting solutions $m$ from our inverse approach are described by the *a posteriori* distribution. To visualize the high-dimensional *a posteriori* distribution, we plot probability distributions for each parameter. Rather than create separate probability distributions for each of the many parameters in our model space, we plot each probability distribution successively in a single figure to visualize the entire model space at once. Figure 4 shows our results, with the model inputs on the left and outputs on the right. The grey shading shows successive probability distributions. A vertical slice through the shading in each plot represents the probability distribution for a particular parameter (recall that a parameter represents the value of a variable at a specified model timestep, *e.g.,* the value of temperature at the 4th timestep). How often a particular value is accepted for each parameter is represented by the shading, where darker shading denotes values that were accepted more often. The solid magenta curves describe the initial guess for each parameter, and the dashed magenta curves describe the bounded model space (for temperature and accumulation rate). The right three panels of Figure 4 illustrate how well the modeled observables $d(m)$ match with the observations $d_{obs}$ throughout the collection of solutions.

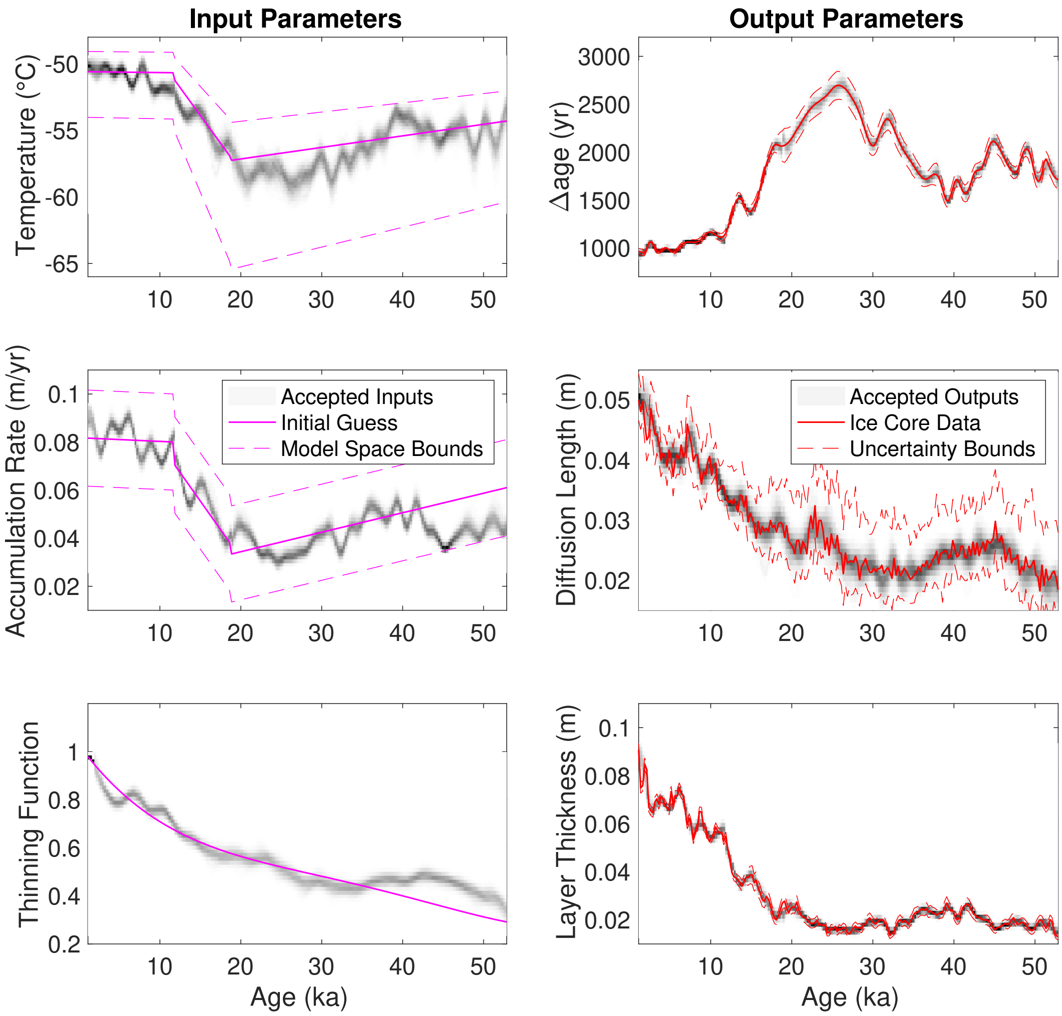


Figure 4: Results of the Monte Carlo inverse calculations, showing the *a posteriori* distribution result compared with *a priori* information. The grey shading in each panel represents probability distributions for each parameter from the *a posteriori* distribution, where darker shading signifies greater likelihood. Left panels show the initial guesses (solid magenta) and model bounds (dashed) for the input parameters: temperature, accumulation rate, and thinning. Right panels show the observational data (solid red) and prescribed uncertainties (dashed) for the output parameters: Δage, diffusion length, and layer thickness.

## 5 Sensitivity of Results

We evaluate the sensitivity of our results to choices within the forward model and inverse algorithm, as well as to constraints from the data sets included in the inverse problem and from independent data.

### 5.1 Sensitivity to Forward Model

Within the forward model, we hold the surface density $\rho_0$ in the firn-densification model constant through time. We tested two alternate values of surface density $\rho_0$ (450 kg m$^{-3}$ and 550 kg m$^{-3}$); we find no significant change in the results. We also did two experiments to assess the impact of the choice of firn-densification model. First, we evaluated the depth-density and age-density profiles using a large collection of models (Herron and Langway, 1980; Goujon et al., 2003; Ligtenberg et al., 2011; Simonsen et al., 2013; Li and Zwally, 2015) within the Community Firn Model framework (Stevens et al., 2020). Second, we implemented two of those models, those of Goujon et al. (2003) (GOU) and Ligtenberg et al. (2011) (LIG), within our inverse framework. The results are similar regardless of which firn model is used, but the GOU and LIG models produce consistently lower temperatures than the HL model. Because this difference is systematic throughout the depth of the core, the magnitude of reconstructed temperature variability, including the glacial-interglacial temperature change, is not significantly affected (Figures S3 and S4). Our choice of the HL model within our forward model is justified by the good agreement with modern temperature compared with these other models and the consistency within the interpretation of the temperature result across all models. Details from these sensitivity tests are given in the Supporting Information, Section S3.1. It has been suggested that most firn models (including the HL model) are biased to produce firn columns that are too thick at very cold temperatures (Landais et al., 2006; Dreyfus et al., 2010; Freitag et al., 2013; Bréant et al., 2017), though the magnitude of this bias is disputed. An implicit assumption in our method is that the HL model is unbiased. We discuss the implications of this assumption in Section 6.

### 5.2 Sensitivity to Inverse Algorithm

Within the formulation of the inverse algorithm, we evaluated the sensitivity to different initial guesses for each parameter. Altering the initial guesses within the model space bounds do not affect the final results. Additionally, including higher-frequency *a priori* information in our initial guesses does not change the results. For example, we evaluated initial guesses of constant values for each of temperature, accumulation rate, and thinning function. These extremely simplified initial guesses produce results indistinguishable from those that include the high-frequency variability of each comparison data set, but require many more iterations to reach an equilibrium solution. As recommended in Gudmundsson and Raymond (2008), we opted for a middle-ground approach that saves time by setting the initial guess close to the expected answer but relies on the optimization to obtain high-frequency information.

### 5.3 Sensitivity to Included Data Constraints

We also examined the sensitivity of the results to each data set individually, as detailed in the Supporting Information, Section S3.2. One key conclusion from these tests is that all three data sets ($\Delta$age, layer thickness, and diffusion length) provide important information for producing a well-constrained result (Figures S6 and S7), although the relative importance of each parameter varies with age in the record. In general, we find that the diffusion length and layer thickness are sufficient to constrain accumulation rate, and the $\Delta$age strongly impacts the temperature. However, while it is evident that $\Delta$age is the most important constraint on temperature for ages less than $\sim$35 ka, at greater ages, constraints provided by the combination of diffusion length and layer thickness become increasingly critical.

We also considered the influence of the temperature-dependence of water-isotope diffusivity. We evaluated the effect of removing the temperature-dependence (Equation 5), so that diffusion-length data affects only the thinning function (Equation 7), and temperature is primarily driven by the $\Delta$age data. The results show a significant difference from the main result, demonstrating that the diffusion-length data provide an important constraint on temperature, which has subsequent impact on other parameters. Further details are provided in the Supporting Information, Section S3.2.

### 5.4 Comparison with $\delta^{15}$N data

Finally, we consider the impact on our results of the inclusion of information from measurements of $\delta^{15}$N in $N_2$ of air bubbles in SPC14 (Winski et al., 2019; Severinghaus et al., 2019). The enrichment of $\delta^{15}$N in an ice core is a linear function of the original diffusive column height (DCH) of the firn, resulting from gravitational fractionation (Sowers et al., 1992; Buizert et al., 2013). We calculate DCH from $\delta^{15}$N as described in the Supporting Information (Equation S19). As shown in Figure S9, there are significant differences between the DCH calculated from the main reconstruction and that calculated from $\delta^{15}$N. We do not incorporate $\delta^{15}$N data in our full Monte-Carlo inverse procedure because this added constraint over-determines the solution; as we show in the following sensitivity test, no combinations of temperature and accumulation rate can simultaneously satisfy $\delta^{15}$N and the other data constraints at all depths in the core. Instead, we evaluate the impact of the additional constraint of $\delta^{15}$N data as follows.

We use the $\delta^{15}$N data to determine temperature and accumulation-rate pairs that produce a DCH in agreement with the $\delta^{15}$N-based DCH. To determine these pairs, we run a global search algorithm over a set of temperature and accumulation-rate values defined by a small range centered on the mean values from the main reconstruction (Figure 4). For each depth in the core, we use the HL firn model to calculate the DCH for all temperature and accumulation-rate values in the global search, and then select only the temperature and accumulation-rate pairs that produce a DCH within the uncertainty of the DCH calculated from $\delta^{15}$N. The result is shown in light-red shading in Figure 5. Compared with our main reconstruction, the accumulation-rate history remains essentially unchanged, but the mean temperature is greater by 2.8°C on average for the glacial period (*i.e.,* before about 15 ka). To further refine this suite of solutions, we select the subset of accumulation-rate and temperature values that both satisfy the $\delta^{15}$N constraint on DCH and are consistent (through the HL model) with $\Delta$age, within the uncertainty of the empirical $\Delta$age data. The blue shading in Figure 5 shows this combination of both $\delta^{15}$N and $\Delta$age constraints; the result is a decrease in mean values for both accumulation rate and temperature during the glacial period compared to $\delta^{15}$N alone. Areas of overlap (dark purple shading) between our main reconstruction and the combined $\delta^{15}$N and $\Delta$age constraints show where all constraints – diffusion length, layer thickness, $\Delta$age, $\delta^{15}$N – are satisfied. Further details on this sensitivity test are given in the Supporting Information, Section S3.3 and Figure S9.

Three important conclusions can be drawn from these comparisons. First, while our temperature and accumulation-rate reconstructions are entirely consistent with $\delta^{15}$N constraints during the Holocene, a combination of warmer temperatures and lower accumulation rates are required to match the $\delta^{15}$N constraint in the glacial period. Second, there is no consistent solution for which all constraints (layer thickness, diffusion length, $\Delta$age, and $\delta^{15}$N), for all depths in SPC14, are satisfied, implying that further refinements to firn models may be required (Supporting Information, Section S3.3). However, for those depths where all constraints are satisfied, the resulting temperatures are warmer by $<1$°C on average than in our main reconstruction. This means that, third, our results are conservative with respect to the assumption that the HL model produces the correct DCH at very cold temperatures. This also supports the exclusion of $\delta^{15}$N in our main reconstruction, to avoid giving too much weight to the reproduction of the DCH by the HL model. For this reason, we focus on the results from our main reconstruction in the discussion which follows.

## 6 Discussion

We now consider our main reconstructions for accumulation rate, ice thinning, and temperature in comparison with estimates from simpler calculations and independent data. In general, the results are in agreement with naïve expectations, but with some important differences. Because the accumulation-rate and thinning reconstructions are fun-

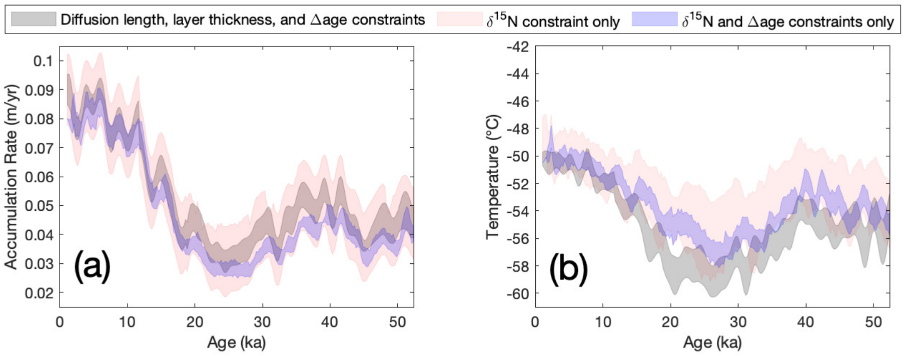


Figure 5: Results from a sensitivity test that includes $\delta^{15}$N as a constraint on diffusive column height (DCH). Panel (a) shows accumulation rate, and panel (b) shows temperature; shading represents 2 s.d. uncertainty for all three reconstructions. The main reconstruction is shown in grey. Results consistent with the $\delta^{15}$N constraints (only) are shown in red. Results consistent with both $\delta^{15}$N and the empirical $\Delta$age data are shown in blue. The overlap of blue and grey shows where all empirical constraints (layer thickness, diffusion length, $\Delta$age, and $\delta^{15}$N) are satisfied within the framework of the firn model. Further details are given in the Supporting Information, Section S3.3 and Figure S9.

damentally linked through Equation 8, we discuss them together. We then compare our reconstruction for temperature with the traditional water-isotope paleothermometer, and discuss the broader implications of our results. The *a posteriori* distribution is near-Gaussian, and in this section we plot its mean and standard deviation rather than the full probability distributions. Recall that the *a posteriori* distribution comprises only accepted solutions, a subset of all iterations.

### 6.1 Accumulation Rate and Thinning Function

Figure 6 shows the results for the thinning function (panel (a)) and accumulation rate (panel (b)). The grey shading denotes a band of two s.d. of the *a posteriori* distribution. In general, thinning functions are expected to be smooth and to decrease monotonically because they integrate the total thinning experienced at a given depth, as illustrated by the results of a 1-D Dansgaard-Johnsen (DJ) model with $h_0 = 0.2$ (red curve, panel (a)). However, the SPC14 site is far from an ice divide such that variations in the bed topography upstream can create more complex thinning histories (e.g., Parrenin et al., 2004). Thus, the thinning function result is similar to the DJ-model output, but contains additional higher-frequency variations. To evaluate the plausibility of these variations in the primary reconstruction, we compare with two other independent estimates of the thinning function, an ice-flow-model thinning function and a $\delta^{15}$N-based thinning function.

First, we compare the primary thinning function with one calculated from an ice-flow model. We use a 2.5-D flowband model (Koutnik et al., 2016) forced with observations of the bedrock topography and the accumulation-rate pattern. Details of the model setup are given in the Supporting Information, Section S4 (Nye, 1963; Looyenga, 1965; Gades et al., 2000; Neumann et al., 2008; Catania et al., 2010; Jordan et al., 2018). The resulting thinning function is best considered in two segments. The thinning function for the past 10 ka (solid black line in Figure 6) is well constrained because the flowline is known (Lilien et al., 2018) and the bed topography has been measured along the flowline (Figure S11). The key result is that the bed undulations along the flowline cause the same structure as is inferred in the primary thinning function. The "reversal" in the thinning function at 7 ka, where deeper layers have thinned less than shallower layers, matches

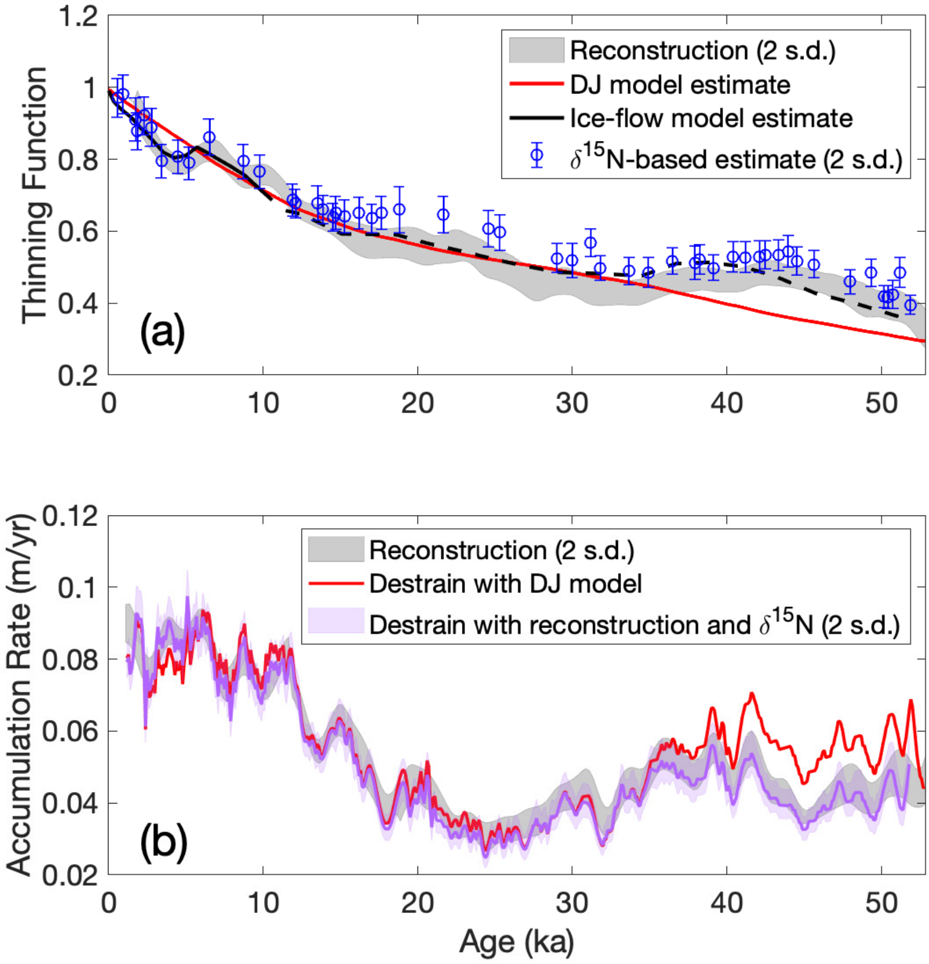


Figure 6: Reconstructions of accumulation rate and thinning function for SPC14. Two s.d. (grey shading) of the *a posteriori* distribution is plotted for each reconstruction alongside comparison estimates. Panel (a) shows the primary thinning function reconstruction (grey) compared to a DJ-model output with $h_0 = 0.2$ (red), an ice-flow-model thinning function from a 2.5-D flowband model (solid and dashed black), and a $\delta^{15}$N-based thinning function with error bars showing two s.d. uncertainty (blue). The solid black curve shows where the ice-flow-model thinning function is well constrained by data, and the dashed black curve shows where the bed topography is simulated. The thinning function is shown vs. depth in the Supporting Information (Figure S10). Panel (b) shows the accumulation-rate reconstruction compared to two versions of the destrained layer-thickness data. The thinning functions used for destraining are the DJ-model output (red) and the mean of the reconstruction and the $\delta^{15}$N-based estimate (purple).

well in both the primary and ice-flow-model thinning functions. This feature is caused by an overdeepening in the bed topography (Figure S18).

For ages older than 10 ka, we do not know where the ice originated and thus cannot use the ice-flow model to determine the thinning function with confidence. Instead, we aim to evaluate whether the primary thinning function is physically plausible, given what we know about the bed topography in the region. Using airborne radar measurements (Forsberg et al., 2017) to create a plausible bed beyond 100 km upstream, we show that the ice-flow model (black dashed line) can approximately match the magnitude and structure of the primary thinning function. Therefore, the primary thinning function is consistent with expectations, given plausible variations in bedrock topography.

Second, we compare the primary thinning function with a $\delta^{15}$N-based thinning function (blue circles; error bars show two s.d. uncertainty). We obtain this estimate following the methods described in Parrenin et al. (2012), who showed that the thinning function scales with the ratio of "$\Delta$depth" to the DCH, where $\Delta$depth is given by $\Delta$age multiplied by the depth/age slope from the ice-core timescale. The thinning function $\Gamma$ is then given by (Parrenin et al., 2012):

$$\Gamma = \frac{\Delta\text{depth}}{A \times \text{LID}}, \tag{10}$$

where $A$ is a scaling factor that accounts for the ice-equivalent thickness of the original firn column (Winski et al., 2019), and the lock-in depth, LID = DCH + 3, accounting for a 3-m convective zone. We use our temperature reconstruction to incorporate the impact of thermal fractionation in our calculation of the LID (Grachev and Severinghaus, 2003; Cuffey and Paterson, 2010; Fudge et al., 2019). Full details on this approach and its uncertainties are given in the Supporting Information, Section S5.

Figure 6a shows that the structure of the $\delta^{15}$N-based thinning function generally agrees with the primary reconstruction, showing the same high-frequency variations and mean estimates whose error bars in general overlap with the uncertainty of the primary reconstruction. There is the least agreement between ages of about 15 and 30 ka, where the $\delta^{15}$N-based thinning function is shifted appreciably towards higher values (less thinning). This is consistent with the observation that the modeled DCH from our main reconstruction tends to be higher than that calculated from $\delta^{15}$N. We note that the uncertainties for the $\Delta$depth calculation are not depth-independent; many known sources of error are expected to be systematic. For example, if the WAIS Divide $\Delta$age data set were systematically too large during the glacial period, correcting for this would result in smaller estimates for the SPC14 $\Delta$depth, and therefore smaller values (more thinning) in the $\delta^{15}$N-based thinning function. The same adjustment to $\Delta$age results in no significant change in the primary thinning function, thus improving the agreement between the means of the two independent estimates. We discuss further quantification of uncertainties in these calculations in Section 5.4 and Section S5.1 in the Supporting Information.

For comparison with the accumulation-rate reconstruction, Figure 6b shows two versions of high-frequency estimates produced by destraining the layer-thickness data with estimates of the thinning function. The red curve uses the 1-D Dansgaard-Johnsen thinning function; the resulting accumulation-rate estimate deviates from the reconstruction at the oldest ages. Thus, the reconstruction reflects a significantly smaller accumulation rate before 40 ka than would be inferred using a DJ model. The purple curve shows our best estimate for high-frequency accumulation rate by combining the information from both the primary thinning function and the $\delta^{15}$N-based thinning function; we use the mean of these two thinning functions to destrain the layer-thickness data. We incorporate information from both thinning functions in order to include all available information in our best estimate. The uncertainty is estimated by combining the uncertainties of both thinning functions.

### 6.2 Temperature Reconstruction

The temperature reconstruction is shown in Figure 7. For comparison, we show two scaled versions of the measured $\delta^{18}$O, corrected for secular variations in the $\delta^{18}$O of sea-water, following Bintanja and van de Wal (2008). Recall that while we used diffusion length determined from the $\delta^{18}$O power spectrum in our reconstruction, we do not use the abso-

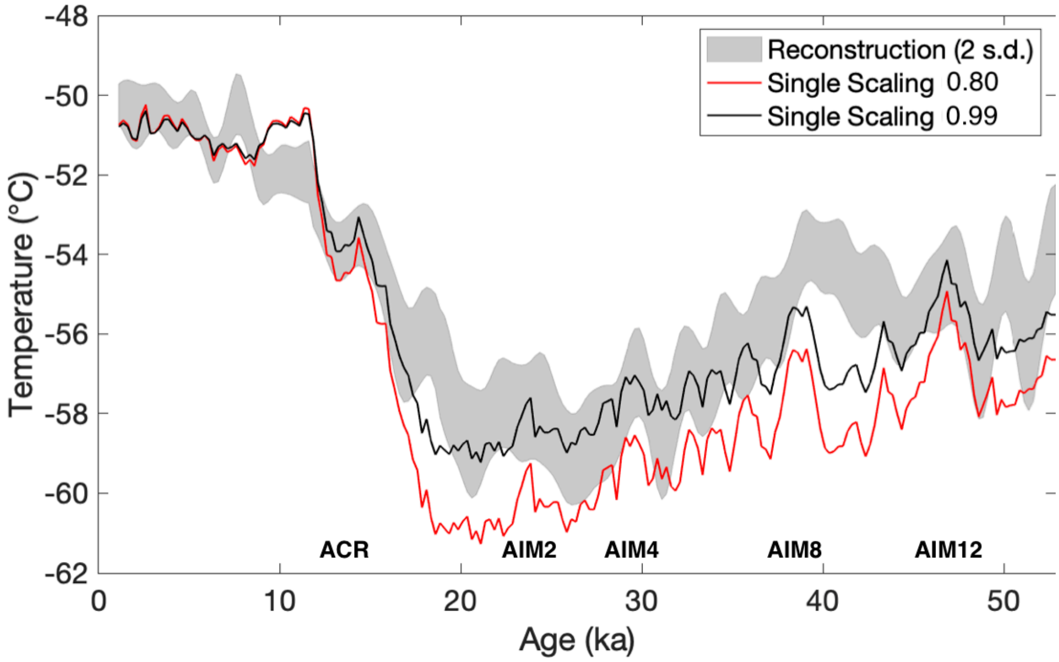


Figure 7: Reconstruction of temperature and relationship with $\delta^{18}$O. Grey shading shows two s.d. of the *a posteriori* distribution. Solid lines show scaled versions of $\delta^{18}$O, discretely averaged to 250-year resolution. The $\delta^{18}$O is scaled by 0.8‰°C$^{-1}$ (red), the modern surface relationship, and by 0.99‰°C$^{-1}$ (black), the calibrated linear relationship with the mean of the temperature reconstruction.

lute $\delta^{18}$O values; hence, these comparisons serve as an independent calibration of the traditional water-isotope thermometer, similar to what has been done previously with borehole thermometry (Cuffey et al., 1995, 2016) but maintaining higher-frequency information. The red curve in Figure 7 uses a scaling of $\partial(\delta^{18}\mathrm{O})/\partial T = 0.8‰°\mathrm{C}^{-1}$, which is both the observed modern surface isotope-temperature relationship at the site (Fudge et al., 2020) and the value commonly used in the literature for Antarctica (e.g., Jouzel et al., 2003), for which Masson-Delmotte et al. (2008) report a 1 s.d. error of 0.01‰°C$^{-1}$. The black curve shows the best-fit linear calibration between $\delta^{18}$O and the mean of our reconstruction; this has a significantly greater slope of 0.99±0.03‰°C$^{-1}$ (2 s.d.). Our estimate of uncertainty on the slope accounts for errors in both variables, following the method of York et al. (2004), with errors on temperature given by the *a posteriori* distribution (Figure 7) and errors on $\delta^{18}$O (0.1‰, 1 s.d.) obtained from replicate continuous-flow measurements made on the South Pole ice core as reported in Steig et al. (2021). Results from the sensitivity tests (Section 5) using other firn models, and using independent $\delta^{15}$N constraints, yield the same result: slopes vary from 0.97 to greater than 1.2‰°C$^{-1}$. Correlation with the $\delta^{18}$O is greatest ($r$=0.94) with our main reconstruction (see Supporting Information, Section S3.4).

There are interesting similarities and differences between the calibrated $\delta^{18}$O and our independent temperature reconstruction. For example, the prominent Antarctic Isotope

Maximum 12 (AIM12) event, at about 47 ka, is similar in both our reconstruction and the scaled $\delta^{18}$O data, and suggests a temperature change of about 2°C. On the other hand, our temperature reconstruction for AIM8, at about 38 ka, is part of a low-frequency variation longer than that indicated by the $\delta^{18}$O data, and the mean reconstruction suggests that AIM8 was warmer than AIM12, while a simple linear scaling of the $\delta^{18}$O implies the opposite. Another interesting feature is AIM2 ($\sim$24 ka), which is muted in most East Antarctic records, but is prominent in the WAIS Divide ice core (WAIS Divide Project Members, 2013). AIM2 is clearly evident in both our reconstruction and in the scaled $\delta^{18}$O data, as is AIM4 ($\sim$30 ka) and the Antarctic Cold Reversal (ACR) ($\sim$13 ka).

In contrast, the early-Holocene isotope maximum (centered at about 10 ka) is muted in our temperature reconstruction. This is perhaps surprising, given the prevalence of this feature in the $\delta^{18}$O records, both at South Pole and elsewhere in East Antarctica. On the other hand, there is no early-Holocene peak in the WAIS Divide record, in either the $\delta^{18}$O or the borehole-calibrated temperature reconstruction (WAIS Divide Project Members, 2013; Cuffey et al., 2016). Furthermore, the temperature reconstruction suggests an earlier onset of deglacial warming (at about 22 ka) than the isotope data suggest, but similar to both the isotope data and the temperature reconstruction at WAIS Divide (WAIS Divide Project Members, 2013; Cuffey et al., 2016). Because large changes in the $\delta^{18}$O-temperature relationship can occur, for example, from changes in seasonality (Steig et al., 1994; Werner et al., 2000), we cannot assume that either result (*i.e.,*, our main reconstruction or the scaled $\delta^{18}$O) is the more faithful representation of temperature. Reconciling the differences would benefit from transient simulations, including water isotopes, of the AIM events and the early-Holocene maximum, as recently achieved for Dansgaard-Oeschger events in Greenland (Sime et al., 2019), and of the deglaciation.

Clearly, a single $\partial(\delta^{18}\mathrm{O})/\partial T$ scaling does not capture all of the variability in our temperature reconstruction. We explored calibrations separated by frequency and time period (*i.e.,* millennial versus glacial-interglacial frequencies and Holocene versus glacial time periods), but find the resulting fits were not statistically distinguishable from that of the single scaling. Thus, there is no evidence of the large change in scaling that has been observed in Greenland ice cores (Cuffey et al., 1995), attributable primarily to changes in the seasonality of precipitation (Steig et al., 1994; Werner et al., 2000). Our results agree well with the assumption generally made in East Antarctica that the slope remains constant through time (*e.g.,* Jouzel et al. (2003)), but show that this slope cannot be assumed to be the same as the modern spatial relationship.

While our calibration yields a significantly greater slope than has been generally used in previous work, this slope is consistent with isotope-modeling results. Modeling work has shown that the sensitivity of $\delta^{18}$O to temperature should increase at sites with colder mean-annual temperatures and higher elevations in Antarctica. For example, Markle (2017) obtains $\partial(\delta^{18}\mathrm{O})/\partial\ \mathrm{T} \sim 0.8‰°\mathrm{C}^{-1}$ for a location like WAIS Divide, in agreement with the borehole temperature calibration, and $\partial(\delta^{18}\mathrm{O})/\partial\ \mathrm{T} \sim 1‰°\mathrm{C}^{-1}$ for South Pole. This difference in sensitivity occurs because air masses traveling to higher elevations are on different moist isentropic surfaces and experience greater rainout for a given change in temperature (Bailey et al., 2019).

### 6.3 Upstream Corrections and Site Reconstructions

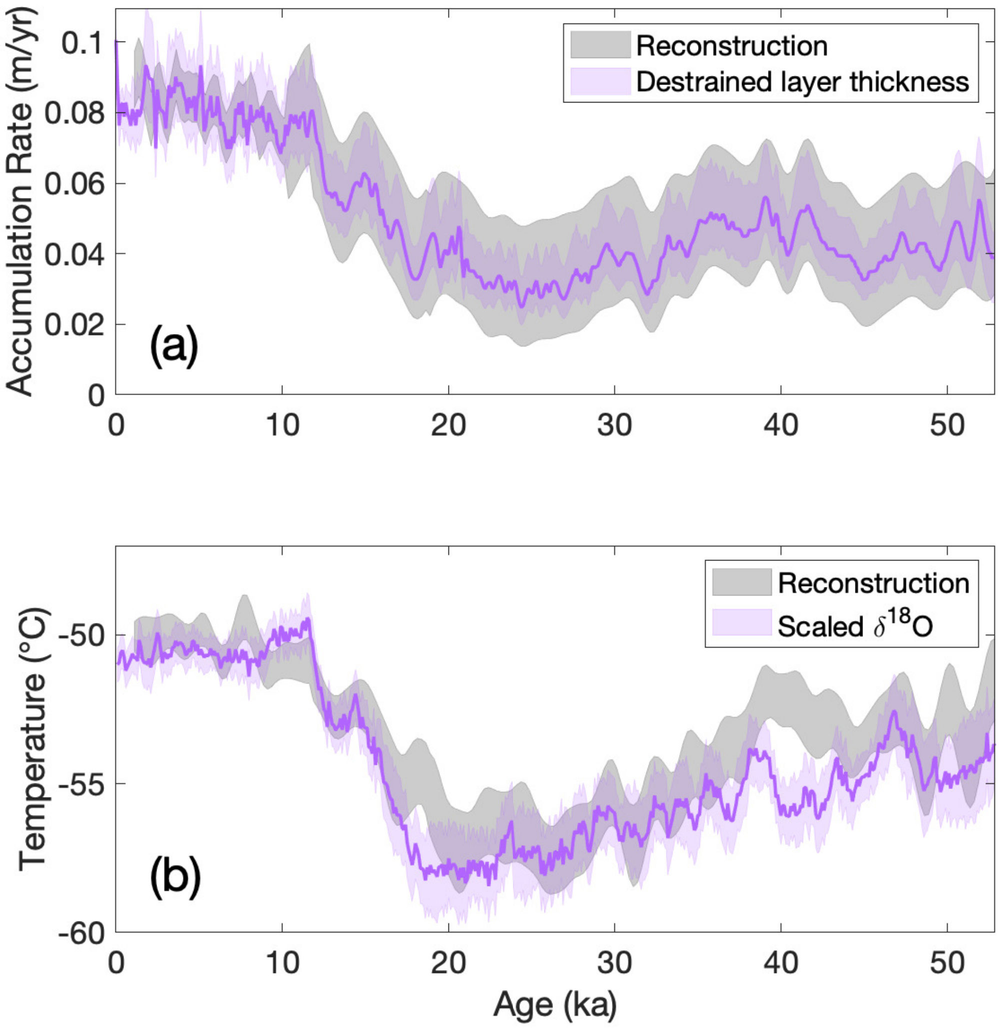


Figure 8: Advection-corrected reconstructions of accumulation rate and temperature at the South Pole site. Advection corrections are based on Lilien et al. (2018) and Fudge et al. (2020), as described in the text. All shading indicates two s.d. uncertainty. Panel (a) shows two advection-corrected accumulation-rate histories: the main reconstruction (grey) and the high-frequency accumulation-rate history from destraining 100-year average layer thicknesses (purple), corresponding to the ice-core histories shown in Figure 6b. Panel (b) compares the advection-corrected temperature estimates from our reconstruction and from the scaled $\delta^{18}$O, averaged to 100-year resolution. Uncertainty takes into account the correlation coefficient between the temperature reconstruction and the scaled isotope estimate.

Because SPC14 was drilled far from the divide, deeper ice in the core originated increasingly farther upstream. To obtain accurate climate histories, it is necessary to remove the influence of flow from upstream where the climate conditions are different. We correct for advection of ice based on Lilien et al. (2018) and Fudge et al. (2020). Using measurements of surface velocities and the pattern of modern accumulation rate upstream along the flowline, Lilien et al. (2018) correlated the measured ice-core layer thicknesses with the expected layer thickness due to advection through the upstream accumulation-rate pattern. This provides a unique constraint on the origin of ice for the past 10 ka and indicates an increase in surface flow speed of about 15% through that time period. We rely on this novel constraint for our advection correction rather than the advection predicted with the steady-state flowband model, and we note that the two approaches give similar trajectories for the reversal in the thinning function at 7 ka (Figure S13). Fudge et al. (2020) measured $\delta^{18}$O values using 10-m firn cores at 12.5 km intervals along the flowline to determine an appropriate correction for $\delta^{18}$O. Fudge et al. (2020) also measured 10-m firn temperatures, and while the results were inconclusive, they were consistent with a typical 10°C km$^{-1}$ lapse rate (dry adiabatic). Using this information, we apply corrections to the "ice core" reconstructions described above to produce "site" reconstructions of accumulation rate and temperature.

The upstream correction to accumulation rate is separated into two time intervals. For ages younger than 10.2 ka, the surface accumulation-rate pattern upstream of the core is known (Lilien et al., 2018). We apply these modern surface variations as a correction by adding the deviation from the mean value to the accumulation-rate ice-core reconstruction. This correction damps the variability of Holocene accumulation rate in the site reconstruction compared with the ice-core reconstruction, but it does not affect the trend of the mean. For ages older than 10.2 ka, there is an insignificant linear trend in the accumulation rate along the 100 km flowline such that Fudge et al. (2020) suggest no long-term advection correction. Thus we make no correction to the ice-core reconstruction for ages older than 10.2 ka. We do not attempt to correct for the impact of spatial variability on the ice-core reconstruction for these older ages, but note that non-climate variations of roughly 15% are expected to occur on millennial timescales. We estimate the uncertainty in the accumulation-rate upstream correction using the variations in accumulation rate along the flowline. For ages older than 10.2 ka, we assume the $1\sigma$ uncertainty is equal to the standard deviation of the upstream accumulation-rate pattern. For ages younger than 10.2 ka, the uncertainty is lower because we have removed much of the impact of advection; however, the correction is not perfect. Roughly 2/3 of the variance in the measured annual-layer thicknesses is explained by advection (Lilien et al., 2018). We thus conservatively assume a $1\sigma$ uncertainty is equivalent to half the standard deviation. Adding this uncertainty in quadrature to the uncertainty of the ice-core accumulation-rate estimates shown in Figure 6b, we produce the site accumulation-rate histories and their uncertainty bounds shown in Figure 8a. The grey bounds show the advection-corrected accumulation-rate reconstruction from our inverse approach and the purple bounds show the advection-corrected high-frequency accumulation-rate estimate from destraining the layer-thickness data with our thinning function reconstruction.

To correct the ice-core temperature reconstruction, we apply the dry adiabatic lapse rate of 10°C km$^{-1}$ to the elevation correction given by Fudge et al. (2020) to produce the grey shading in Figure 8b. We do not quantify uncertainty associated with this correction. For comparison with the water-isotope record, we correct the $\delta^{18}$O with the water-isotope correction given by Fudge et al. (2020) and scale the record using the best-fit linear calibration with the site reconstruction (also 0.99‰°C$^{-1}$) to produce the purple curve in Figure 8b. The uncertainty in the advection correction takes into account the correlation coefficient between the temperature reconstruction and the scaled isotope estimate.

We use our site temperature reconstruction to determine the magnitude of glacial-interglacial temperature change at South Pole. We define this change as the difference in the mean temperature within the intervals of 0.5 - 2.5 ka and 19.5 - 22.5 ka. Note that our reconstruction ends at 0.5 ka, not the present, because the upper ∼500 years of the record is in the firn; hence, $\Delta$age is undefined and diffusion of water isotopes is still in progress.

The choice of the last glacial maximum (LGM) window avoids the prominent warming of the Antarctic Isotope Maximum (AIM2) event. The site temperature reconstruction gives a glacial-interglacial temperature change at the South Pole site of 6.65±0.96°C (one s.d.). The site scaled $\delta^{18}$O gives a glacial-interglacial temperature change of 7.15±0.68°C (one s.d.).

Our site temperature estimate indicates a 2 to 3.5°C lower glacial-interglacial surface temperature change than that reconstructed from other ice cores in east Antarctica, which is generally taken to be 9°C (Parrenin et al., 2013). Importantly, assessment of uncertainty in our calculations suggests that this key finding is conservative. In particular, there is some indication that firn-densification models may be biased to produce diffusive column heights that are too large at cold temperatures (Landais et al., 2006; Dreyfus et al., 2010; Freitag et al., 2013; Bréant et al., 2017). If the Herron-Langway model were in fact unbiased, then even warmer LGM temperatures would be required.

The difference between our results and the conventional 9°C value cannot be readily attributed to elevation change at South Pole, which is unlikely to have been more than 100 m thinner during the last glacial maximum, thus accounting for at most about 1°C of the difference, assuming a dry adiabatic lapse rate of 10°C km$^{-1}$. (Constraints from ice sheet models and geodetic data (Pollard and DeConto, 2009; Whitehouse et al., 2012; Briggs et al., 2014; Argus et al., 2014; Golledge et al., 2014; Roy and Peltier, 2015) show a near-zero mean elevation change, with a standard deviation of 50 m.)

Our results show that the commonly-used 9°C value for glacial-interglacial change in East Antarctica, which is based on water isotopes unconstrained by the independent estimates we use here, is too large. This finding may resolve an apparent disagreement, first recognized at least three decades ago (Crowley and North, 1991), between ice-core-based temperature estimates and results from general circulation models (GCMs), which produce cold-enough LGM temperatures only if surface elevations significantly higher than present are assumed (e.g., Masson-Delmotte et al., 2006; Lee et al., 2008; Werner et al., 2018), or other boundary conditions, such as extensive sea ice, are imposed (Schoenemann et al., 2014). Such GCM estimates are in better agreement with our results if corrected for the prescribed elevation changes, consistent with the smaller changes in East Antarctic ice elevations during the LGM indicated by more recent results than those suggested by earlier work (e.g., Peltier, 2004).

## 7 Conclusions

The South Pole ice core (SPC14) provides the opportunity to obtain reconstructions of important climate variables using multiple independent constraints. SPC14 has an empirical measure of the gas-age ice-age difference, Δage, obtained independently of firn-densification modeling (Epifanio et al., 2020). We also present a new continuous record of water-isotope diffusion length. Both Δage and diffusion length depend on firn properties, which in turn depend on the snow-accumulation rate and firn temperature. The water-isotope diffusion length provides an important additional constraint on the ice-thinning function, which relates measured layer thickness with the original accumulation rate at the surface. Layer thickness variations in SPC14 are well constrained by the ice timescale for the core, developed by annual-layer counting through the Holocene and by stratigraphic matches with the well-dated West Antarctic Ice Sheet Divide ice core (Winski et al., 2019). We have used a statistical inverse approach to combine information from all these data sets to obtain an ensemble of self-consistent temperature, accumulation-rate, and ice-thinning histories.

Our estimate of the thinning function for SPC14 indicates greater variations in thinning rate, in particular less thinning at depth, than can be captured with a simple one-dimensional ice-flow parameterization such as the commonly-used Dansgaard-Johnsen model. Variations in thinning comparable in timing and magnitude to our results are supported by a 2.5-D flowband model that accounts for variations in bedrock topography upstream of the drill site. The thinning function reconstruction is particularly important because SPC14 was drilled more than 200 km away from the ice divide and the surface velocity is high (10 m $a^{-1}$) (Casey et al., 2014). Our results demonstrate the value of using water-isotope diffusion length, in conjunction with annual-layer thickness, to more precisely constrain the thinning function. This approach, also employed by Gkinis et al. (2014) for a Greenland ice core, is entirely independent of the $\delta^{15}$N method of Parrenin et al. (2012), and provides an important new observational constraint on ice-sheet flow.

Our temperature reconstruction serves two important purposes. First, it provides the first empirical, high-frequency estimate of temperature for an East Antarctic ice-core site that does not depend on the traditional water-isotope paleothermometer. It thus enables an independent calibration of the isotope-temperature sensitivity, $\partial(\delta^{18}\mathrm{O})/\partial T$, similar to what has been done in central Greenland and in West Antarctica using borehole thermometry (Cuffey et al., 1995, 2016). Moreover, our approach preserves additional high-frequency information that is not available from the highly diffused borehole-temperature measurements. We find no evidence of a time- or frequency-dependence to the $\partial(\delta^{18}\mathrm{O})/\partial T$ relationship, in contrast to the case for Greenland. Second, our results indicate a smaller glacial-interglacial temperature change at South Pole than previously estimated elsewhere in East Antarctica. Our results yield a glacial-interglacial change of 6.7±1.0°C (one s.d.). This value is in better agreement with results from climate models, which generally match the much colder LGM temperatures obtained from traditional isotope-temperature scaling only when high ice-sheet elevations are assumed. The difficulty of reconciling temperature estimates from climate models and ice-core data has been noted in the literature for more than three decades (Crowley and North, 1991; Masson-Delmotte et al., 2005; Lee et al., 2008; Schoenemann et al., 2014). Our results thus lend greater confidence to the fidelity of climate-model simulations of last glacial maximum climate.

## 8 Data Availability

The published data set associated with this paper, including water isotope diffusion lengths and all of the reconstructions discussed in this manuscript, can be accessed through the USAP Data Center (DOI: 10.15784/601396). The SPC14 high-resolution water stable isotope record published with this paper can also be accessed through the USAP Data Center (DOI: 10.15784/601239). The radar data used in the ice-flow modeling can be accessed through the USAP Data Center at https://www.usap-dc.org/view/project/p0000200. The code used in this work is publicly available at https://doi.org/10.5281/zenodo.4579416, and the Community Firn Model is available at https://doi.org/10.5281/zenodo.3585885.

## Acknowledgments

This work was funded through grants from the US National Science Foundation (E.J.S. (1143105 and 1141839), C.B. (1643394 and 1443472), M.R.K. and others (1443471)). We thank J.P. Severinghaus for providing $^{15}$N data collected under grant NSF1443710. We thank G.H. Roe, B.R. Markle, and D. Shapero for suggestions on this work, and M. Twickler and J. Souney for their work administering the SPICEcore project. We thank the SPICEcore field team, the 109th New York Air National Guard, and the National Science Foundation Ice Core Facility, for the collection, transport, processing, and storage of the core. Finally, we thank the two reviewers of this manuscript for their very thorough comments and suggestions, which helped considerably in compiling the final publication.

## References

Argus, D. F., Peltier, W. R., Drummond, R. & Moore, A. W. (2014). The Antarctica component of postglacial rebound model ICE-6G C (VM5a) based upon GPS positioning, exposure age dating of ice thicknesses, and relative sea level histories. *Geophys. J. Int., 198*(1), 537–563. https://doi.org/10.1093/gji/ggu140

Bailey, A., Singh, H. K. A., & Nusbaumer, J. (2019). Evaluating a moist isentropic rramework for poleward moisture transport: implications for water isotopes over Antarctica. *Geophysical Research Letters, 46*(13), 7819–7827. https://doi.org/10.1029/2019GL082965

Barkan, E., & Luz, B. (2007). Diffusivity fractionations of $H_2^{16}O/H_2^{17}O$ and $H_2^{16}O/H_2^{18}O$ in air and their implications for isotope hydrology. *Rapid Communications in Mass Spectrometry, 21*(18), 2999–3005. https://doi.org/10.1002/rcm.3180

Bazin, L., Landais, A., Lemieux-Dudon, B., Toyé Mahamadou Kele, H., Veres, D., Parrenin, F., et al. (2013). An optimized multi-proxy, multi-site Antarctic ice and gas orbital chronology (AICC2012): 120–800 ka. *Climate of the Past, 9*, 1715–1731. https://doi.org/10.5194/cp-9-1715-2013

Bintanja, R., & van de Wal, R. S. W. (2008). North American ice-sheet dynamics and the onset of 100,000-year glacial cycles. *Nature, 454*(7206), 869–872. https://doi.org/10.1038/nature07158

Blunier, T., & Schwander, J. (2000). Gas enclosure in ice: age difference and fractionation. *Physics of Ice Core Records* 307–326. Hokkaido University Press.

Bréant, C., Martinerie, P., Orsi, A., Arnaud, L., & Landais, A. (2017). Modelling firn thickness evolution during the last deglaciation: constraints on sensitivity to temperature and impurities. *Climate of the Past, 13*, 833–853. https://doi.org/10.5194/cp-13-833-2017

Briggs, R. D., Pollard, T., & Tarasov, L. (2014). A data-constrained large ensemble analysis of Antarctic evolution since the Eemian. *Quaternary Science Reviews, 103*, 91–115. https://doi.org/10.1016/j.quascirev.2014.09.003

Buizert, C., Martinerie, P., Petrenko, V. V., Severinghaus, J. P., Trudinger, C. M., Witrant, E., Steele, L. P., et al. (2012). Gas transport in firn: multiple-tracer characterisation and model intercomparison for NEEM, Northern Greenland. *Atmospheric Chemistry and Physics, 12*(9), 4259–4277. https://doi.org/10.5194/acp-12-4259-2012

Buizert, C., Sowers, T., & Blunier, T. (2013). Assessment of diffusive isotopic fractionation in polar firn, and application to ice core trace gas records. *Earth and Planetary Science Letters, 361*, 110–119. https://doi.org/10.1016/j.epsl.2012.11.039

Buizert, C., Gkinis, V., Severinghaus, J. P., He, F., Lecavalier, B. S., Kindler, P., Brook, E. J., et al. (2014). Greenland temperature response to climate forcing during the last deglaciation. *Science, 345*(6201), 1177–1180. https://doi.org/10.1126/science.1254961

Buizert, C., Cuffey, K. M., Severinghaus, J. P., Baggenstos, D., Fudge, T. J., Steig, E. J., Sowers, T. A., et al. (2015). The WAIS divide deep ice core WD2014 chronology–Part 1: methane synchronization (68–31 kaBP) and the gas age–ice age difference. *Climate of the Past, 11*, 153–173. https://doi.org/10.5194/cp-11-153-2015

Casey, K. A., Fudge, T. J., Neumann, T. A., Steig, E. J., Cavitte, M. G. P., & Blankenship, D. D. (2014). The 1500 m South Pole ice core: Recovering a 40 ka environmental record. *Annals of Glaciology, 55*(68), 137–146. https://doi.org/10.3189/2014AoG68A016

Catania, G, C. Hulbe, & Conway, H. (2010). Grounding-line basal melt rates determined using radar-derived internal stratigraphy. *Journal of Glaciology, 56*(197), 545–554. https://doi.org/10.3189/002214310792447842

Crowley, T. J., & North, G. R. (1991). *Paleoclimatology.* New York, NY: Oxford University Press.

Cuffey, K. M., & Steig, E. J. (1998). Isotopic diffusion in polar firn: Implications for interpretation of seasonal climate parameters in ice-core records, with emphasis on central Greenland. *Journal of Glaciology, 44*(147), 273–284.

https://doi.org/10.3189/S0022143000002616
Cuffey, K. M., & Paterson, W. S. B. (2010). The physics of glaciers. Academic Press.
Cuffey, K. M., Clow, G. D., Alley, R. B., Stuiver, M., Waddington, E. D., & Saltus, R. W. (1995). Large arctic temperature change at the Wisconsin-Holocene glacial transition. *Science, 270*(5235), 455–458. https://doi.org/10.1126/science.270.5235.455
Cuffey, K. M., Clow, G. D., Steig, E. J., Buizert, C., Fudge, T. J., Koutnik, M., Severinghaus, J. P., et al. (2016). Deglacial temperature history of West Antarctica. *Proceedings of the National Academy of Sciences, 113*(50), 14249–14254. https://doi.org/10.1073/pnas.1609132113
Dahl-Jensen, D., Mosegaard, K., Gundestrup, N., Clow, G. D., Johnsen, S. J., Hansen, A. W., & Balling, N. (1998). Past temperatures directly from the Greenland ice sheet. *Science, 282*(5387), 268–271. https://doi.org/10.1126/science.282.5387.268
Dansgaard, W. (1964). Stable isotopes in precipitation. *Tellus B, 16*(4), 436–468. https://doi.org/10.3402/tellusa.v16i4.8993
Dansgaard, W., & Johnsen, S. J. (1969). A flow model and a time scale for the ice core from Camp Century, Greenland. *Journal of Glaciology, 8*(53), 215–223. https://doi.org/10.3189/S0022143000031208
Dreyfus, G. B., Jouzel, J., Bender, M. L., Landais, A., Masson-Delmotte, V., & Leuenberger, M. (2010). Firn processes and $\delta^{15}$N: potential for a gas-phase climate proxy. *Quaternary Science Reviews, 29*(1-2), 28-42. https://doi.org/10.1016/j.quascirev.2009.10.012
Epifanio, J. A., Brook, E. J., Buizert, C., Edwards, J. S., Sowers, T. A., Kahle, E. C., Severinghaus, J. P., Steig, E. J., Winski, D. A., Osterberg, E. C., Fudge, T. J., Aydin, M., Hood, E., Kalk, M., Kreutz, K. J., Ferris, D. G., & Kennedy, J. A. (2020). The SP19 chronology for the South Pole Ice Core–Part 2: gas chronology, $\Delta$age, and smoothing of atmospheric records. *Climate of the Past, 16*(6), 2431–2444. https://doi.org/10.5194/cp-16-2431-2020
EPICA Community Members. 2004. Eight glacial cycles from an Antarctic ice core. *Nature, 429*, 623–628. https://doi.org/10.1038/nature02599
Fausto, R. S., Box, J. E., Vandecrux, B. R. M., van As, D., Steffen, K., MacFerrin, M. J., Charalampidis, C., et al. (2018). A snow density dataset for improving surface boundary conditions in Greenland ice sheet firn modeling. *Frontiers in Earth Science, 6*, 51. https://doi.org/10.3389/feart.2018.00051
Forsberg, R., Olesen, A. V., Ferraccioli, F., Jordan, T., Corr, H., & Matsuoka, K. (2017). PolarGap 2015/16: Filling the GOCE polar gap in Antarctica and ASIRAS flight around South Pole. Radar grids available at: *ftp : //ftp.bas.ac.uk/tomj/PolarGAP/PolarGAP_radar_grids.zip*
Freitag, J., Kipfstuhl, S., Laepple, T., & Wilhelms, F. (2013). Impurity-controlled densification: a new model for stratified polar firn. *Journal of Glaciology, 59*(218), 1163–1169. https://doi.org/10.3189/2013JoG13J042
Fudge, T. J., Waddington, E. D., Conway, H., Lundin, J. M. D., & Taylor, K. (2014). Interpolation methods for Antarctic ice-core timescales: application to Byrd, Siple Dome and Law Dome ice cores. *Climate of the Past, 10*(3), 1195–1209. https://doi.org/10.5194/cp-10-1195-2014
Fudge, T. J., Markle, B. R., Cuffey, K. M., Buizert, C., Taylor, K. C., Steig, E. J., Koutnik, M., et al. (2016). Variable relationship between accumulation and temperature in West Antarctica for the past 31,000 years. *Geophysical Research Letters, 43*(8), 3795–3803. https://doi.org/10.1002/2016GL068356
Fudge, T. J., Biyani, S. C., Clemens-Sewall, D., & Hawley, R. L. (2019). Constraining geothermal flux at coastal domes of the Ross Ice Sheet, Antarctica. *Geophysical Research Letters, 46*(22), 13090–13098. https://doi.org/10.1029/2019GL084332

Fudge, T. J., Lilien, D. A., Koutnik, M., Conway, H., Stevens, C. M., Waddington, E. D., Steig, E. J., Schauer, A. J., & Holschuh, N. (2020). Advection and non-climate impacts on the South Pole Ice Core. *Climate of the Past, 16*, 819–832. https://doi.org/10.5194/cp-16-819-2020

Gades, A. M., Raymond, C. F., Conway, H., & Jacobel, R. W., (2000). Bed properties of Siple Dome and adjacent ice streams West Antarctica, inferred from radio-echo sounding measurements. *Journal of Glaciology, 46*(152), 88–94. https://doi.org/10.3189/172756500781833467

Gelman, A., Roberts, G. & Gilks W. (1996). Efficient Metropolis jumping rules, in Bayesian Statistics 5, Berger, J. O., Bernardo, J. M., Dawid, A. P. and Smith, A. F. M. (eds), Oxford University Press.

Gkinis, V., Simonsen, S. B., Buchardt, S. L., White, J. W. C., & Vinther, B. M. (2014). Water isotope diffusion rates from the NorthGRIP ice core for the last 16,000 years - glaciological and paleoclimatic implications. *Earth and Planetary Science Letters, 405*, 132–141. https://doi.org/10.1016/j.epsl.2014.08.022

Gkinis, V., Holme, C., Kahle, E.C., Stevens, C.M., Steig, E.J., & Vinther, B.M. (2021). Numerical experiments on firn isotope diffusion with the Community Firn Model. *Journal of Glaciology, 67*(263), 450-472. https://doi.org/10.1017/jog.2021.1

Golledge, N. R., Menviel, L., Carter, L., Fogwill, C. J., England, M. H., Cortese, G., & Levy, R. H. (2014). Antarctic contribution to meltwater pulse 1A from reduced Southern Ocean overturning. *Nature Communications, 5*(1), 1–10. https://doi.org/10.1038/ncomms6107

Goujon, C., Barnola, J. M., & Ritz, C. (2003). Modeling the densification of polar firn including heat diffusion: Application to close-off characteristics and gas isotopic fractionation for Antarctica and Greenland sites. *Journal of Geophysical Research: Atmospheres, 108*(D24). https://doi.org/10.1029/2002JD003319

Grachev, A. M., & Severinghaus, J. P. (2003). Laboratory determination of thermal diffusion constants for $^{29}N_2/^{28}N_2$ in air at temperatures from 60 to 0 C for reconstruction of magnitudes of abrupt climate changes using the ice core fossil–air paleothermometer. *Geochimica et Cosmochimica Acta, 67*(3), 345–360. https://doi.org/10.1016/S0016-7037(02)01115-8

Gudmundsson, G. H., & Raymond, M. (2008). On the limit to resolution and information on basal properties obtainable from surface data on ice streams. *The Cryosphere, 2*(3), 413–445. https://doi.org/10.5194/tc-2-167-2008

Guillevic, M., Bazin, L., Landais, A., Kindler, P., Orsi, A., Masson-Delmotte, V., Martinerie, P., et al. (2013). Spatial gradients of temperature, accumulation and $\delta^{18}$O-ice in Greenland over a series of Dansgaard-Oeschger events. *Climate of the Past, 9*(3), 1029–1051. https://doi.org/10.5194/cp-9-1029-2013

Hammer, C. U., Clausen, H. B., Dansgaard, W., Gundestrup, N., Johnsen, S. J., & Reeh, N. (1978). Dating of Greenland ice cores by flow models, isotopes, volcanic debris, and continental dust. *Journal of Glaciology, 20*(82), 3–26. https://doi.org/10.3189/S0022143000021183

Herron, M. M., & Langway, C. C. (1980). Firn densification: an empirical model. *Journal of Glaciology, 25*(93), 373–385. https://doi.org/10.3189/S0022143000015239

Holme, C., Gkinis, V., & Vinther, B. M. (2018). Molecular diffusion of stable water isotopes in polar firn as a proxy for past temperatures. *Geochimica et Cosmochimica Acta, 225*, 128–145. https://doi.org/10.1016/j.gca.2018.01.015

Huber, C., Leuenberger, M., Spahni, R., Flückiger, J., Schwander, J., Stocker, T. F., Jouzel, J., et al. (2006). Isotope calibrated Greenland temperature record over Marine Isotope Stage 3 and its relation to $CH_4$. *Earth and Planetary Science Letters, 243*(3-4), 504–519. https://doi.org/10.1016/j.epsl.2006.01.002

Johnsen, S. J. (1977). Stable isotope homogenization of polar firn and ice, in *Proc. of Symp. on Isotopes and Impurities in Snow and Ice*, pp. 210–219, Int. Assoc. of Hydrol. Sci., Gentbrugge, Belgium.

Johnsen, S. J., Clausen, H. B., Cuffey, K. M., Hoffmann, G., Schwander, J., & Creyts, T. (2000). Diffusion of stable isotopes in polar firn and ice: The isotope effect in firn diffusion. T. Hondoh (Ed.), *Physics of Ice Core Records*, Hokkaido University Press, Sapporo (2000), pp. 121–140.

Jones, T. R., Cuffey, K. M., White, J. W. C., Steig, E. J., Buizert, C., Markle, B. R., McConnell, J. R., & Sigl, M. (2017a). Water isotope diffusion in the WAIS Divide ice core during the Holocene and last glacial. *Journal of Geophysical Research: Earth Surface, 122*(1), 290–309. https://doi.org/10.1002/2016JF003938

Jones, T. R., White, J. W. C., Steig, E. J., Vaughn, B. H., Morris, V., Gkinis, V., Markle, B. R., & Schoenemann, S. W. (2017b). Improved methodologies for continuous flow analysis of stable water isotopes in ice cores. *Atmospheric Measurement Techniques, 10*, 617–632. https://doi.org/10.5194/amt-10-617-2017

Jordan, T. A., Martin, C., Ferraccioli, F., Matsuoka, K., Corr, H., Forsberg, R., Olesen, A., & Siegert, M. (2018). Anomalously high geothermal flux near the South Pole. *Scientific Reports, 8*(1), 1–8. https://doi.org/10.1038/s41598-018-35182-0

Jouzel, J., Barkov, N. I., Barnola, J. M., Bender, M., Chappellaz, J., Genthon, C., Raynaud, D., et al. (1993). Extending the Vostok ice-core record of palaeoclimate to the penultimate glacial period. *Nature, 364*(6436), 407–412. https://doi.org/10.1038/364407a0

Jouzel, J., Vimeux, F., Caillon, N., Delaygue, G., Hoffmann, G., Masson-Delmotte, V., & Parrenin, F. (2003). Magnitude of isotope/temperature scaling for interpretation of central Antarctic ice cores. *Journal of Geophysical Research: Atmospheres*, 108(D12). https://doi.org/10.1029/2002JD002677

Jouzel, J., Masson-Delmotte, V., Cattani, O., Dreyfus, G., Falourd, S., Hoffmann, G., Fischer, H., et al. (2007). Orbital and millennial Antarctic climate variability over the past 800,000 years. *Science, 317*(5839), 793–796. https://doi.org/10.1126/science.1141038

Kahle, E. C., Holme, C., Jones, T. R., Gkinis, V., & Steig, E. J. (2018). A generalized approach to estimating diffusion length of stable water isotopes from ice-core data. *Journal of Geophysical Research: Earth Surface, 123*(10), 2377–2391. https://doi.org/10.1029/2018JF004764

Kahle, E. C. (2020). Climate reconstructions from ice cores: New techniques to understand the information preserved in the South Pole ice core (Doctoral dissertation, University of Washington, Seattle, USA). http://hdl.handle.net/1773/45398

Khan, A., Mosegaard, K., & Rasmussen, K. L. (2000). A new seismic velocity model for the Moon from a Monte Carlo inversion of the Apollo lunar seismic data. *Geophysical Research Letters, 27*(11), 1591–1594. https://doi.org/10.1029/1999GL008452

Kindler, P., Guillevic, M., Baumgartner, M. F., Schwander, J., Landais, A., & Leuenberger, M. (2014). Temperature reconstruction from 10 to 120 kyr b2k from the NGRIP ice core. *Climate of the Past, 10*(2), 887–902. https://doi.org/10.5194/cp-10-887-2014

Koutnik, M. R., Fudge, T. J., Conway, H., Waddington, E. D., Neumann, T. A., Cuffey, K. M., Taylor, K. C., et al. (2016). Holocene accumulation and ice flow near the West Antarctic Ice Sheet Divide ice core site. *Journal of Geophysical Research: Earth Surface, 121*(5), 907–924. https://doi.org/10.1002/2015JF003668

Lamb, K. D., Clouser, B. W., Bolot, M., Sarkozy, L., Ebert, V., Saathoff, H., Mohler, O., & Moyer, E. J. (2017). Laboratory measurements of $HDO/H_2O$ isotopic fractionation during ice deposition in simulated cirrus clouds. *Proceedings of the National Academy of Sciences, 114*(22), 5612–5617. https://doi.org/10.1073/pnas.1618374114

Landais, A., Barnola, J.M., Kawamura, K., Caillon, N., Delmotte, M., van Ommen, T., Dreyfus, G., Jouzel, J., Masson-Deltmotte, V., Minster, B., Freitag, J., Leuenberger, M., Schwander, J., Huber, C., Etheridge, D., & Morgan, V. (2006). Firn-air $\delta^{15}$N in modern polar sites and glacial-interglacial ice: a model-data mismatch during glacial periods in Antarctica? *Quaternary Science Reviews, 25*(1-2), 499–62. https://doi.org/10.1016/j.quascirev.2005.06.007

Lazzara, M. A., Keller, L. M., Markle, T., & Gallagher, J. (2012). Fifty-year Amundsen–Scott South Pole station surface climatology. *Atmospheric Research*, 118, 240–259. https://doi.org/10.1016/j.atmosres.2012.06.027

Lee, J.-E., Fung, I., DePaolo, D. J., & Otto-Bliesner, B. (2008). Water isotopes during the Last Glacial Maximum: New general circulation model calculations. *Journal of Geophysical Research, 113*(D19). https://doi.org/10.1029/2008JD009859

Li, J., & Zwally, H. J. (2015). Response times of ice-sheet surface heights to changes in the rate of Antarctic firn compaction caused by accumulation and temperature variations. *Journal of Glaciology, 61*(230), 1037–1047. https://doi.org/10.3189/2015JoG14J182

Ligtenberg, S. R. M., Helsen, M. M., & Van den Broeke, M. R. (2011). An improved semi-empirical model for the densification of Antarctic firn. *The Cryosphere, 5*, 809–819. https://doi.org/10.5194/tc-5-809-2011

Lilien, D. A., Fudge, T. J., Koutnik, M. R., Conway, H., Osterberg, E. C., Ferris, D. G., Stevens, C. M., et al. (2018). Holocene Ice-Flow Speedup in the Vicinity of the South Pole. *Geophysical Research Letters, 45*(13), 6557–6565. https://doi.org/10.1029/2018GL078253

Looyenga, H. (1965). Dielectric constants of heterogeneous mixtures. *Physica, 31*(3), 401–406. https://doi.org/10.1016/0031-8914(65)90045-5

Lorius, C., Jouzel, J., Raynaud, D., Hansen, J., & Le Treut, H. (1990). The ice-core record: climate sensitivity and future greenhouse warming. *Nature, 347*(6289), 139–145. https://doi.org/10.1038/347139a0

Lundin, J. M., Stevens, C. M., Arthern, R., Buizert, C., Orsi, A., Ligtenberg, S. R., Harris, P., et al. (2017). Firn Model Intercomparison Experiment (FirnMICE). *Journal of Glaciology, 63*(239), 401–422. https://doi.org/10.1017/jog.2016.114

Luz, B., & Barkan, E. (2010). Variations of $^{17}$O/$^{16}$O and $^{18}$O/$^{16}$O in meteoric waters. *Geochimica et Cosmochimica Acta, 74*(22), 6276–6286. https://doi.org/10.1016/j.gca.2010.08.016

MacAyeal, D. R. (1993). Binge/purge oscillations of the Laurentide ice sheet as a cause of the North Atlantic's Heinrich events. *Paleoceanography, 8*(6), 775–784. https://doi.org/10.1029/93PA02200

Majoube, B. (1970). Fractionation factor of $^{18}$O between water vapour and ice. *Nature, 226*, 1242. https://doi.org/10.1038/2261242a0

Markle, B. R. (2017). *Climate dynamics revealed in ice cores: advances in techniques, theory, and interpretation* (Thesis (PH. D.) – University of Washington, 208 pp.). http://hdl.handle.net/1773/40391

Martinerie, P., Lipenkov, V. Y., Raynaud, D., Chappellaz, J., Barkov, N. I., % Lorius, C. (1994). Air content paleo record in the Vostok ice core (Antarctica): A mixed record of climatic and glaciological parameters. *Journal of Geophysical Research, 99*(D5), 10565. https://doi.org/10.1029/93JD03223

Masson-Delmotte, V., Jouzel, J., Landais, A., Stievenard, M., Johnsen, S.J., White, J. W. C., Werner, M., Sveinbjornsdottir, A. and Fuhrer, K. (2005). GRIP deuterium excess reveals rapid and orbital-scale changes in Greenland moisture origin. *Science, 309*, 118–121. https://doi.org/10.1126/science.1108575

Masson-Delmotte, V., Kageyama, M., Braconnot, P., Charbit, S., Krinner, G., Ritz, C., Gladstone, R. M., et al. (2006). Past and future polar amplification of climate change: climate model intercomparisons and ice-core constraints. *Climate Dynamics, 26*(5), 513–529. https://doi.org/10.1007/s00382-005-0081-9

Masson-Delmotte, V., Hou, S., Ekaykin, A., Jouzel, J., Aristarain, A., Bernardo, R. T., Frezzotti, M., et al. (2008). A review of Antarctic surface snow isotopic composition: Observations, atmospheric circulation, and isotopic modeling. *Journal of Climate, 21*(13), 3359–3387. https://doi.org/10.1175/2007JCLI2139.1

Metropolis, N., Rosenbluth, A. W., Rosenbluth, M. N., Teller, A. H., & Teller, E. (1953). Equation of state calculations by fast computing machines. *The Journal of Chemical Physics, 21*(6), 1087–1092. https://doi.org/10.1063/1.1699114

Monnin, E., Steig, E. J., Siegenthaler. U., Kawamura, K., Schwander, J., Stauffer, B., Morse, D. L., Stocker, T. F., Barnola, J. M., Bellier, B., Raynaud, D., & Fischer, H. (2004). Evidence for substantial accumulation rate variability in Antarctica during the Holocene through synchronization of $CO_2$ in the Taylor Dome, Dome C and DML ice cores. *Earth and Planetary Science Letters, 224*, 45–54. https://doi.org/10.1016/j.epsl.2004.05.007

Mosegaard, K., & Tarantola, A. (1995). Monte Carlo sampling of solutions to inverse problems. *Journal of Geophysical Research: Solid Earth, 100*(B7), 12431–12447. https://doi.org/10.1029/94JB03097

Mosegaard, K. (1998). Resolution analysis of general inverse problems through inverse Monte Carlo sampling. *Inverse Problems, 14*(3), 405. https://doi.org/10.1088/0266-5611/14/3/004

Mosegaard, K., & Tarantola, A. (2002). Probabilistic approach to inverse problems. In W. Lee, P. Jennings, C. Kisslinger, & H. Kanamori (Eds.), *International Handbook of Earthquake & Engineering Seismology (Part A)* (237–265). Academic Press.

Mosegaard, K., & Sambridge, M. (2002). Monte Carlo analysis of inverse problems. *Inverse problems, 18*(3), R29. https://doi.org/10.1088/0266-5611/18/3/201

Neumann, T. A., Conway, H., Price, S., Waddington, E. D., & Morse, D. L. (2008). Holocene accumulation and ice-sheet dynamics in central West Antarctica. *Journal of Geophysical Research, 113*, (F2). https://doi.org/10.1029/2007JF000764

Nye, J. (1963). Correction factor for accumulation measured by the thickness of the annual layers in an ice sheet. *Journal of Glaciology, 4*(36), 785–788. https://doi.org/10.3189/S0022143000028367

Parrenin, F., Remy, F., Ritz, C., Siegert, M. J., & Jouzel, J. (2004). New modeling of the Vostok ice flow line and implication of the glaciological chronology of the Vostok ice core. *Journal of Geophysical Research, 109*, (D20). https://doi.org/10.1029/2004JD004561

Parrenin, F., Barker, S., Blunier, T., Chappellaz, J., Jouzel, J., Landais, A., Veres, D., et al. (2012). On the gas-ice depth difference (Δdepth) along the EPICA Dome C ice core. *Climate of the Past, 8*(2), 1089–1131. https://doi.org/10.5194/cpd-8-1089-2012

Parrenin, F., Masson-Delmotte, V., Kohler, P., Raynaud, D., Paillard, D., Schwander, J., Jouzel, J., et al. (2013). Synchronous change of atmospheric CO2 and Antarctic temperature during the last deglacial warming. *Science, 339*(6123), 1060–1063. https://doi.org/10.1126/science.1226368

Peltier, W.R. (2004). Global glacial isostasy and the surface of the ice-age Earth: The ICE-5G (VM2) Model and GRACE. *Ann. Rev. Earth and Planet. Sci., 32*, 111–149. https://doi.org/10.1146/annurev.earth.32.082503.144359

Pollard, D., & DeConto, R. M. (2009). Modelling West Antarctic ice sheet growth and collapse through the past five million years. *Nature, 458*(7236), 329–332. https://doi.org/10.1038/nature07809

Price, P. B., Nagornov, O. V., Bay, R., Chirkin, D., He, Y., Miocinovic, P., Richards, A., Woschnagg, K., Koci, B., & Zagorodnov, V., (2002). Temperature profile for glacial ice at the South Pole: implications for life in a nearby subglacial Lake. *Proceedings of the National Academy of Sciences, 99*(12), 7844–7847. https://doi.org/10.1073/pnas.082238999

Raymond, C. (1983). Deformation in the vicinity of ice divides. *Journal of Glaciology, 29*(103), 357—373. https://doi.org/10.3189/S0022143000030288

Roy, K., & Peltier, W. R. (2015). Glacial isostatic adjustment, relative sea level history and mantle viscosity: reconciling relative sea level model predictions for the US East coast with geological constraints. *Geophysical Journal International, 201*(2), 1156–1181. https://doi.org/10.1093/gji/ggv066.

Schoenemann, S. W., Steig, E. J., Ding, Q., Markle, B. R., & Schauer, A. J. (2014). Triple water-isotopologue record from WAIS Divide, Antarctica: Controls on glacial-interglacial changes in $^{17}O_{excess}$ of precipitation. *Journal of Geophysical Research: Atmospheres, 119*(14), 8741–8763. https://doi.org/10.1002/2014JD021770

Schwander, J., & Stauffer, B. (1984). Age difference between polar ice and the air trapped in its bubbles. *Nature, 311*(5981), 45–47. https://doi.org/10.1038/311045a0

Schwander, J., Stauffer, B., & Sigg, A. (1988). Air mixing in firn and the age of the air at pore close-off. *Annals of Glaciology, 10*, 141–145. https://doi.org/10.3189/S0260305500004328

Schwander, J. The transformation of snow to ice and the occlusion of gases, in: H. Oeschger, C.C. Langway Jr. (Eds.), The Environmental Record in Glaciers and Ice Sheets, John Wiley, New York, 1989, pp. 53–67.

Severinghaus, J. P., Sowers, T., Brook, E. J., Alley, R. B., & Bender, M. L. (1998). Timing of abrupt climate change at the end of the Younger Dryas interval from thermally fractionated gases in polar ice. *Nature, 391*(6663), 141–146. https://doi.org/10.1038/34346

Severinghaus, J. P., Grachev, A., & Battle, M. (2001). Thermal fractionation of air in polar firn by seasonal temperature gradients. *Geochemistry, Geophysics, Geosystems, 2*(7). https://doi.org/10.1029/2000GC000146

Severinghaus, J. (2019) "South Pole (SPICECORE) $^{15}$N, $^{18}$O, $O_2/N_2$ and Ar/N)2" U.S. Antarctic Program (USAP) Data Center. https://doi.org/10.15784/601152.

Sigl, M., Fudge, T. J., Winstrup, M., Cole-Dai, J., Ferris, D., McConnell, J. R., Bisiaux, M., et al. (2016). The WAIS Divide deep ice core WD2014 chronology–Part 2: Annual-layer counting (0–31 ka BP). *Climate of the Past, 12*(3), 769–786. https://doi.org/10.5194/cp-12-769-2016

Sime, L. C., Hopcroft, P. O., & Rhodes, R. H. (2019). Impact of abrupt sea ice loss on Greenland water isotopes during the last glacial period. *Proceedings of the National Academy of Sciences, 116*(10), 4099–4104. https://doi.org/10.1073/pnas.1807261116

Simonsen, S. B., Johnsen, S. J., Popp, T. J., Vinther, B. M., Gkinis, V., & Steen-Larsen, H. C. (2011). Past surface temperatures at the NorthGRIP drill site from the difference in firn diffusion of water isotopes. *Climate of the Past, 7*(4), 1327–1335. https://doi.org/10.5194/cp-7-1327-2011

Simonsen, S. B., Stenseng, L., Ađalgeirsdóttir, G., Fausto, R. S., Hvidberg, C. S., & Lucas-Picher, P. (2013). Assessing a multilayered dynamic firn-compaction model for Greenland with ASIRAS radar measurements. *Journal of Glaciology, 59*(215), 545–558. https://doi.org/10.3189/2013JoG12J158

Sowers, T., Bender, M., Raynaud, D., & Korotkevich, Y. S. (1992). $\delta^{15}$N of $N_2$ in air trapped in polar ice: A tracer of gas transport in the firn and a possible constraint on ice age-gas age differences. *Journal of Geophysical Research: Atmospheres, 97*(D14), 15683–15697. https://doi.org/10.1029/92JD01297

Steen-Larsen, H. C., Waddington, E. D., & Koutnik, M. R. (2010). Formulating an inverse problem to infer the accumulation-rate pattern from deep internal layering in an ice sheet using a Monte Carlo approach. *Journal of Glaciology, 56*(196), 318–332. https://doi.org/10.3189/002214310791968476

Steig, E. J., Grootes, P. M., & Stuiver, M. (1994). Seasonal precipitation timing and ice core records. *Science, 266*, 1885–1886. https://doi.org/10.1126/science.266.5192.1885

Steig, E. J., Ding, Q., White, J. W. C., Küttel, M., Rupper, S. B., Neumann, T. A., Neff, P. D., Gallant, A. J. E., Mayewski, P. A., Taylor, K. C., Hoffmann, G., Dixon, D. A., Schoenemann, S., Markle B. M., Schneider, D. P., Fudge, T. J., Schauer, A. J., Teel, R. P., Vaughn, B., Burgener, L., Williams, J., & Korotkikh, E. (2013). Recent climate and ice-sheet change in West Antarctica compared to the past 2000 years. *Nature Geoscience, 6*(5), 372. https://doi.org/10.1038/ngeo1778

Steig, E. J., Gkinis, V., Schauer, A. J., Schoenemann, S. W., Samek, K., Hoffnagle, J., Tan, S. M., et al. (2014). Calibrated high-precision $^{17}$O-excess measurements using cavity ring-down spectroscopy with laser-current-tuned cavity resonance. *Atmospheric Measurement Techniques, 7*, 2421–2435. https://doi.org/10.5194/amt-7-2421-2014

Steig, E. J., T. R. Jones, A. J. Schauer, E. C. Kahle, V. A. Morris, B. H. Vaughan, L. Davidge, & White, J. W. C. (2021). Continuous-flow analysis of $\delta^{17}$O, $\delta^{18}$O, and $\delta$D of $H_2O$ on an ice core from the South Pole. *Frontiers in Earth Science, 9*, 640292. https://doi.org/10.3389/feart.2021.640292

Stevens, C. M., Verjans, V., Lundin, J., Kahle, E. C., Horlings, A. N., Horlings, B. I., & Waddington, E. D. (2020). The Community Firn Model (CFM) v1. 0. *Geoscientific Model Development, 13*(9), 4355–4377. https://doi.org/10.5194/gmd-13-4355-2020

Tarantola, A. (1987). Inverse problem theory: Methods for data fitting and model parameter estimation. *Elsevier Science*, Amsterdam.

van der Wel, G., Fischer, H., Oerter, H., Meyer, H., & Meijer, H. A. J. (2015). Estimation and calibration of the water isotope differential diffusion length in ice core records. *The Cryosphere, 9*(4), 1601–1616. https://doi.org/10.5194/tc-9-1601-2015

Veres, D., Bazin, L., Landais, A., Toyé Mahamadou Kele, H., Lemieux-Dudon, B., Parrenin, F., Chappellaz, J., et al. (2013). The Antarctic ice core chronology (AICC2012): an optimized multi-parameter and multi-site dating approach for the last 120 thousand years. *Climate of the Past, 9*(4), 1733–1748. https://doi.org/10.5194/cp-9-1733-2013

WAIS Divide Project Members (2013). Onset of deglacial warming in West Antarctica driven by local orbital forcing. *Nature, 500*(7463), 440–444. https://doi.org/10.1038/nature12376

Werner, M., Mikolajewicz, U., Heimann, M., & Hoffmann, G. (2000). Borehole versus isotope temperatures on Greenland: Seasonality does matter. *Geophysical Research Letters, 27*(5), 723–726. https://doi.org/10.1029/1999GL006075

Werner, M., Jouzel, J., Masson-Delmotte, V., & Lohmann, G. (2018). Reconciling glacial Antarctic water stable isotopes with ice sheet topography and the isotopic paleothermometer. *Nature Communications, 9*(1), 1-10. https://doi.org/10.1038/s41467-018-05430-y

Whillans, I. M., & Grootes P. M. (1985). Isotopic diffusion in cold snow and firn. *Journal of Geophysical Research, 90*(D2), 3910–3918. https://doi.org/10.1029/JD090iD02p03910

Whitehouse, P. L., Bentley, M. J., & Le Brocq, A. M. (2012). A deglacial model for Antarctica: geological constraints and glaciological modelling as a basis for a new model of Antarctic glacial isostatic adjustment. *Quaternary Science Reviews, 32*, 1–24. https://doi.org/10.1016/j.quascirev.2011.11.016

Winski, D. A., Fudge, T. J., Ferris, D. G., Osterberg, E. C., Fegyveresi, J. M., Cole-Dai, J., Buizert, C., Epifanio, J., Brook, E. J., Beaudette, R., Severinghaus, J., Sowers, T., Steig, E. J., Kahle, E. C., Jones, T. R., Morris, V., Aydin, M., Nicewonger, M. R., Casey, K. A., Alley, R. B., Waddington, E. D., & Iverson, N.

A. (2019). The SP19 chronology for the South Pole Ice Core–Part 1: volcanic matching and annual layer counting. *Climate of the Past, 15*(5), 1793–1808. https://doi.org/10.5194/cp-15-1793-2019

York, D., Evensen, N. M., Martınez, M. L., & De Basabe Delgado, J. (2004). Unified equations for the slope, intercept, and standard errors of the best straight line. *American Journal of Physics, 72*(3), 367–375. https://doi.org/10.1119/1.1632486

# Reconstruction of Temperature, Accumulation Rate, and Layer Thinning from an Ice Core at South Pole Using a Statistical Inverse Method

Emma C. Kahle[1], Eric J. Steig[1], Tyler R. Jones[2], T.J. Fudge[1], Michelle R. Koutnik[1], Valerie A. Morris[2], Bruce H. Vaughn[2], Andrew J. Schauer[1], C. Max Stevens[1], Howard Conway[1], Edwin D. Waddington[1], Christo Buizert[3], Jenna Epifanio[3], James W. C. White[2]

[1]Department of Earth and Space Sciences, University of Washington, Seattle WA 98195, USA

[2]Institute of Arctic and Alpine Research, University of Colorado, Boulder CO 80309, USA

[3]College of Earth Ocean and Atmospheric Sciences, Oregon State University, Corvallis OR 97331, USA

## Contents of this file



---

Corresponding author: Emma C. Kahle, Department of Earth and Space Sciences, University of Washington, Seattle WA 98195, USA. (eckahle@uw.edu)

**Introduction.** This supporting information document provides further details on methods used in the analysis described in the main text. We include information about:

S1. Diffusion-length data and modeling

S2. Inverse methods

S3. Sensitivity tests

S4. Ice-flow modeling

S5. The $\delta^{15}$N-based thinning function

## Text S1. Diffusion-length data and modeling

*S1.1 Corrections to diffusion-length data*

We make two corrections to the estimates of diffusion length calculated from the spectra of the water-isotope data.

First, we correct for the effect on the water-isotope data from the continuous-flow-analysis (CFA) measurement system. As melted ice samples are transported through the tubing and reservoirs of the CFA system, some smoothing of the high-frequencies of the natural water-isotope variations occurs. This smoothing is minimized by design of the components of the CFA-system, but still impacts the measured signal. The extent of this system smoothing can be quantified by measuring the system response to a step change in isotopic value using laboratory-produced ice (Jones et al., 2017b). The system diffusion length for the CFA system used in this analysis is 0.07 cm for $\delta^{17}$O and $\delta^{18}$O, and 0.08 cm for $\delta$D (Jones et al., 2017b).

Second, we correct for the additional diffusion that occurred in the solid ice below the bottom of the firn, following Gkinis et al. (2014). To calculate the solid-ice diffusion length, we assume the modern borehole temperature profile $T(z)$ remains constant through time to find the diffusivity profile $D_{ice}(z)$, following Gkinis et al. (2014):

$$D_{ice}(z) = 9.2 \times 10^{-4} \times \exp\left(\frac{-7186}{T(z)}\right), \tag{1}$$

with $T(z)$ given in K and $D_{ice}(z)$ given in m$^2$ s$^{-1}$. For $T(z)$ at SPC14, we use borehole temperature measurements from the nearby neutrino observatory (Price et al., 2002).

The solid-ice diffusion length is also affected by vertical strain in the ice sheet. We assume a simple thinning function from a 1-D ice-flow model (Dansgaard and Johnsen, 1969) with a kink-height $h_0 = 0.2$ for this calculation. We describe the total thinning experienced by a layer $S(t)$ in a given time interval $t = 0$ to $t = t'$ as:

$$S(t') = \exp\left(\int_0^{t'} \dot{\epsilon}_z(t)dt\right), \tag{2}$$

where $\dot{\epsilon}_z(t)$ is the vertical strain rate calculated from the thinning function. The solid-ice diffusion length, $\sigma_{ice}$, is then calculated as (Gkinis et al., 2014):

$$\sigma_{ice}^2(t') = S(t')^2 \int_0^t 2D_{ice}(t)S(t)^{-2}dt. \tag{3}$$

To produce the corrected diffusion-length data set used in this analysis, we subtract in quadrature both the system diffusion length, $\sigma_{CFA}$, and the solid-ice diffusion length, $\sigma_{solid}$, from the total measured diffusion length, $\sigma_{meas}$:

$$\sigma^2 = \sigma_{meas}^2 - \sigma_{CFA}^2 - \sigma_{solid}^2. \tag{4}$$

The diffusion length $\sigma$ represents the diffusion that occurred within the firn column and that has experienced the effects of vertical strain in the ice sheet (*i.e.*, $\sigma = S(z)\sigma_{firn}$). Figure S1 shows the effect of these corrections on the estimated diffusion length.

*S1.2 Modeling firn diffusion length*

Within the forward model of the inverse problem, we model diffusion length in the firn column. We use the following values in calculating the diffusivity coefficients, $D_x$, for each water-isotope ratio:

$$D^{air}_{\delta^{18}O} = \frac{D^{air}}{1.0285} \qquad \text{(Johnsen et al., 2000)} \tag{5}$$

$$D^{air}_{\delta^{17}O} = \frac{D^{air}}{1.01466} \qquad \text{(Luz and Barkan, 2010)} \tag{6}$$

$$D^{air}_{\delta D} = \frac{D^{air}}{1.0251} \qquad \text{(Johnsen et al., 2000)} \tag{7}$$

where:

$$D^{air} = 0.211 \times 10^{-4} \times \left(\frac{T}{273.15}\right)^{1.94} \times \frac{P_0}{P} \quad \text{(Johnsen et al., 2000)} \tag{8}$$

is the diffusivity of water vapor in air. $T$ is temperature given in Kelvin and $P$ is the atmospheric pressure compared to a reference pressure of $P_0 = 1$ atm.

We use the following values in calculating the fractionation factors, $\alpha_x$, for each water-isotope ratio, for the equilibrium of water vapor over ice:

$$\alpha_{18} = \exp(\frac{11.839}{T} - 28.224 \times 10^{-3}) \qquad \text{(Majoube, 1970)} \tag{9}$$

$$\alpha_{17} = \exp(0.529 \times \log(\alpha_{18})) \qquad \text{(Barkan and Luz, 2007)} \tag{10}$$

$$\alpha_D = \exp(-0.0559 + \frac{13525}{T^2}) \qquad \text{(Lamb et al., 2017)} \tag{11}$$

The tortuosity parameter $\tau$ used in Equation 5 in the main text is given by (Schwander et al., 1988; Johnsen et al., 2000):

$$\frac{1}{\tau} = \begin{cases} 1 - b \times \left(\frac{\rho}{\rho_{ice}}\right)^2 & \text{, for } \rho \leq \frac{\rho_{ice}}{\sqrt{b}} \\ 0 & \text{, for } \rho > \frac{\rho_{ice}}{\sqrt{b}} \end{cases} \tag{12}$$

using a tortuosity parameter $b = 1.3$.

The solution to Equation 4 in the main text for the isotope profile at a given depth $z$ and time $t$ is given by:

$$\delta(z,t) = S(t)\frac{1}{\sigma\sqrt{2\pi}}\int_{-\infty}^{\infty}\delta(z,0)\exp\left(\frac{-(z-u)^2}{2\sigma^2}\right)du, \tag{13}$$

as described in (Gkinis et al., 2014) and fully derived in Kahle et al. (2020), where $\sigma$ is the diffusion length and the factor $S(t)$ is the total thinning a layer has experienced due to ice flow, as described in Equation 2 of this supplement.

## Text S2. Inverse methods

The statistical inverse method used in this work relates the three variables that span the model space with the three data variables that span the data space. We define the model space as a vector space with a dimension for each of the unknown input parameters; a particular point in the model space represents a specific set of input parameters $m$. The data space is defined similarly, where each data parameter in $d$ represents a dimension, and our observations $d_{obs}$ exist at a particular point in the data space. Because the data have measurement uncertainties, the “true” values in the data space may differ from $d_{obs}$.

Because we have three model parameters across 208 depth points (624 total unknown parameters), our problem spans a high dimensional model space, and an exhaustive search of all possible solutions $m$ is not practical. We limit the number of instances of $m$ to evaluate by using an importance-sampling algorithm. We use a Markov Chain Monte Carlo algorithm to combine *a priori* information about which solutions $m$ are plausible for realistic ice-sheet conditions and information from our data sets. This algorithm efficiently explores the parameter space by favoring instances of $m$ that are similar to those that have already produced good fits with the observations $d_{obs}$.

In this section, we describe the theoretical framework (S2.1 and S2.2) and the practical implementation (S2.3) of the inverse approach we use. In general, the solution of this type of inverse problem depends on the formulation of the problem, including what information is included in the constraints and how the output is analyzed. We detail below each of the choices that we make in our approach.

*S2.1 Bayesian framework*

We use a statistical Bayesian framework to solve this inverse problem. Rather than seek a single best-fit solution, we consider the likelihood of different solutions based on probability distributions within the parameter spaces of the data and the model. This framework combines *a priori* model parameter information with data measurement uncertainties. Unlike a regularization approach, such as Tikhonov regularization, a Bayesian approach does not require a subjective choice about how well the final set of solutions should fit the data (Tarantola, 1987; Steen-Larsen et al., 2010).

We characterize the *a priori* information describing the model inputs $m$ as a probability distribution in the model space. This distribution, denoted as $\rho_m(m)$, represents the likelihood of solutions $m$ based on data-independent prior knowledge about what values are realistic for that particular parameter (Mosegaard and Tarantola, 1995; Mosegaard & Sambridge, 2002). To produce the complete solution to the problem, the *a priori* information is combined with the likelihood function, which describes how well the output $d$ from a given solution $G(m)$ matches our observations $d_{obs}$. The likelihood function $L(m)$ is defined as (Mosegaard and Tarantola, 1995):

$$L(m) = C_L \exp(-M(m)), \tag{14}$$

where $C_L$ is a normalization constant and $M(m)$ is a misfit function that measures the deviation between $d$ and $d_{obs}$ in the data space.

The likelihood function $L(m)$ is combined with the *a priori* distribution $\rho_m(m)$ to define the *a posteriori* distribution $f(m)$ (Tarantola, 1987):

$$f(m) = C_f L(m) \rho_m(m). \tag{15}$$

Note that in our implementation, detailed in S2.3, we directly incorporate *a priori* information into the model space bounds and thus directly compare values of the misfit function $M(m)$ calculated for each solution $m$. Specific values for $C_L$, $C_f$, and $\rho_m$ are not required.

The *a posteriori* distribution $f(m)$ contains all the information we have to constrain the inverse problem and thus represents its complete solution. The region of maximum values of $f(m)$ denote the most likely solutions to the problem. This distribution may be Gaussian-like and simple to interpret, or may be multi-modal and require a more complex interpretation. We cannot produce this *a posteriori* distribution analytically, but we can sample its values at discrete points. For each solution $m$ that we test in our forward model $G$, we calculate a discrete value of $f(m)$.

*S2.2 Sampling strategy*

Our sampling strategy uses an algorithm to determine which solutions $m$ to test, with the goal of producing $f(m)$ after sufficient iterations (Mosegaard and Tarantola, 1995). The algorithm explores the model space by randomly stepping from one solution $m_i$ to a neighbor $m_j$. In each iteration, the algorithm follows two stages, designed such that it asymptotically produces $f(m)$ (Mosegaard, 1998; Mosegaard & Sambridge, 2002).

First, an exploration stage defines how the algorithm selects a proposal for $m_j$ given its starting place at $m_i$. The selection depends on how far in model space the algorithm is allowed to step in a single iteration. While the magnitude and direction of the step are determined randomly, the magnitude is scaled by a base step-size. The choice of base step-size balances the exploration of more of the model space (larger steps) with the exploration of regions that result in high values of $f(m)$ (smaller steps). In practice, we must tune the step size in order to strike this balance (*e.g.,* Steen-Larsen et al. (2010)).

Second, an exploitation stage defines the transition probability that the proposed step with be accepted. If the proposed step is rejected, the current solution $m_i$ is repeated for an additional iteration. The simplest choice for the transition probability is the Metropolis acceptance probability (Metropolis et al., 1953; Mosegaard, 1998; Mosegaard & Sambridge, 2002):

$$p_{accept} = min\left(1, \frac{f(m_j)}{f(m_i)}\right). \tag{16}$$

This formulation will always accept the proposed step to $m_j$ if the *a posteriori* distribution is greater at that point ($f(m_j) > f(m_i)$), but may still accept the proposed step even if the *a posteriori* distribution is smaller at that point ($f(m_j) < f(m_i)$) by a probability proportional to $\frac{f(m_j)}{f(m_i)}$. This design prevents the algorithm from getting stuck at a local maximum of $f(m)$, while still favoring samples from regions of the model space with a relatively high value of $f(m)$.

After sufficient iterations, the sampling of this algorithm will converge on $f(m)$. The number of iterations required for convergence, the convergence time, depends on the base step-size chosen. Step size is tuned to minimize the number of iterations required while appropriately sampling the model space. Related to the convergence time is the burn-in time, which refers to the number of iterations completed before the sampled values of $f(m)$ become relatively stationary. After this point, the algorithm continues to sample only highly likely solutions $m$. Prior work has found that after the burn-in time, the acceptance rate of the algorithm should be 25-50% (Gelman et al., 1996) in order to strike a balance between exploration (bigger steps) and efficiency (smaller steps).

*S2.3 Implementation of sampling*

To sample and estimate the *a posteriori* distribution, we implement the theory described above. We initiate the problem with our initial guess $m_1$ for each parameter and begin evaluating successive solutions from that point. Our sampling strategy uses Equation 16 and the associated ideas about sampling efficiency.

In the exploration stage of the algorithm, rather than perturb only one parameter within $m_i$ at a time, all 624 parameters (*i.e.,* values at each depth point for temperature, accumulation rate, and thinning function) are perturbed in each iteration. This design improves the efficiency of the algorithm. Each perturbation is constructed with the same low-frequency, red-noise slope in its power spectral density as that of a comparison data set. The comparison data set for temperature is the water-isotope record, for accumulation rate is a destrained version of the annual-layer thicknesses, and for the thinning function is a DJ-model output. Because in reality we expect temperature, accumulation rate, and thinning to vary smoothly through time, each proposed perturbation must vary smoothly as well. Furthermore, the $\Delta$age and diffusion-length data sets are inherently smooth because they integrate information over the depth of the firn column. To prevent spurious high-frequency noise from being introduced into the proposed solution $m$, we apply a low-pass filter to the perturbation. To the temperature and accumulation-rate perturbations, we apply a lowpass filter at a 3000-year period, which corresponds to the maximum value of $\Delta$age. We apply a lowpass filter at a 10,000-year period to the thinning-function perturbations because we expect the thinning function to be even smoother. The perturbations are then added to the previous accepted solution to generate the next proposed solution.

In the exploitation stage, the algorithm determines whether to accept the proposed solution $m_{i+1}$ by calculating and comparing the values of the *a posteriori* distribution at $m_i$ and $m_{i+1}$. Equation 15 describes how the *a posteriori* distribution is calculated from the likelihood function $L(m)$ and the *a priori* distribution $\rho(m)$. Because we have already incorporated our prior knowledge directly into the model space bounds, we simply compare the value of the likelihood function evaluated at $m_i$ and $m_{i+1}$ (Mosegaard, 1998):

$$p_{accept} = min\left(1, \frac{L(m_{i+1})}{L(m_i)}\right). \tag{17}$$

We define the likelihood function, as in Equation 14, with a misfit function $M(m)$ defined as (Khan et al., 2000; Mosegaard & Sambridge, 2002):

$$M(m) = \sum_n \frac{\left|d^{(n)}(m) - d^{(n)}_{obs}\right|}{\sigma_n}, \tag{18}$$

where $d^{(n)}(m)$ denotes the modeled output, $d^{(n)}_{obs}$ the observation, and $\sigma_n$ the standard deviation of the observation for the $n$th datum. This misfit function minimizes the influence of outliers, compared to a root-mean-square formulation.

We run the algorithm until we have 100,000 accepted samples of the *a posteriori* distribution. With an acceptance rate of 30-40%, this requires approximately 300,000 iterations in total. The burn-in time is reached after approximately 10,000 iterations, and we consider solutions $m$ only after this point. We repeat this process five times to account for any persistent impacts from early perturbations, combining all accepted solutions after the burn-in time to create the final set of results. Because only a small perturbation is made between iterations, successive iterations are correlated. Analysis of the *a posteriori* distribution requires a collection of statistically independent models, so we consider only a subset of all accepted models (Mosegaard, 1998; Dahl-Jensen et al., 1998). Through an autocorrelation analysis of the accepted models, we conclude that saving every 300th solution produces a statistically independent set. Out of a total of 500,000 accepted solutions, 1500 solutions are included in our analysis of the *a posteriori* distribution.

## Text S3. Sensitivity tests

### *S3.1 Sensitivity to Firn Model*

To evaluate the sensitivity of the results to the choice of firn model, we perform two sets of experiments comparing different firn models. First, we use the Community Firn Model (CFM) (Stevens et al., 2020; Gkinis et al., 2021) to calculate $\Delta$age using our full ensemble of accumulation-rate and temperature reconstructions as inputs for five different models: a dynamic version of Herron-Langway, Goujon et al. (2003), Li and Zwally (2015), Ligtenberg et al. (2011), and Simonsen et al. (2013). (Solving the full inverse problem with any of these dynamic models, which do not have analytical solutions, is impractical, but we address this issue in the second set of experiments below.) Comparison of the outputs of the five different models and the $\Delta$age data is given in Figure S2. The results show that while the Ligtenberg et al. (2011) and Li and Zwally (2015) models produce similar results for the glacial period, the Goujon et al. (2003) and Simonsen et al. (2013) models systematically underestimate $\Delta$age by about 500 years. As currently formulated, none of these models other than Herron-Langway are consistent with the modern depth-density profiles at South Pole. Because the accumulation rate and thinning function are tightly constrained by the diffusion-length and layer-thickness data, the only available free parameter that could be used to reconcile these other models with the empirical $\Delta$age data is temperature. For the Goujon et al. (2003) model, for example, adjusting the temperature to match $\Delta$age requires reducing the temperature by about 2°C in the glacial and by $> 3$°C in the Holocene; the latter is implausible and would require an even smaller glacial-interglacial temperature change than our reconstruction indicates. Thus, our choice of Herron-Langway is motivated by the fact that it produces results most consistent with multiple, independent, empirical constraints.

In a second set of experiments, we further examine the sensitivity of our results to the choice of firn model by implementing two of the models, Goujon et al. (2003) (GOU) and Ligtenberg et al. (2011) (LIG), within our inverse model framework. These two models are representative end-members (Figure S2). We use the CFM to run these models to steady state using a range of temperature and accumulation-rate pairs that span the climate of the SPC14 record. We save the model output in a format that is accessible from within the inverse procedure, allowing the appropriate firn age-depth-density profile to be used for the corresponding temperature and accumulation-rate value in each iteration.

Figure S3 shows the results of these experiments compared with the main result using the Herron-Langway analytic model (HLA). Both the GOU and LIG firn models produce lower temperatures throughout the record, lower accumulation-rate values in the Holocene, and slightly higher thinning function values through the Holocene and glacial transition, compared to the main HLA result. Although the Last Glacial Maximum (LGM) temperature in the GOU and LIG results is lower than that of the HLA result, the glacial-interglacial temperature change is similar for all three models, as shown in Figure S4. This shows that the relatively small glacial-interglacial change, one of the key results in this paper, is not a consequence of our model choice. Building on the result of the first set of firn-model experiments, it also further demonstrates that the HLA model is an appropriate model for South Pole.

*S3.2 Sensitivity to Measured Data Sets*

To determine the extent to which each of our three data sets affects the results, we tested our approach by excluding different combinations of the data sets. We used the same inverse framework as before, but took into account only how well the output $d$ matches the data observations $d_{obs}$ for the data sets included in that test. Excluding all data sets evaluates the effect of the perturbation construction by resampling the *a priori* distribution (Mosegaard and Tarantola, 2002). Figure S5 illustrates that this null test, in which there are *no* constraints from the data, successfully recovers the prior; the mean of the *a priori* distribution is approximately the mean of the bounded model space. This result shows that no spurious information is produced by the sampling procedure.

Building up from the null test, we tested two suites of three runs each to evaluate the sensitivity of results to each of the data sets. The first suite includes only one data set at a time, and the second suite includes two data sets at a time. The results from both suites are similar, and we show here only the results from the second. Figure S6 shows the mean solution from each run of the second suite: excluding $\Delta$age (purple), excluding diffusion length (blue), and excluding layer thickness (green), compared alongside the full results including all parameters (black). The right three panels show the effect on the fit of the data parameters, producing, as expected, the worst fit to each data set when that information is excluded from the problem. The left three panels of Figure S6 show how the exclusion of each data set impacts the mean of each set of solutions. The result for the thinning function suggests that, from 40 - 54 ka, the diffusion-length record pulls the thinning function to greater values (less thinning), while the layer thickness pulls the thinning function to smaller values (more thinning). The accumulation-rate reconstruction is most sensitive to diffusion length and layer thickness. To assess the sensitivity of the temperature reconstruction, we ran our two suites of sensitivity tests again, this time prescribing accumulation rate to the mean solution. Figure S7 shows the results for temperature for each of the four types of tests. The results suggest that $\Delta$age is most important for temperature at ages younger than 35 ka. At ages older than 35 ka, no single data set is most important for temperature, but the results of the 2-parameter suite suggest that the combined information from diffusion length and layer thickness has the greatest impact on the temperature result.

Additionally, we tested the impact of the diffusion-length data set on the temperature result by isolating the temperature-dependence of the water-isotope diffusion model within the forward model. We used a linear step-change input for temperature within the diffusion model (solid magenta line in temperature panel of Figure S8), not allowing changes of temperature in each iteration to influence the misfit of the modeled diffusion lengths to the data set. These results (blue shading in Figure S8) show a significant difference in the results for all three variables (temperature, accumulation rate, and thinning function), particularly during the LGM. This occurs because the fixed temperature we use for the diffusivity increases the modeled firn diffusion length, requiring more thinning to match the diffusion-length data. To accommodate the increased thinning, accumulation rate must increase to match the layer-thickness data. To compensate for a higher accumulation rate, a colder temperature is required to match the Δage data. In this particular example, the glacial-interglacial temperature change is reduced by 1.4°C from the main results, a significant difference. Setting a constant diffusion temperature colder than the main result would have the opposite effect. This sensitivity test demonstrates that the water-isotope diffusion model provides a critical constraint on temperature, comparable in significance to Δage.

*S3.3 Sensitivity to $\delta^{15}N$ data*

As detailed in Section 5.4 of the main text, we use the $\delta^{15}$N-based diffusive column height (DCH) to assess the impact of the $\delta^{15}$N data on our main result. We run a global search algorithm over a range of temperature and accumulation-rate values to find those that are in agreement with the $\delta^{15}$N-based DCH. The temperature and accumulation-rate values included in our global search are defined by a small range about the corresponding mean values in the main reconstruction. For temperature values, we define the range as ±5°C, and for accumulation-rate values, we define the range as $\pm 0.01$ m a$^{-1}$. Given the variability in each parameter, the temperature range is relatively larger than the accumulation-rate range, which is appropriate since the accumulation rate is fairly well constrained.

Accompanying Figure 5 in the main text, Figure S9 shows the DCH as calculated with the accumulation-rate and temperature results shown in Figure 5. The red shading, corresponding to the red shading in Figure 5, shows the DCH calculated when the $\delta^{15}$N constraint is applied to the accumulation rate and temperature solutions. The red shading exactly spans the uncertainty of the $\delta^{15}$N-based DCH, demonstrating that the solutions shown in Figure 5 are consistent with the $\delta^{15}$N data. A change in the global search ranges of temperature and accumulation-rate has a minor effect on the width of the red shading, but no impact on the mean values. We note that the equivalent representation of the blue shading from Figure 5 in Figure S9 is identical to that of the red shading.

As noted in the main text, these results show that the Herron-Langway firn model (and all other firn models we examined) cannot simultaneously accommodate all data constraints at all depths. We emphasize that while $\delta^{15}$N tightly constrains the DCH, $\delta^{15}$N does not depend on the details of the depth-density profile, nor on the amount of time represented by the DCH, and therefore cannot constrain either of these variables independently. In contrast, $\Delta$age is a measure of the firn densification time, and water-isotope diffusion length depends on both the densification time and the depth-density structure. Within the firn-model framework, warmer temperatures than our main reconstruction permit agreement with $\delta^{15}$N, but reduce agreement with diffusion-length constraints. We consider our reconstruction conservative with respect to the key result of a relatively warm last glacial maximum. We suggest that water-isotope diffusion-length data, such as we present in this paper, should be used to a greater extent in developing further refinements to firn models in the future (Gkinis et al., 2021).

*S3.4 Sensitivity of Isotope-Temperature Relationship*

In Section 6.2 of the main test, we show that the $\delta^{18}$O-temperature relationship indicated by our reconstruction, based on the HL firn model, is 0.99‰°C$^{-1}$. Table S1 shows results of the same calculation for the sensitivity tests using other firn models (Figure S3), and from the $\delta^{15}$N and $\Delta$age constraints (main text Figure 5). We also report the correlation coefficient $r$ between the $\delta^{18}$O record and each temperature reconstruction. All $\partial(\delta^{18}\mathrm{O})/\partial T$ slopes are significantly greater than the modern surface slope of 0.8‰°C$^{-1}$. While all correlations are significant, the maximum correlation is for the main reconstruction.

**Text S4. Ice-flow modeling**

We use a 2.5-D flowband ice-flow model to estimate a thinning function for SPC14 to compare with the primary thinning function reconstruction described in the main text. As described in the main text, the primary thinning reconstruction contains more high-frequency variation than a 1-D Dansgaard-Johnsen model output. For emphasis, Figure S10 shows this comparison in the depth domain to highlight the main discrepancies in the estimates, particularly from 200 to 500 m depth and from 1400 to 1750 m depth. This ice-flow-model thinning function is constrained by data for ages younger than 10 ka, producing an independent data-based estimate of ice thinning. Beyond 10 ka, we do not have sufficient knowledge of past ice flow direction and the associated bed topography along that flow path in order to fully constrain the model. For the older ice, the goal with the ice-flow-model thinning function is to determine if the structure in the primary thinning function is physically plausible. To this end, our flowband modeling suggests that variations in the primary thinning function can indeed be explained by observed variations in bedrock topography.

### *S4.1 Flowband model*

The flowband model was developed to calculate the time-dependent ice-surface evolution and velocity distribution along a flowline in the ice-sheet interior. The model has been described in Koutnik et al. (2016) where it was applied near the WAIS Divide ice-core site. The model calculates the ice-flow field using the Shallow Ice Approximation, which is appropriate for relatively slow-flowing interior ice that is not beneath an ice divide. Necessary boundary conditions and initial inputs to the model include the accumulation rate (Figure S11A), bed topography (Figure S11C), and ice temperature along the flowline, as well as the ice flux and ice-sheet thickness at one location.

The flow field described by the model is defined within a flowband domain extending 200 km along the flow line. The downstream edge of the domain is located 10 km from the SPC14 site; the upstream edge marks the location of the ice divide, 190 km upstream of the SPC4 site. The width of the flowband domain (Figure S11B) is a tunable parameter and is determined such that the model matches the measured surface velocities and surface elevations described below (Text S4.2). The ice flux and ice-surface elevation are specified at one point in the domain, which we chose to be near to the drill site.

For this work, we calculate a steady-state flow field, rather than consider the transient response to time-varying forcing. A steady-state model is justified for three main reasons. First, the steady-state model provides a good fit to the observed depth-age relationship for the Holocene (Figure S12), where the flowline location and corresponding bed topography are well defined. The steady-state model also compares well with the ice advection estimated by Lilien et al. (2018) (Figure S13), which included a $\sim$15% speed up of surface ice over the last 10 ka. Second, temporal variations in the accumulation rate have little impact on the cumulative thinning as a function of depth (*e.g.,* Nye, 1963). We calculate the thinning as a function of depth and then convert to a function of age based on the SP19 timescale (Winski et al., 2019). Third, while accumulation-rate variations and other changes to the boundary conditions affect ice-particle-path trajectories, these inputs require knowledge of the flowline and bed topography, which are poorly known beyond 65 km upstream from SPC14. Without specification of where the ice flowed, we cannot determine these time-variable inputs, and a time-dependent model has limited value. Additionally, we find that a steady-state model satisfies our goal of evaluating the physical plausibility of the primary thinning function reconstruction.

*S4.2 Model Inputs*

*Velocity, elevation, spatial pattern of accumulation rate, and flowline determination:* Measurements of the surface velocity, surface elevation, and the determination of the flowline from these measurements are described in Lilien et al. (2018), with data available from the United States Antarctic Program Data Center (USAP-DC) at: https://www.usap-dc.org/view/project/p0000200. The surface velocity was measured at a network of stakes with 12.5 km spacing along the lines of longitude every 10° from 110° E to 180° E and out to a distance of 100 km from SPC14. The modern surface velocities were used to determine the modern flowline. The accumulation-rate pattern along the flowline (Figure S11A) was inferred using traced layers imaged with a 200 MHz radar. By comparing the measured layer thickness in SPC14 to the expected layer thickness due to advection of the upstream accumulation-rate pattern, the flowline was confidently determined for a distance of 65 km upstream of SPC14, spanning the past 10.1 ka (Lilien et al., 2018). For ice older than 10 ka, we are uncertain what path the ice took.

*Bedrock topography:* The bed topography along the domain of the flowline (from SPC14 to the ice divide) is a necessary model input, and can be grouped into three sections based on the data available (Figure S11C). 1) From 0 to 65 km upstream of SPC14, we are confident that the ice flowed over the bedrock topography imaged with radar along the modern flowline. 2) For 65 km to 100 km upstream from SPC14, we use the bedrock topography measured along the modern flowline; however, we cannot be sure that ice reaching the SPC14 site flowed along this path. 3) From 100 km to a divide at approximately 190 km upstream, we have no information about the modern flowline, nor do we know the bed topography. However, we can obtain a plausible example of the bed topography from an airborne radar survey in this region.

For the first and second sections, the bedrock topography along 100 km of the modern flowline upstream of SPC14 was imaged with a ground-based, bistatic impulse radar with center frequency of 7 MHz (Figure S14). The radar system has been used widely in Antarctica (Gades et al., 2000; Neumann et al., 2008; Catania et al., 2010). The radar data and bed picks are posted at the USAP-DC at: https://www.usap-dc.org/view/project/p0000200.

For the third section, to provide additional information about the spatial variability in the bed topography beyond 100 km, we use the PolarGAP airborne radar survey (Forsberg et al., 2017). Although PolarGAP data were collected along 135° E and 142.5° E (Figure S14), the data are publicly available as a gridded product. We interpolate the gridded data to extract the bed topography along the two flight lines. The bed topography along our flowline and the two PolarGAP lines are shown in Figure S15. The three profiles track together well until about 70 km upstream of SPC14 where they diverge as the spacing between the lines increases. To obtain a model input for bed topography that produces thinning variations similar to the primary thinning function (recall that our goal is to evaluate whether these variations are physically plausible), we combine information from the two PolarGAP lines. We connect two points (green circles in Figures S15 and S16) that yield a flowline over a high in the bed topography. The orientation of this flowline is nearly perpendicular to the modern flowline, so the ice is unlikely to have flowed over it; however, this example illustrates that the magnitude of topographic variation required to match the structure of the primary thinning function does exist in the region.

*Ice temperature:* An ice-temperature profile is specified using a 1-D thermal model fit to the measurements from the AMANDA and IceCube projects (Price et al., 2002), forced to reach the pressure melting point at the bed. This temperature profile is held constant in time and is scaled linearly as a function of ice thickness along the flowline to estimate the full temperature field in our model domain.

*Basal melt rate:* We test two choices for basal melt rate to gain insight into the sensitivity of the thinning result to this parameter. With all other parameters taken to be the same, one case has no basal melt and one case has 1 cm $a^{-1}$ of basal melt across the whole domain. A 1 cm $a^{-1}$ melt rate is similar to the value inferred by Jordan et al. (2018) farther upstream of SPC14. The difference between the resulting thinning functions increases with depth, but differs by only 17% during the last 10,000 years of the core. For simplicity, we plot only the non-basal melt result in Figure 6 of the main text.

### *S4.3 Tuning the model*

The flux out the downstream edge of the domain was specified to obtain a velocity of 10 m $a^{-1}$ to match modern observations (Lilien et al., 2018). To approximately match the velocities measured at 12.5 km intervals out to a farthest distance of 100 km upstream (Figure S11E), the width of the flowband was increased with distance upstream (Figure S11B). This represents convergent flow, as indicated for this region from the surface topography. The velocity measurements (Lilien et al., 2018) are not precise enough to allow reliable convergence estimates, and we therefore assumed a linear change in flowband width for 100 km upstream. Beyond 100 km upstream, the flowband width continues to increase, at a different rate, such that the divide position is approximately 190 km upstream at an elevation of 3075 m, consistent with a likely ice origin at Titan Dome (Fudge et al., 2020).

### *S4.4 Comparison with measured layers*

The modeled layers are shown in comparison to 7 internal layers imaged by radar (Figure S17). There is a good fit at the core site, which is also reflected in Figure S12, comparing the modeled depth-age profile and the measured data from SP19. The match to the radar layers is not nearly as good upstream where the amplitude of the modeled layers at the bedrock bump is less than what is observed in the measured layers. The discrepancy may be related to the greater uncertainty in the flowband model inputs farther upstream from SPC14.

### *S4.5 Ice-flow-model thinning function*

The ice-flow-model thinning function (Figure 6 in main text) is calculated from the modeled layer thickness at the core site divided by the original thickness (the accumulation rate) when that ice was deposited at the surface. The numerical calculation can become noisy due to the finite model mesh and the difficulty of establishing the accumulation rate at the point of origin given variations in the surface accumulation pattern. Therefore, we smooth the thinning function with a moving average over a depth interval of 50 m. The jaggedness of the thinning function is the most noticeable in the deepest layers where there are smaller depth differences for the same age interval. Because we have used a steady-state model, the modeled age for a given depth is too young for ages prior to the Holocene (since we do not account for the lower accumulation rates of the glacial period). Because the cumulative thinning as a function of depth is insensitive to temporal variations in accumulation (*e.g.,* Nye, 1963), we convert modeled depth to age using the measured depth-age relationship (SP19; Winski et al. (2019)).

The most prominent feature in the thinning function calculated for the Holocene period is at about 7 ka. The $\sim$7 ka layers have thinned less than the layers above, which we term a "reversal" in the thinning function; for example, Parrenin et al. (2004) noted such features for the Vostok ice core. For SPC14, reversals can occur because the strain thinning of layers is affected by changes in ice thickness along the flow line (Figure S18). As the ice flows from a bedrock high into a trough, the thickening of the ice column either reduces the vertical thinning or can even cause vertical thickening. Therefore, ice parcels reaching the $\sim$7 ka layer have thinned less than if the bedrock were flat because the ice column thickened. Ice parcels reaching younger layers, for example the 6 ka layer, have not experienced this thickening. As the ice flows out of this overdeepening, the rise in bed topography causes thinning of the full ice column (*i.e.,* both the 6 ka and 7 ka particles). For the bed topography along the flowline spanning the Holocene time period (from SPC14 to 65 km upstream), this bed overdeepening is the only feature that has a significant impact on the structure of the thinning function.

## Text S5. $\delta^{15}$N-based thinning function

We use a thinning function estimated from measurements of $\delta^{15}$N in SPC14 for an additional comparison with the primary thinning function reconstruction described in the main text (Figure 6 in main text). Following Parrenin et al. (2012), the $\delta^{15}$N-based thinning function uses the diffusive column height as calculated from the $\delta^{15}$N measurements and the $\Delta$depth as calculated from the ice age scale to determine how much thinning has occurred since that ice was at the surface (see main text Section 6.1).

We calculate the DCH with (Parrenin et al., 2012):

$$\mathrm{DCH}(t) = \left(\delta^{15}\mathrm{N}(t) - \Omega(T)\Delta T_{diff}\right)\left(\frac{\Delta mg \times 1000}{RT(t)}\right)^{-1}, \tag{19}$$

where $\Omega(T)$ is the thermal diffusivity, $T_{diff}$ is the temperature difference between the top and bottom of the diffusive column, $\Delta$m is the difference in molar mass between $^{15}$N and $^{14}$N in kg mol$^{-1}$, $g$ is the gravitational acceleration (9.81 m s$^{-2}$), $R$ is the gas constant (8.314 J mol$^{-1}$ K$^{-1}$), and $T(t)$ is the temperature history in K. We use the temperature reconstruction from the optimization in the main text to estimate the temperature history. The temperature difference in the firn is calculated using a 1-D ice-and-heat flow model (Fudge et al., 2019), also forced by the accumulation-rate reconstruction. The temperature dependence of the thermal diffusivity is from Grachev and Severinghaus (2003).

The $\Delta$depth is conceptually similar to the $\Delta$age except that it is the difference in depth in the core, rather than age, of the same climate event in the ice and gas phases. The $\Delta$depth is found for each gas tie point used to develop the SP19 gas timescale (Epifanio et al., 2020). The depth of the ice of the same age is then found from the SP19 ice timescale (Winski et al., 2019).

The $\delta^{15}$N-based thinning function ($\Gamma$) can be described:

$$\Gamma(t) = \frac{\Delta\mathrm{depth}(t)}{\int_0^{\mathrm{LID}(t)} D(z,t)dz} = \frac{\Delta\mathrm{depth}(t)}{\mathrm{LIDIE}(t)} = \frac{\Delta\mathrm{depth}(t)}{A \times \mathrm{LID}(t)}, \tag{20}$$

where

$$\mathrm{LID}(t) = \mathrm{DCH}(t) + \mathrm{CZ} = \mathrm{DCH}(t) + 3. \tag{21}$$

$D(z,t)$ is the density profile of the firn relative to density of ice at a given time, LID($t$) is the lock-in depth, LIDIE($t$) is the lock-in depth in ice equivalent, DCH($t$) is the diffusive column height, and CZ is the thickness of the convective zone, which we set to 3 m (a typical value found in firn air pumping experiments).

Parrenin et al. (2012) showed that the LID/LDIE ratio changes relatively little for different climate conditions at Dome C and thus we can use a constant factor to convert LID to LIDIE. We obtain a value of $A$=0.717 by integrating the SPC14 density profile (Winski et al., 2019) from the surface to a density of 824 kg m$^{-3}$. In the following sections, we discuss the primary sources of uncertainty in the $\delta^{15}$N-based thinning function.

*S5.1 Uncertainties*

We estimate the uncertainties in the calculation of this thinning function by calculating the change in the thinning function with a different input for the seven main parameters below (Figure S19). We choose values which we believe yield approximately 95% confidence (*i.e.,* 2 standard deviation).

*Density and depth of firn column:* Converting the LID to LIDIE has two primary uncertainties: uncertainty in the measured modern density profile and how much variation there is through time. We estimate the first using six firn cores, two at SPC14 and two near South Pole, as well as two at 50 km upstream (Lilien et al., 2018). We assume lock-in density at 824 kg m$^{-3}$ with an uncertainty $\pm$5 kg m$^{-3}$. The conversion factor, $A$, to get LIDIE from LID is equivalent to the average density of the firn column relative to the density of ice, and hence is unitless. To estimate the uncertainty of this conversion factor $A$, we find a maximum difference of 0.015 among the six firn cores relative to measured value for SPC14.

For the time-varying uncertainty in the conversion factor $A$, we use the pairs of temperature and accumulation rate for each time step found in the primary reconstruction to force a Herron-Langway densification model. We also allow the surface density to vary by $\pm$30 kg m$^{-3}$ from the SPC14 surface density value. We find the largest difference from the modern SPC14 value to define an uncertainty of 0.023 (2 standard deviation).

*Convective zone impact on diffusive column height:* The modern convective zone is 3 m and we assume the uncertainty is $\pm$3 m.

*Vertical thinning of firn column due to ice flow:* Separate from firn compaction, there is vertical thinning caused by the lateral stretching due to ice flow and the effectively incompressible nature of ice under these conditions. Measurements of englacial vertical velocities have become possible with phase sensitive radars; however, separating the vertical thinning due to ice flow from the vertical compaction of the firn is not yet possible. Therefore, we approximate this vertical thinning assuming a uniform, ice-equivalent vertical strain rate (*e.g.,* Nye, 1963). We develop the uncertainty by assuming either no vertical thinning or double our default vertical thinning.

$\Delta$*depth:* We estimate the uncertainty of the $\Delta$depth from the $\Delta$age uncertainties developed for the SP19 gas timescale (Epifanio et al., 2020). To find the uncertainty, we take the difference in depths that correspond to the maximum and minimum gas ages and divide it in half.

*Measurement uncertainty and variability:* The DCH is calculated from the $\delta^{15}N$ of $N_2$ data using Equation 19. The uncertainty in determining the DCH depends on three things: 1) the measurement uncertainty of the $\delta^{15}N$; 2) variability in how well the measurement represents the actual DCH; and 3) the uncertainty in interpolation from the closest measurement. The $\delta^{15}N$ has been measured at 50- to 100-year resolution for much of the core, such that the interpolation distances are small. To jointly assess these measurement uncertainty and variability, we compared the DCH estimates of the three closest measurements. On average, the three measurements differed by slightly less than 2 m. The differences among the three measurements did not have a temporal trend, so we calculate the uncertainty with a constant 2 m uncertainty. This is the smallest uncertainty for most of the measurements.

*Thermal fractionation:* The thermal fractionation of $\delta^{15}$N is calculated using a 1-D ice-and-heat flow model (Fudge et al., 2019). The firn-density profile is assumed constant through time, with the temperature and accumulation-rate histories from the main reconstruction presented here as the primary forcings. The thermal conductivity in the firn follows the Van Dusen formula (Cuffey and Paterson, 2010). The temperature difference is calculated from top and bottom of the diffusive column. The isothermal diffusive column height is used initially in the temperature difference calculation; a new diffusive column height is computed including thermal fractionation and the temperature difference is then recalculated. One iteration is sufficient to reach a stable diffusive column height. The amount of thermal fractionation increases in the glacial compared to the Holocene. This is driven by the lower glacial accumulation rates, which decrease the vertical advection in the firn column. Because the base of the firn column is warmer than the surface, warming will tend to mute the temperature gradient in the firn, while cooling will enhance the temperature gradient. Thus, the average temperature only weakly impacts the thermal fractionation, but the trend in the temperature history is important.

Developing an uncertainty for the trend in the temperature history is not straightforward because it requires making assumptions about the magnitude of timing of temperature change on multi-centennial to millennial timescales. The difference between the main reconstruction and the scaled water isotopes (Figure 8 in the main text) illustrates the uncertainty in these higher frequency trends. Therefore, we seek a simple approximation to capture the main features of the uncertainty to allow comparison with the other sources of uncertainty in determining the thinning function. We assume an uncertainty in the glacial period of 3 m, which is half the maximum impact of including thermal fractionation. To reflect the lower uncertainty due to increasing accumulation rates during the transition into the Holocene, we linearly decrease the uncertainty to 1.5 m from 20 ka to 12 ka, where it is then constant through the present.

*S5.2 Total uncertainty on thinning function*

To calculate the total uncertainty on the $\delta^{15}$N-based thinning function, we combine the uncertainty calculated for each of the seven terms above. The uncertainties for each term are shown in Figure S19. We combine the six sources of uncertainty in quadrature to find the total uncertainty. For glacial-aged ice, the dominant uncertainty is that for $\Delta$depth. This is driven by the larger uncertainty in $\Delta$age primarily due to the larger $\Delta$age at WAIS Divide during the glacial. During the Holocene, all of the terms are more similar in magnitude, but the uncertainty due to temporal variations in the density profile is the largest. Our use of a uniform value (.023) for temporal density for the full record is likely too simplistic, and perhaps too conservative, since the uncertainty is based on glacial values which differ from modern value far more than the Holocene values.

## References

Barkan, E & Luz, B. (2007). Diffusivity fractionations of $H_2^{16}O/H_2^{17}O$ and $H_2^{16}O/H_2^{18}O$ in air and their implications for isotope hydrology. *Rapid Communications in Mass Spectrometry*, 21(18), 2999–3005. https://doi.org/10.1002/rcm.3180

Catania, G, C. Hulbe, & H. Conway, 2010. Grounding-line basal melt rates determined using radar-derived internal stratigraphy, *J. Glaciol.* 56(197), 545–554 https://doi.org/10.3189/002214310792447842

Cuffey, K. M., & Paterson, W. S. B. (2010). The physics of glaciers. Academic Press.

Dahl-Jensen, D., Mosegaard, K., Gundestrup, N., Clow, G. D., Johnsen, S. J., Hansen, A. W., & Balling, N. (1998). Past temperatures directly from the Greenland ice sheet. *Science*, 282(5387), 268–271. https://doi.org/10.1126/science.282.5387.268

Dansgaard, W., & Johnsen, S. J. (1969). A flow model and a time scale for the ice core from Camp Century, Greenland. *Journal of Glaciology*, 8(53), 215–223. https://doi.org/10.3189/S0022143000031208

Epifanio, J. A., Brook, E. J., Buizert, C., Edwards, J. S., Sowers, T. A., Kahle, E. C., Severinghaus, J. P., Steig, E. J., Winski, D. A., Osterberg, E. C., Fudge, T. J., Aydin, M., Hood, E., Kalk, M., Kreutz, K. J., Ferris, D. G., & Kennedy, J. A. (2020). The SP19 chronology for the South Pole Ice Core–Part 2: gas chronology, Δage, and smoothing of atmospheric records. *Climate of the Past*, 16(6), 2431–2444. https://doi.org/10.5194/cp-16-2431-2020

Forsberg, R., A.V. Olesen, F. Ferraccioli, T. Jordan, H, Corr, & K. Matsuoka (2017). PolarGap 2015/16: Filling the GOCE polar gap in Antarctica and ASIRAS flight around South Pole. Radar grids available at:

$ftp://ftp.bas.ac.uk/tomj/PolarGAP/PolarGAP\_radar\_grids.zip$

Fudge, T. J., Biyani, S. C., Clemens-Sewall, D., & Hawley, R. L. (2019). Constraining geothermal flux at coastal domes of the Ross Ice Sheet, Antarctica. *Geophysical Research Letters*, 46(22), 13090–13098. https://doi.org/10.1029/2019GL084332

Fudge, T. J., Lilien, D. A., Koutnik, M., Conway, H., Stevens, C. M., Waddington, E. D., Steig, E. J., Schauer, A. J., & Holschuh, N. (2020). Advection and non-climate impacts on the South Pole Ice Core. *Clim. Past*, 16, 819–832. https://doi.org/10.5194/cp-16-819-2020

Gades, A. M., Raymond, C. F., Conway, H., & Jacobel, R. W. (2000). Bed properties of Siple Dome and adjacent ice streams West Antarctica, inferred from radio-echo sounding measurements. *Journal of Glaciology*, 46(152), 88–94. https://doi.org/10.3189/172756500781833467

Gelman, A., Roberts, G. & Gilks W. (1996). Efficient Metropolis jumping rules, in Bayesian Statistics 5, Berger, J. O., Bernardo, J. M., Dawid, A. P. and Smith, A. F. M. (eds), Oxford University Press.

Gkinis, V., Simonsen, S. B., Buchardt, S. L., White, J. W. C., & Vinther, B. M. (2014). Water isotope diffusion rates from the NorthGRIP ice core for the last 16,000 years - glaciological and paleoclimatic implications. *Earth and Planetary Science Letters*, 405, 132–141. https://doi.org/10.1016/j.epsl.2014.08.022

Gkinis, V., Holme, C., Kahle, E.C., Stevens, C.M., Steig, E.J., & Vinther, B.M. (2021). Numerical experiments on firn isotope diffusion with the Community Firn Model. *Journal of Glaciology*, 1–23. doi:10.1017/jog.2021.1

Goujon, C., Barnola, J. M., & Ritz, C. (2003). Modeling the densification of polar firn including heat diffusion: Application to close-off characteristics and gas isotopic fractionation for Antarctica and Greenland sites. *Journal of Geophysical Research: Atmospheres*, 108(D24). https://doi.org/10.1029/2002JD003319

Grachev, A. M., & Severinghaus, J. P. (2003). Laboratory determination of thermal diffusion constants for 29N2/28N2 in air at temperatures from 60 to 0 C for reconstruction of magnitudes of abrupt climate changes using the ice core fossil–air paleothermometer. *Geochimica et Cosmochimica Acta*, 67(3), 345–360. https://doi.org/10.1016/S0016-7037(02)01115-8

Herron, M. M., & Langway, C. C. (1980). Firn densification: an empirical model. *Journal of Glaciology*, 25(93), 373–385. https://doi.org/10.3189/S0022143000015239

Johnsen, S. J., Clausen, H. B., Cuffey, K. M., Hoffmann, G., Schwander, J., & Creyts, T. (2000). Diffusion of stable isotopes in polar firn and ice: The isotope effect in firn diffusion. T. Hondoh (Ed.), *Physics of Ice Core Records*, Hokkaido University Press, Sapporo (2000), pp. 121–140.

Jones, T. R., White, J. W. C., Steig, E. J., Vaughn, B. H., Morris, V., Gkinis, V., Markle, B. R., & Schoenemann, S. W. (2017b). Improved methodologies for continuous flow analysis of stable water isotopes in ice cores. Atmospheric Measurement Techniques, 10, 617–632. https://doi.org/10.5194/amt-10-617-2017

Jordan, T. A., Martin, C., Ferraccioli, F., Matsuoka, K., Corr, H., Forsberg, R., Olesen, A., & Siegert, M. (2018). Anomalously high geothermal flux near the South Pole. *Scientific reports*, 8(1), 1–8. https://doi.org/10.1038/s41598-018-35182-0

Kahle, E. C. (2020). Climate reconstructions from ice cores: New techniques to understand the information preserved in the South Pole ice core (Doctoral dissertation, University of Washington, Seattle, USA). http://hdl.handle.net/1773/45398

Khan, A., Mosegaard, K., & Rasmussen, K. L. (2000). A new seismic velocity model for the Moon from a Monte Carlo inversion of the Apollo lunar seismic data. *Geophysical Research Letters*, 27(11), 1591–1594. https://doi.org/10.1029/1999GL008452

Koutnik, M. R., Fudge, T. J., Conway, H., Waddington, E. D., Neumann, T. A., Cuffey, K. M., Taylor, K. C., et al. (2016). Holocene accumulation and ice flow near the West Antarctic Ice Sheet Divide ice core site. *Journal of Geophysical Research: Earth Surface*, 121(5), 907–924. https://doi.org/10.1002/2015JF003668

Lamb, K. D., Clouser, B. W., Bolot, M., Sarkozy, L., Ebert, V., Saathoff, H., Mohler, O., & Moyer, E. J. (2017). Laboratory measurements of HDO/H2O isotopic fractionation during ice deposition in simulated cirrus clouds. *Proceedings of the National Academy of Sciences*, 114(22), 5612–5617. https://doi.org/10.1073/pnas.1618374114

Li, J. & Zwally, H. J. (2015). Response times of ice-sheet surface heights to changes in the rate of Antarctic firn compaction caused by accumulation and temperature variations. *Journal of Glaciology*, 61(230), 1037–1047. https://doi.org/10.3189/2015JoG14J182

Ligtenberg, S. R. M., Helsen, M. M., & Van den Broeke, M. R. (2011). An improved semi-empirical model for the densification of Antarctic firn. *The Cryosphere*, 5, 809–819. https://doi.org/10.5194/tc-5-809-2011

Lilien, D. A., Fudge, T. J., Koutnik, M. R., Conway, H., Osterberg, E. C., Ferris, D. G., & Stevens, C. M. et al. (2018). Holocene Ice-Flow Speedup in the Vicinity of the South Pole. *Geophysical Research Letters*, 45(13), 6557–6565.

https://doi.org/10.1029/2018GL078253

Looyenga, H. (1965). Dielectric constants of heterogeneous mixtures. *Physica*, 31(3), 401–406. https://doi.org/10.1016/0031-8914(65)90045-5

Luz, B. & Barkan, E. (2010). Variations of 17O/16O and 18O/16O in meteoric waters. *Geochimica et Cosmochimica Acta*, 74(22), 6276–6286. https://doi.org/10.1016/j.gca.2010.08.016

Majoube, B. (1970). Fractionation factor of $^{18}$O between water vapour and ice. *Nature* 226, 1242. https://doi.org/10.1038/2261242a0

Metropolis, N., Rosenbluth, A. W., Rosenbluth, M. N., Teller, A. H., & Teller, E. (1953). Equation of state calculations by fast computing machines. *The Journal of Chemical Physics*, 21(6), 1087–1092. https://doi.org/10.1063/1.1699114

Mosegaard, K. & Tarantola, A. (1995). Monte Carlo sampling of solutions to inverse problems. *Journal of Geophysical Research: Solid Earth*, 100(B7), 12431–12447. https://doi.org/10.1029/94JB03097

Mosegaard, K. (1998). Resolution analysis of general inverse problems through inverse Monte Carlo sampling. *Inverse Problems*, 14(3), 405. https://doi.org/10.1088/0266-5611/14/3/004

Mosegaard, K., & Tarantola, A. (2002). Probabilistic approach to inverse problems. In W. Lee, P. Jennings, C. Kisslinger, & H. Kanamori (Eds.), *International Handbook of Earthquake & Engineering Seismology (Part A)* (237–265). Academic Press.

Mosegaard, K. & Sambridge, M. (2002). Monte Carlo analysis of inverse problems. *Inverse problems*, 18(3), R29. https://doi.org/10.1088/0266-5611/18/3/201

Neumann, T. A., Conway, H., Price, S., Waddington, E. D., & Morse, D. L. (2008). Holocene accumulation and ice-sheet dynamics in central West Antarctica. *Journal of Geophysical Research*, 113(F2). https://doi.org/10.1029/2007JF000764

Nye, J. 1963. Correction factor for accumulation measured by the thickness of the annual layers in an ice sheet. *Journal of Glaciology*, 4(36), 785–788. https://doi.org/10.3189/S0022143000028367

Parrenin, F., Remy, F., Ritz, C., Siegert, M. J., & Jouzel, J. (2004). New modeling of the Vostok ice flow line and implication of the glaciological chronology of the Vostok ice core. *Journal of Geophysical Research*, 109, (D20). https://doi.org/10.1029/2004JD004561

Parrenin, F., Barker, S., Blunier, T., Chappellaz, J., Jouzel, J., Landais, A., Veres, D. et al. (2012). On the gas-ice depth difference (Δdepth) along the EPICA Dome C ice core. *Climate of the Past*, 8(2), 1089–1131. https://doi.org/10.5194/cpd-8-1089-2012

Price, P. B., Nagornov, O. V., Bay, R., Chirkin, D., He, Y., Miocinovic, P., Richards, A., Woschnagg, K., Koci, B., & Zagorodnov, V. (2002). Temperature Profile for Glacial Ice at the South Pole: Implications for Life in a Nearby Subglacial Lake. *Proceedings of the National Academy of Sciences*, 99(12), 7844–7847. https://doi.org/10.1073/pnas.082238999

Raymond, C. (1983). Deformation in the vicinity of ice divides. *Journal of Glaciology*, 29(103), 357–373. https://doi.org/10.3189/S0022143000030288

Schwander, J., Stauffer, B., & Sigg, A. (1988). Air mixing in firn and the age of the air at pore close-off. *Annals of Glaciology*, 10, 141–145. https://doi.org/10.3189/S0260305500004328

Simonsen, S. B., Stenseng, L., Adalgeirsdottir, G., Fausto, R. S., Hvidberg, C. S., & Lucas-Picher, P. (2013). Assessing a multilayered dynamic firn-compaction model for Greenland with ASIRAS radar measurements. *Journal of Glaciology*, 59 (215), 545–558. https://doi.org/10.3189/2013JoG12J158

Steen-Larsen, H. C., Waddington, E. D., & Koutnik, M. R. (2010). Formulating an inverse problem to infer the accumulation-rate pattern from deep internal layering in an ice sheet using a Monte Carlo approach. *Journal of Glaciology*, 56(196), 318–332. https://doi.org/10.3189/002214310791968476

Stevens, C. M., Verjans, V., Lundin, J., Kahle, E. C., Horlings, A. N., Horlings, B. I., & Waddington, E. D. (2020). The Community Firn Model (CFM) v1. 0. *Geoscientific Model Development*, 13(9), 4355–4377. https://doi.org/10.5194/gmd-13-4355-2020

Tarantola, A. (1987). Inverse problem theory: Methods for data fitting and model parameter estimation. *Elsevier Science*, Amsterdam.

Winski, D. A., Fudge, T. J., Ferris, D. G., Osterberg, E. C., Fegyveresi, J. M., Cole-Dai, J., Buizert, C. et al. (2019). The SP19 chronology for the South Pole Ice Core–Part 1: volcanic matching and annual layer counting. *Climate of the Past*, 15(5), 1793–1808. https://doi.org/10.5194/cp-15-1793-2019

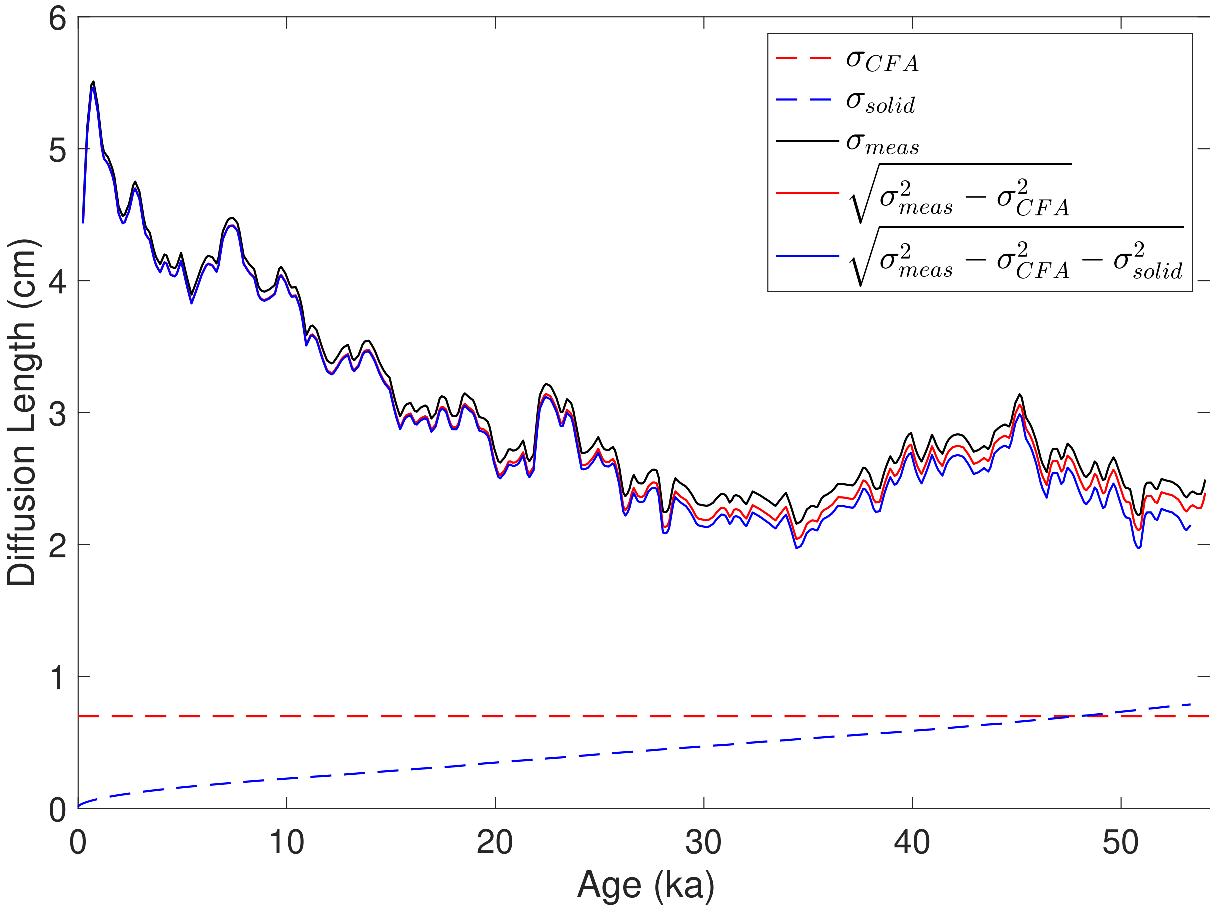


Figure S1: Impact of corrections applied to diffusion-length measurements. Dashed curves show the effective diffusion length resulting from the continuous-flow system (CFA, red), and from diffusion in solid ice (blue). Solid curves show diffusion lengths obtained from the water-isotope data before (black) and after correction for the CFA (red) and solid-ice diffusion (blue).

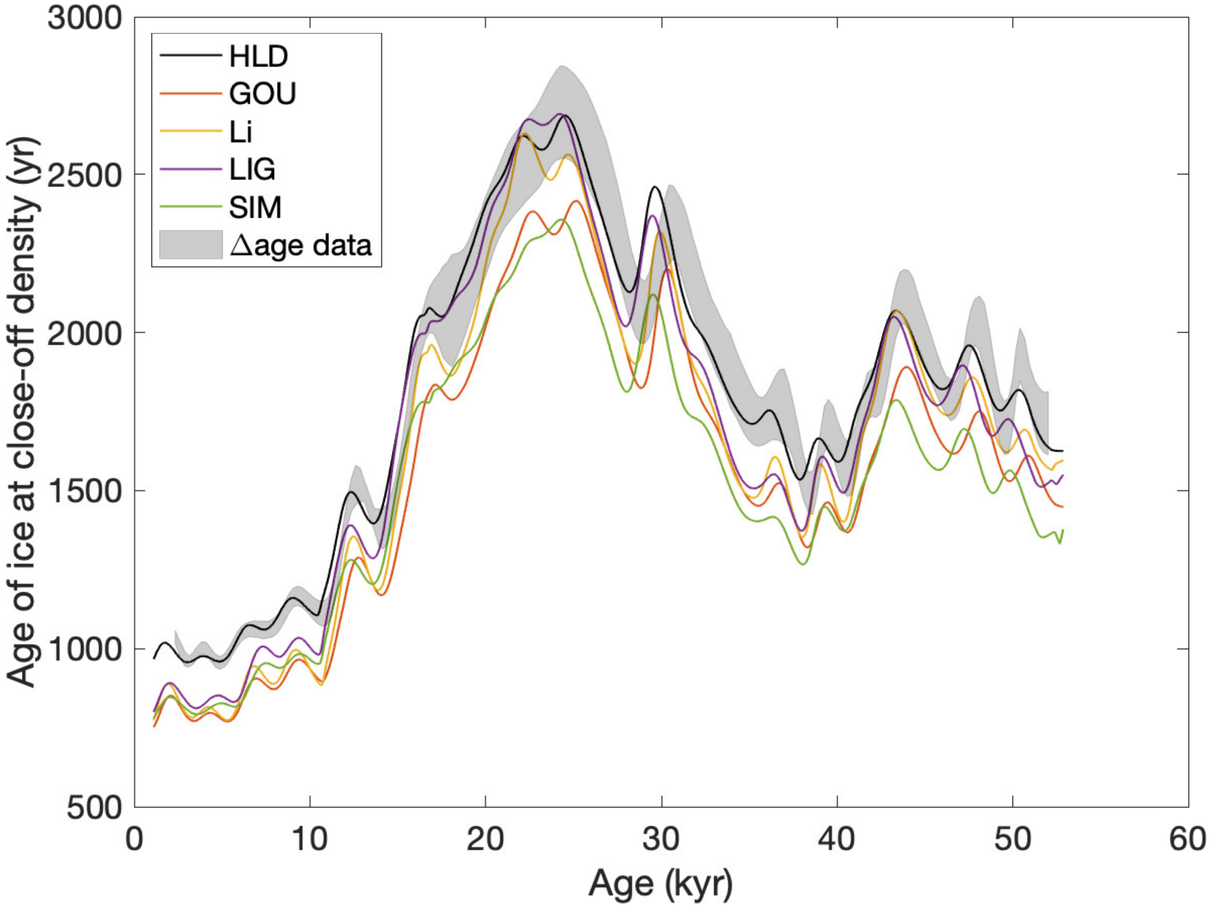


Figure S2: Close-off age as a function of age for a collection of models from the Community Firn Model framework (HLD = Herron and Langway (1980), GOU = Goujon et al. (2003), Li = Li and Zwally (2015), LIG = Ligtenberg et al. (2011), SIM = Simonsen et al. (2013)). The grey shading shows the Δage data and two s.d. uncertainty.

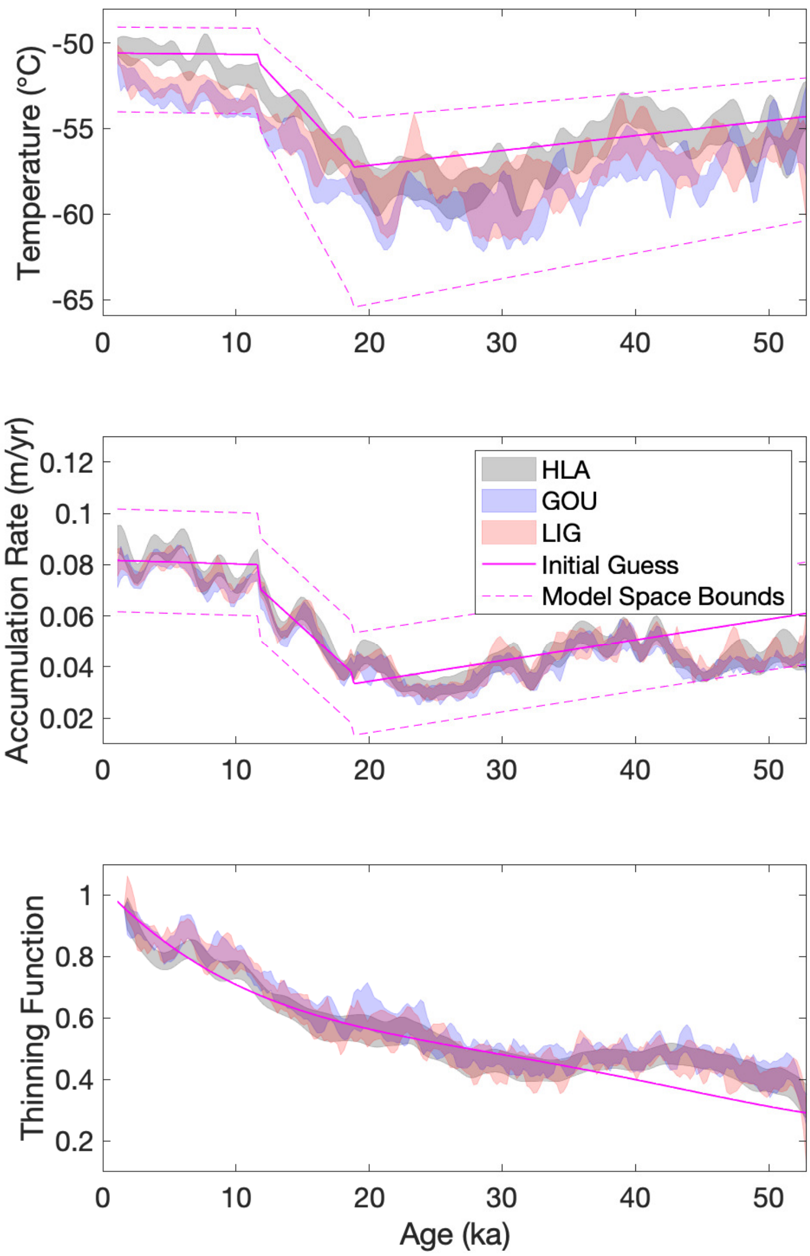


Figure S3: Results of inverse procedure using three different firn models. Grey, blue, and red shading show two s.d. results for Herron and Langway (1980) (HLA), Goujon et al. (2003) (GOU), and Ligtenberg et al. (2011) (LIG), respectively.

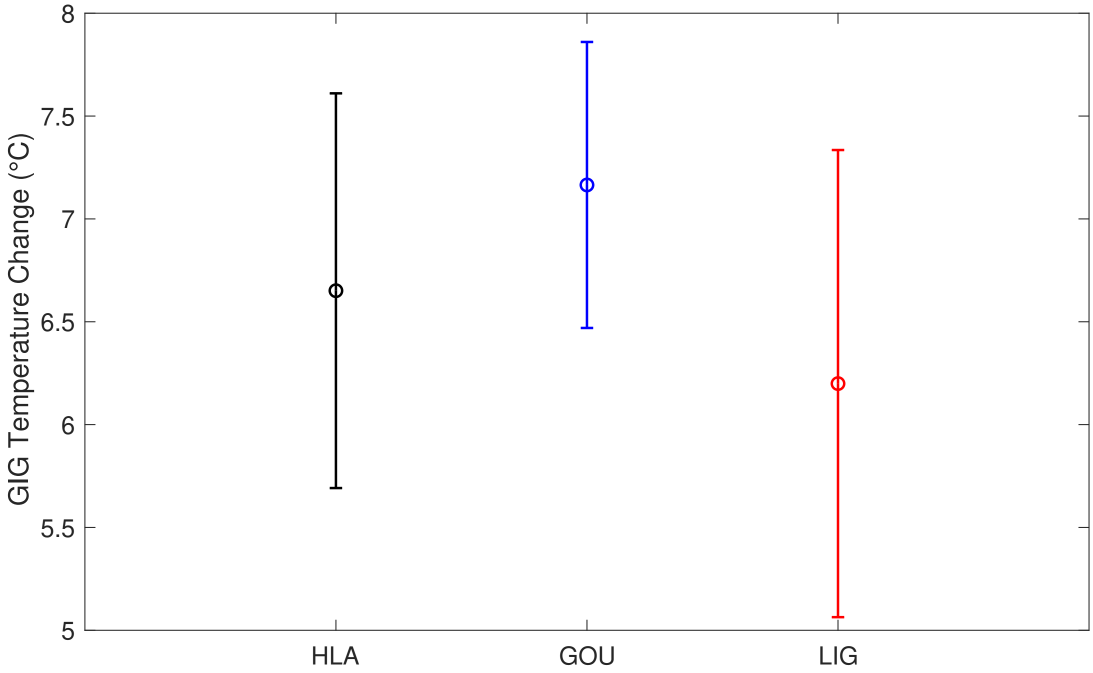


Figure S4: Glacial-interglacial temperature change from the inverse framework with three different firn models. Mean and one s.d. are shown for Herron and Langway (1980) (HLA), Goujon et al. (2003) (GOU), and Ligtenberg et al. (2011) (LIG). The temperature difference is calculated on the intervals defined in the main text: present = 500-2500 years; glacial = 19500-22500 years. The temperature reconstructions have been corrected for ice advection from upstream, resulting in a temperature change estimate for the South Pole site.

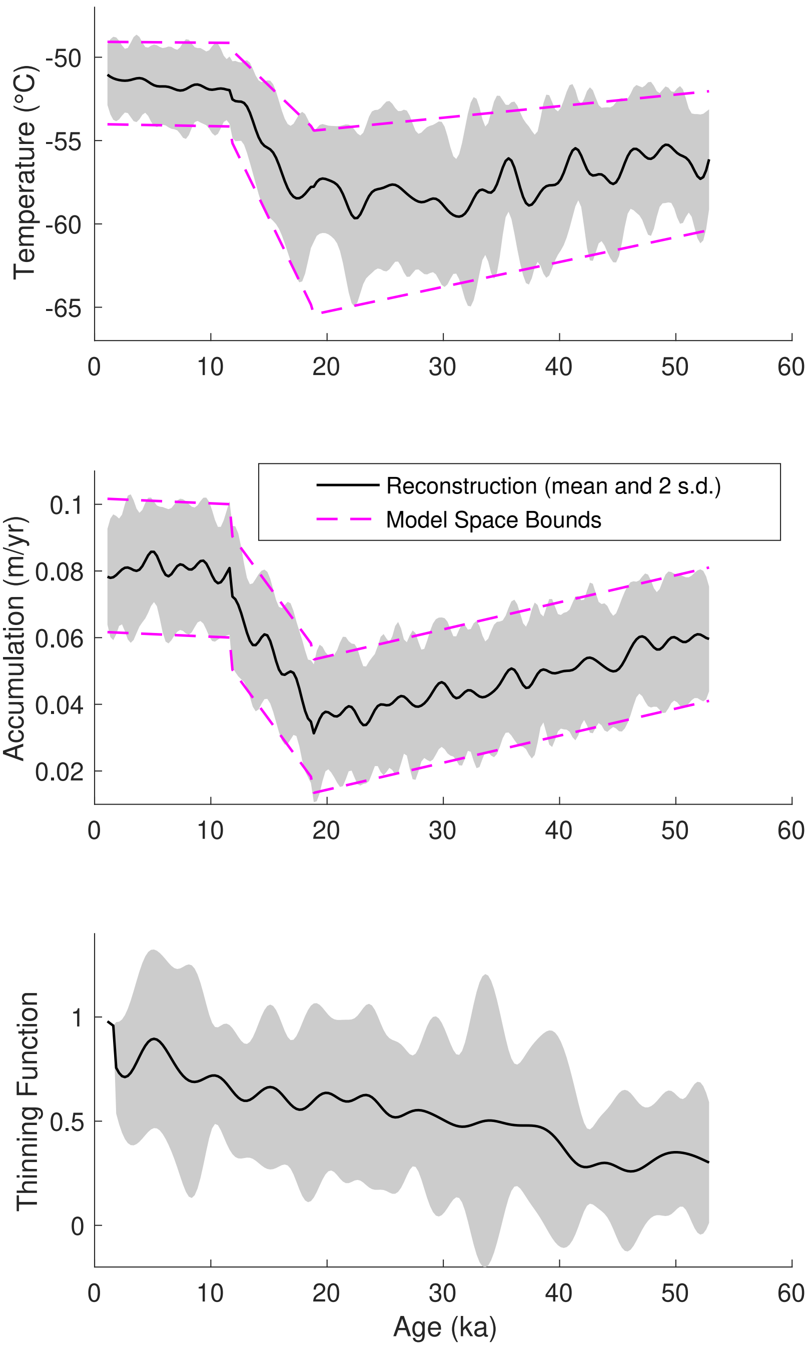


Figure S5: Results of the null test to recover the *a priori* distribution. In the upper two panels, for which model bounds are defined, two standard deviations of the *a posteriori* distribution (grey shading) approximately fill the bounded space (dashed magenta lines), and the mean of the distribution (black curve) is approximately the mean of the bounds.

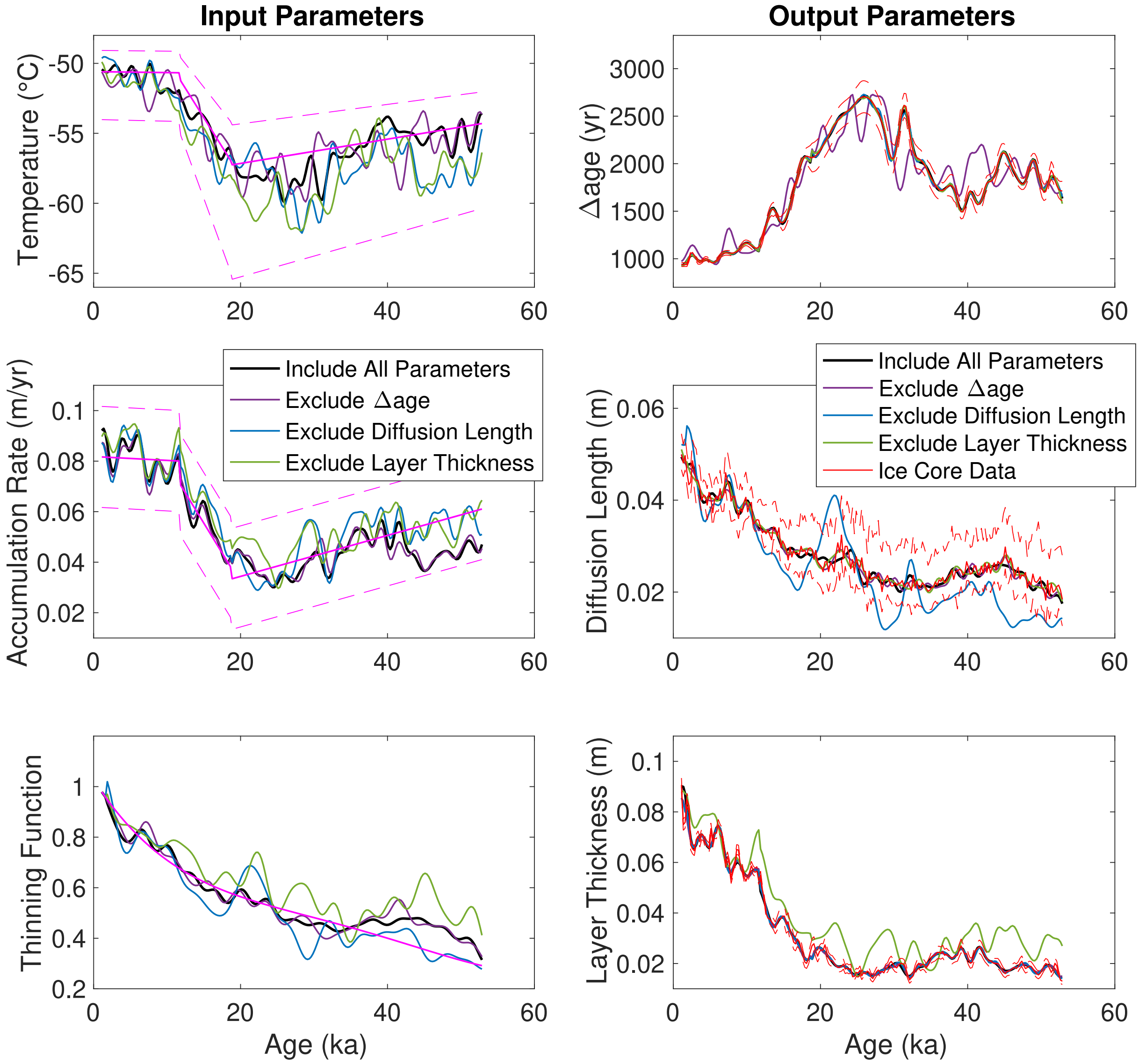


Figure S6: Analysis of the sensitivity of the *a posteriori* distribution to information in each data set. Each color shows the *a posteriori* distribution mean for a different sensitivity test. We compare the results when Δage is excluded (purple), when diffusion length is excluded (blue), when layer thickness is excluded (green), and when all data sets are included (black). Magenta curves in the left panels show *a priori* information and red curves in the right panels show ice-core data and uncertainties.

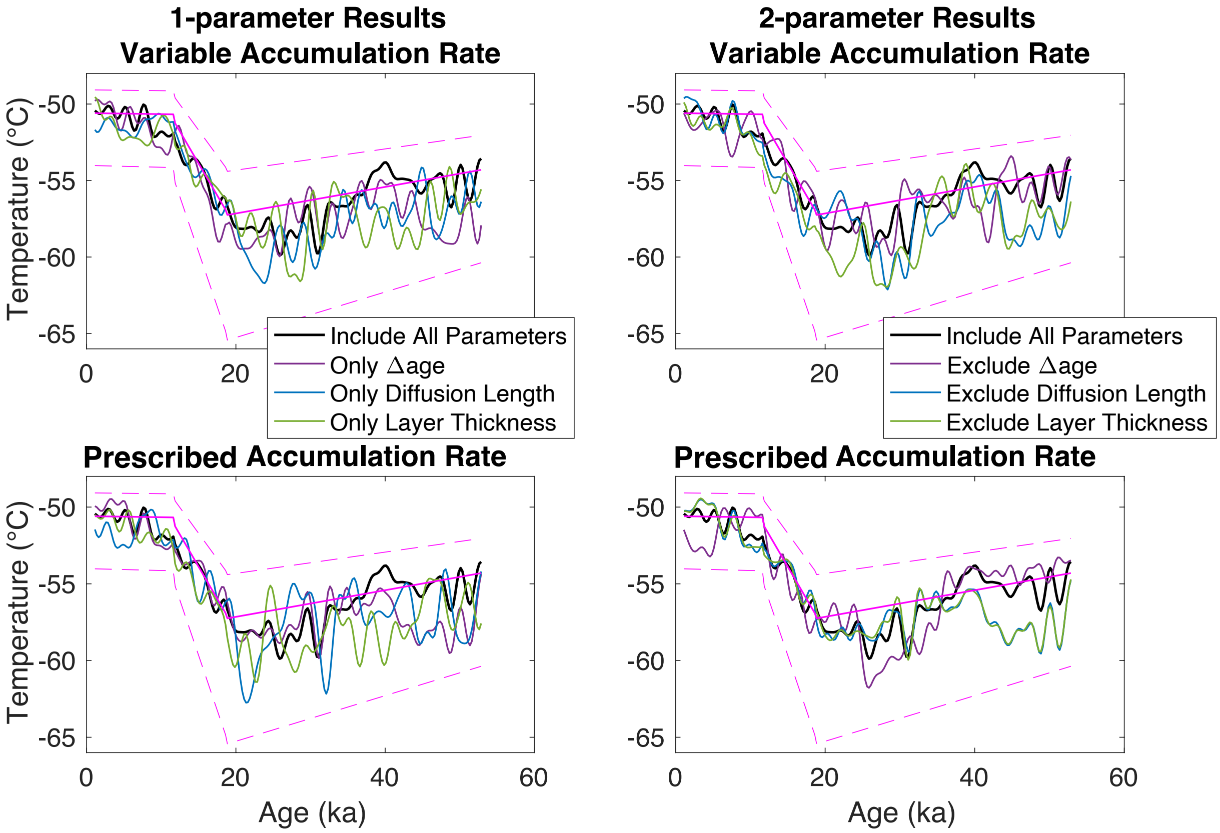


Figure S7: Analysis of the sensitivity of temperature to information in each data set. Colors are defined as in Figure S6. The results of the 1-parameter suite are shown on the left and of the 2-parameter suite on the right. The upper row shows the result when accumulation rate is allowed to vary, and the lower row shows the result when accumulation rate is held at the prescribed values.

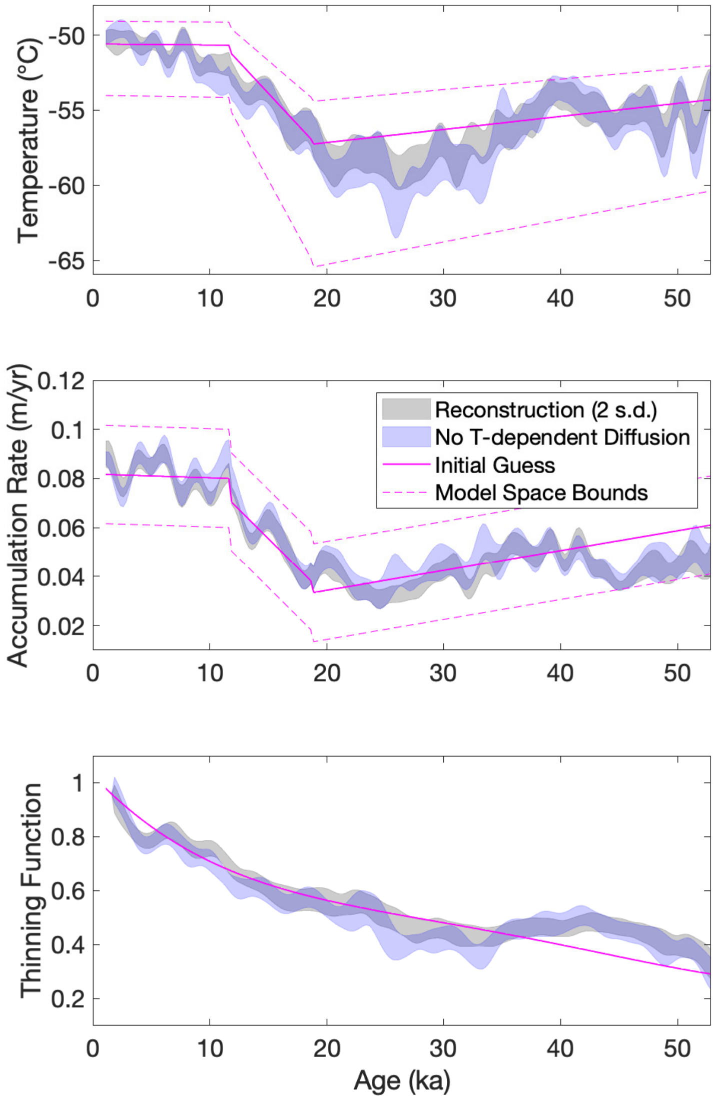


Figure S8: Analysis of sensitivity to the temperature dependence within the water-isotope diffusion model. Grey shading shows the main inverse result as a control test. Blue shading shows the results from holding the temperature history constant within the water-isotope diffusion model, only allowing the diffusion-length data to impact the thinning function.

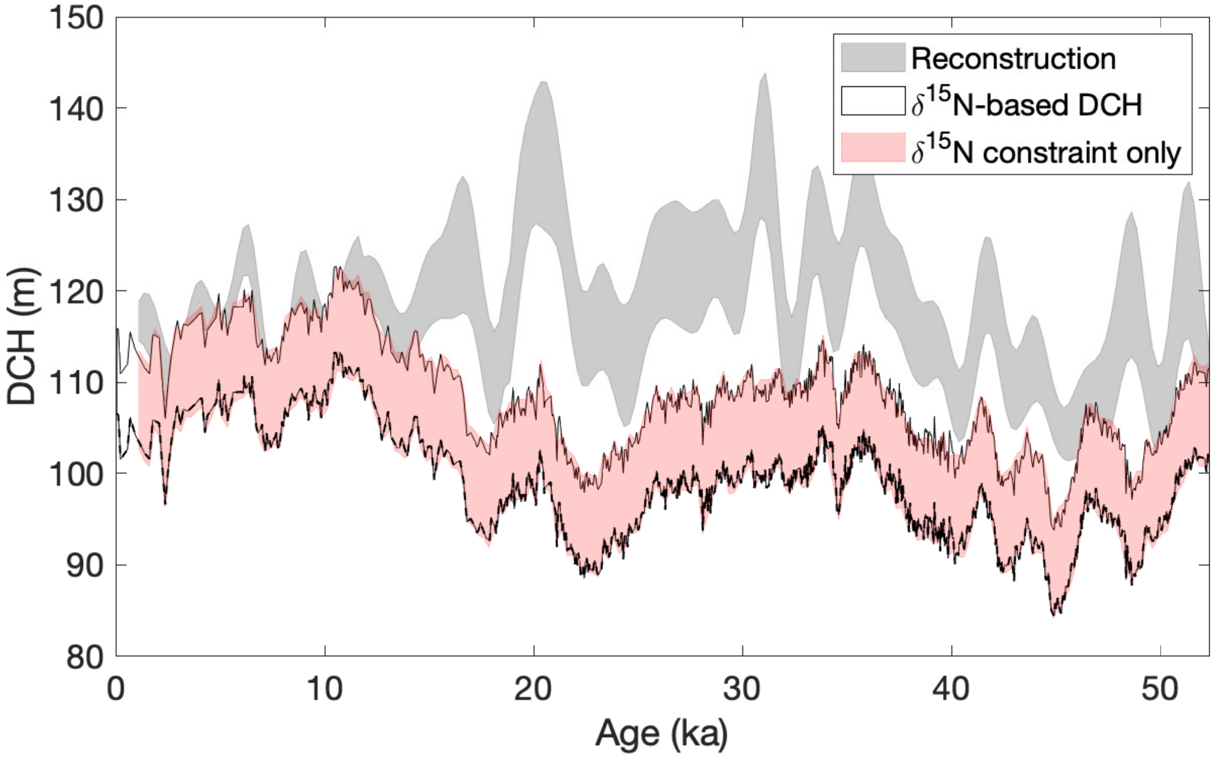


Figure S9: Comparison of diffusive column height (DCH), shown as two s.d. for each source. Grey shading shows the DCH as modeled by the temperature and accumulation rate solutions accepted in the main reconstruction. The black outline shows the DCH as calculated from the $\delta^{15}$N data. Red shading shows the $\delta^{15}$N-constrained DCH, reconstructed from the temperature and accumulation-rate histories shown in Figure 5 in the main text.

Table S1: Sensitivity of the relationship between water isotopes and temperature. Calibrated slopes are given for the relationship between water isotopes and temperature from five different temperature reconstructions: the main inverse result, the results from using the GOU and LIG firn models instead of HLA, and the results from using the constraints of the $\delta^{15}$N and $\Delta$age data sets. The correlation coefficient $r$ is given for the relationship between the water-isotope record and each temperature reconstruction.

| **Reconstruction** | **Slope (‰°C$^{-1}$)** | $r$ |
|---|---|---|
| Main | 0.99 | 0.94 |
| GOU | 0.97 | 0.94 |
| LIG | 1.10 | 0.90 |
| $\delta^{15}$N | 1.28 | 0.84 |
| $\delta^{15}$N & $\Delta$age | 1.14 | 0.86 |

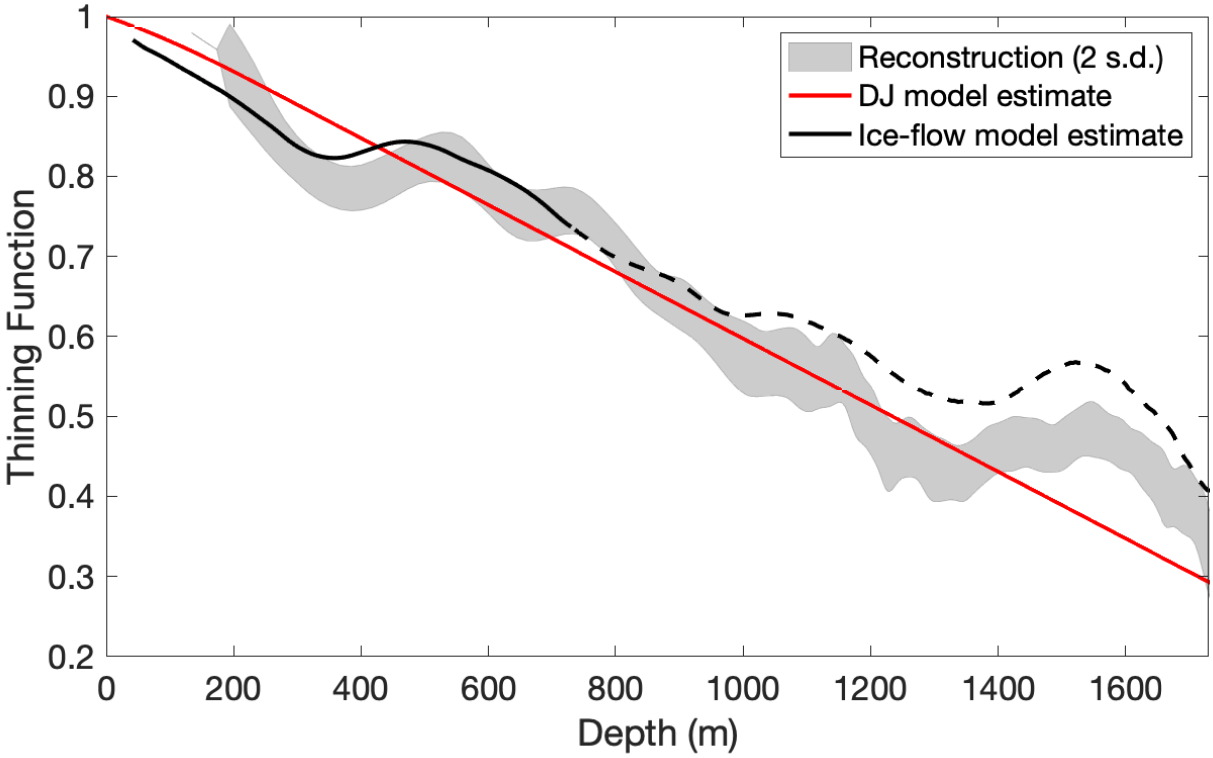


Figure S10: Comparison of primary thinning reconstruction (grey band shows two s.d. uncertainty), the 1-D Dansgaard-Johnsen model output (red) plotted against depth, and the thinning estimate from the 2.5-D ice flow model (black). As in Figure 6 in the main text, the dashed black line shows the depths at which the upstream bed topography is unknown. The reconstruction shows considerably more high-frequency variability. Note that the reconstruction band collapses to a line at the upper depth points due to an imposed constraint of *a priori* information to limit variability in the uppermost part of the thinning function.

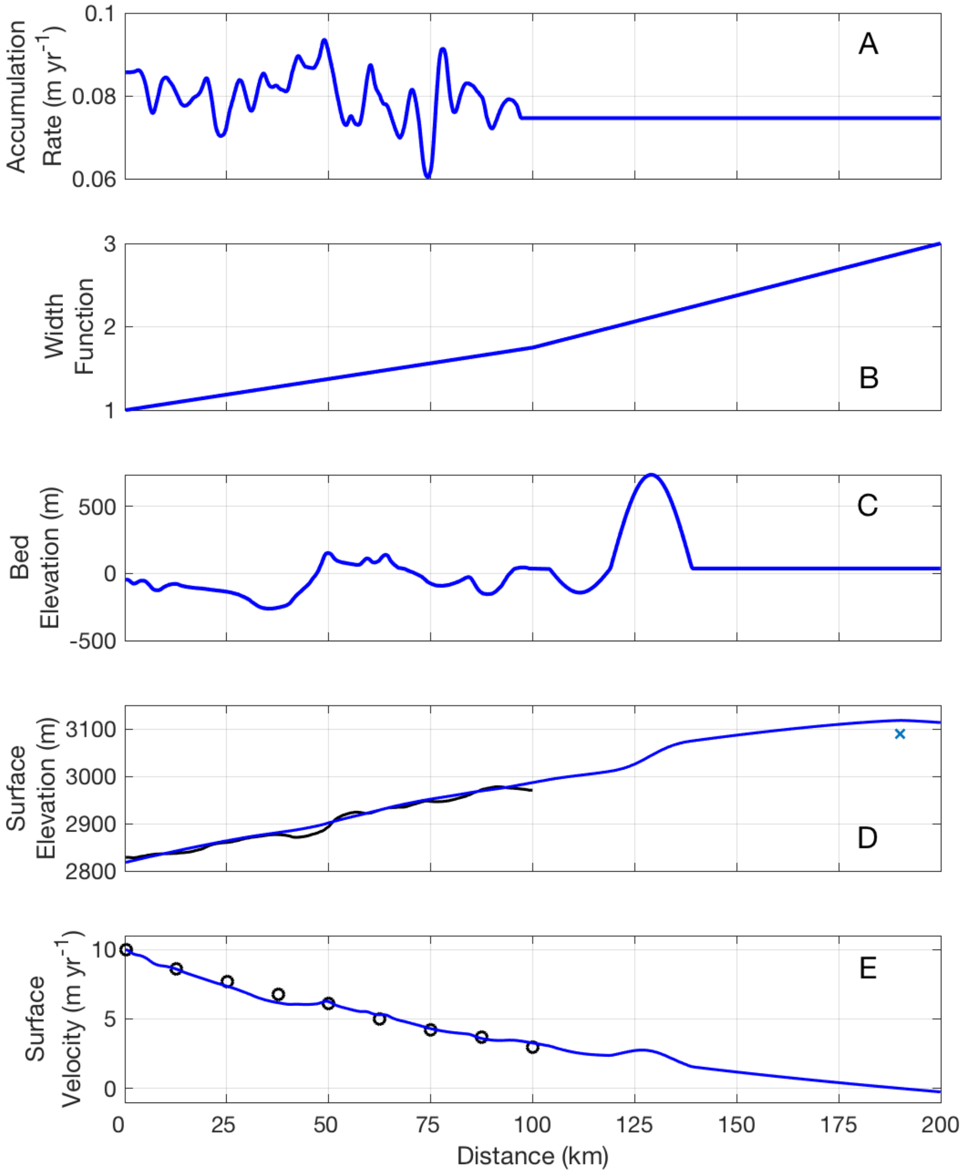


Figure S11: Flowband model inputs (A-C) and model fits to measured data (D-E). A) Modern accumulation-rate pattern for 100 km upstream of SPC14 site inferred from the available shallow radar measurements (Lilien et al., 2018; Fudge et al., 2020). B) Normalized width function used to fit measured surface velocities in panel E. C) Bed topography was measured from 0 to 100 km. Beyond 100 km, the bed topography used in the model is determined as discussed in Text S4.2. D) Measured (black) and modeled surface elevation (blue). The small black "x" at 190 km marks the approximate position and elevation of Titan Dome relative to SPC14. E) Measured (black circles) and modeled surface velocities (blue).

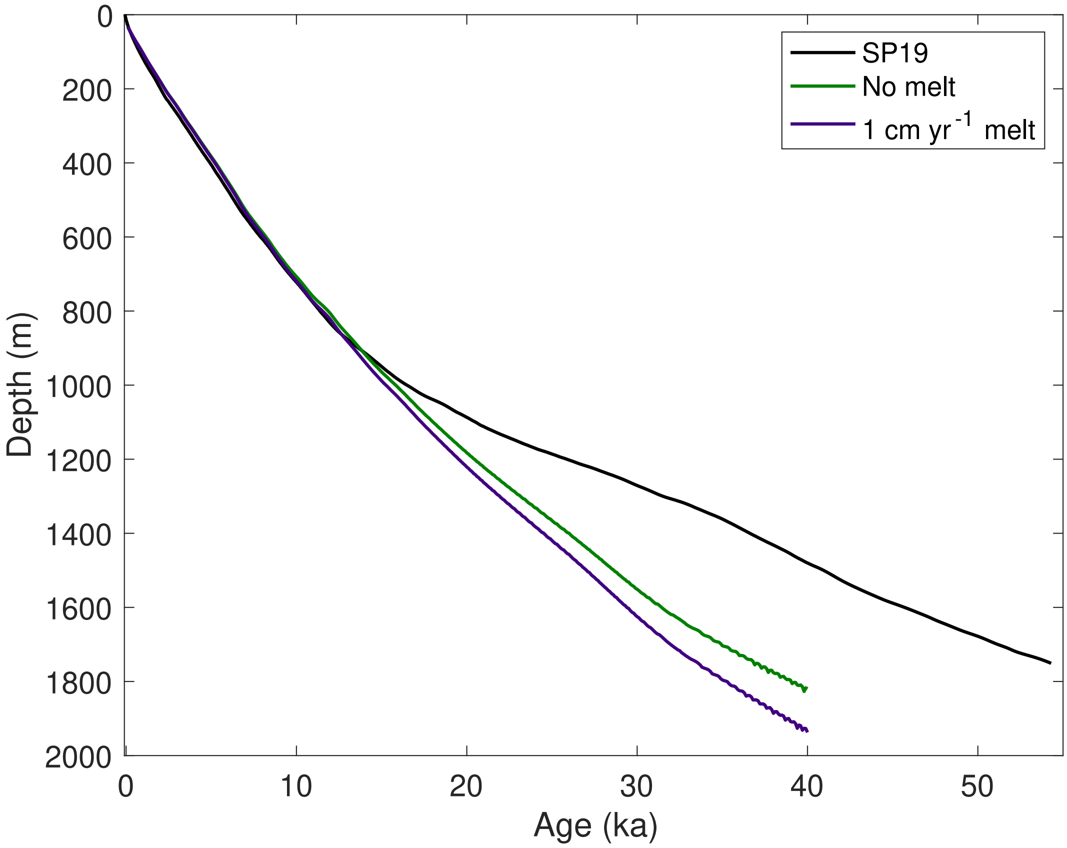


Figure S12: Comparison between modeled and measured depth-age relationship. The depth-age relationship from the steady-state models compare well to SP19 (Winski et al., 2019) for the Holocene. The divergence in the modeled values compared to SP19 values below approximately 900 m depth is due to the decrease in accumulation rate at older ages that we do not simulate with the steady-state model.

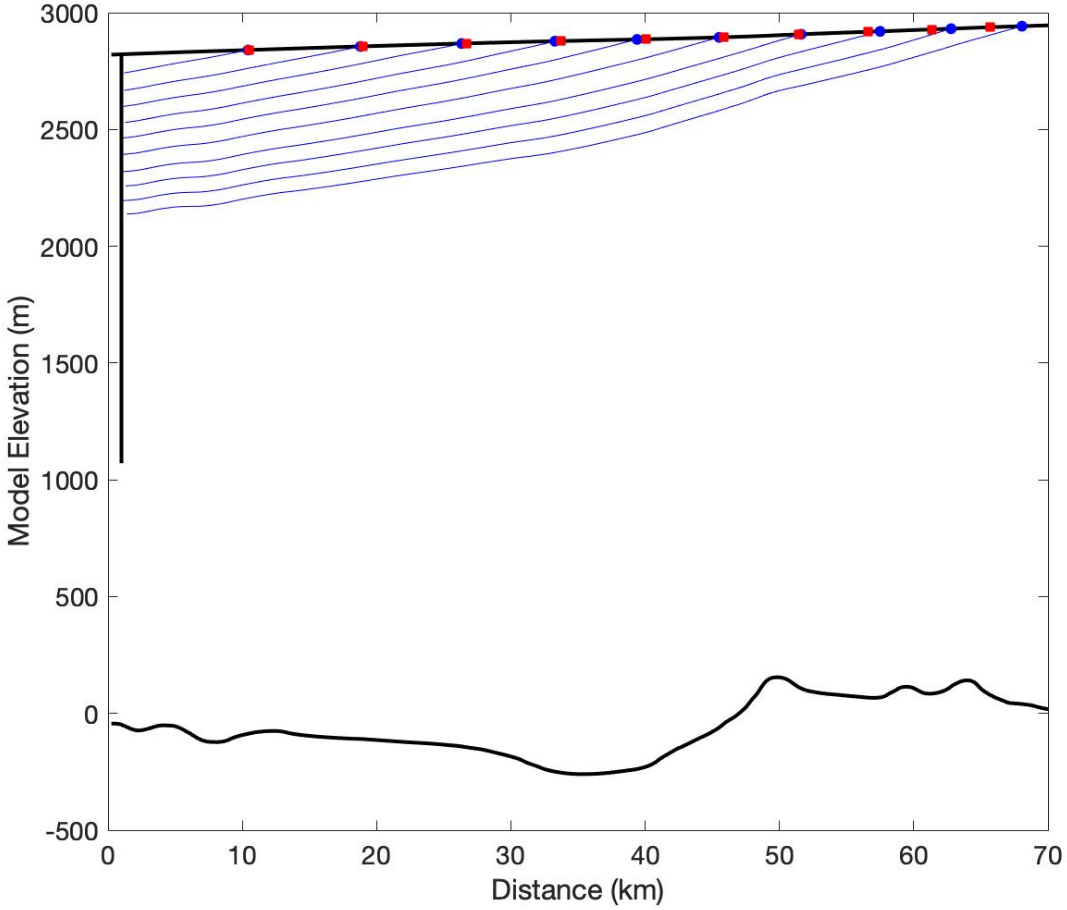


Figure S13: The origin location of ice parcels in 1 ka increments are shown in red squares for the reconstruction of Lilien et al. (2018) and the flowband model used in this study (blue dots). The blue lines are the modeled ice parcel paths. The black vertical line at 1 km represents the 1751 m deep SPC14.

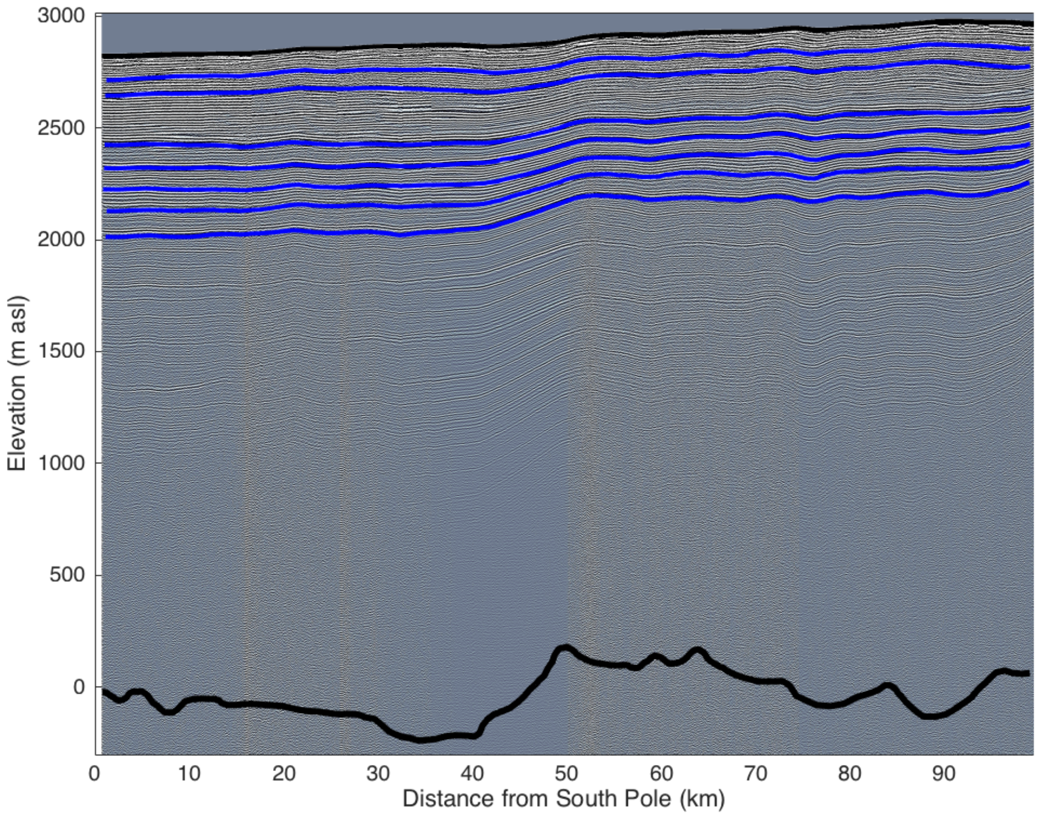


Figure S14: Radar profile along 100 km of the modern flowline upstream of SPC14 (see map, Figure S16). The data were imaged using a ground-based, bistatic impulse radar with center frequency of 7 MHz. The transmitter and receiver were towed inline behind a skidoo; each record consists of 1024 stacked waveforms and records were located using GPS. Reflection positions, measured as a function of radar two-way travel time, were converted to depth below the surface using a wave speed of 168.5 m $\mu s^{-1}$ in ice and 300 m $\mu s^{-1}$ in air. Wave speed in the firn was calculated using the density profile from SPC14 and a mixing equation (Looyenga, 1965) to estimate the depth profile of the dielectric constant. Solid black curves show the surface and bed elevations (m above sea level (asl)). Note that the SPC14 site is about 40 m below sea level. Blue curves are radar-detected internal layers (isochrones) that were dated using the SPC14 timescale. Layer ages with increasing depth are: 1020, 1900, 5070, 6510, 8070, 9690, and 11770 years.

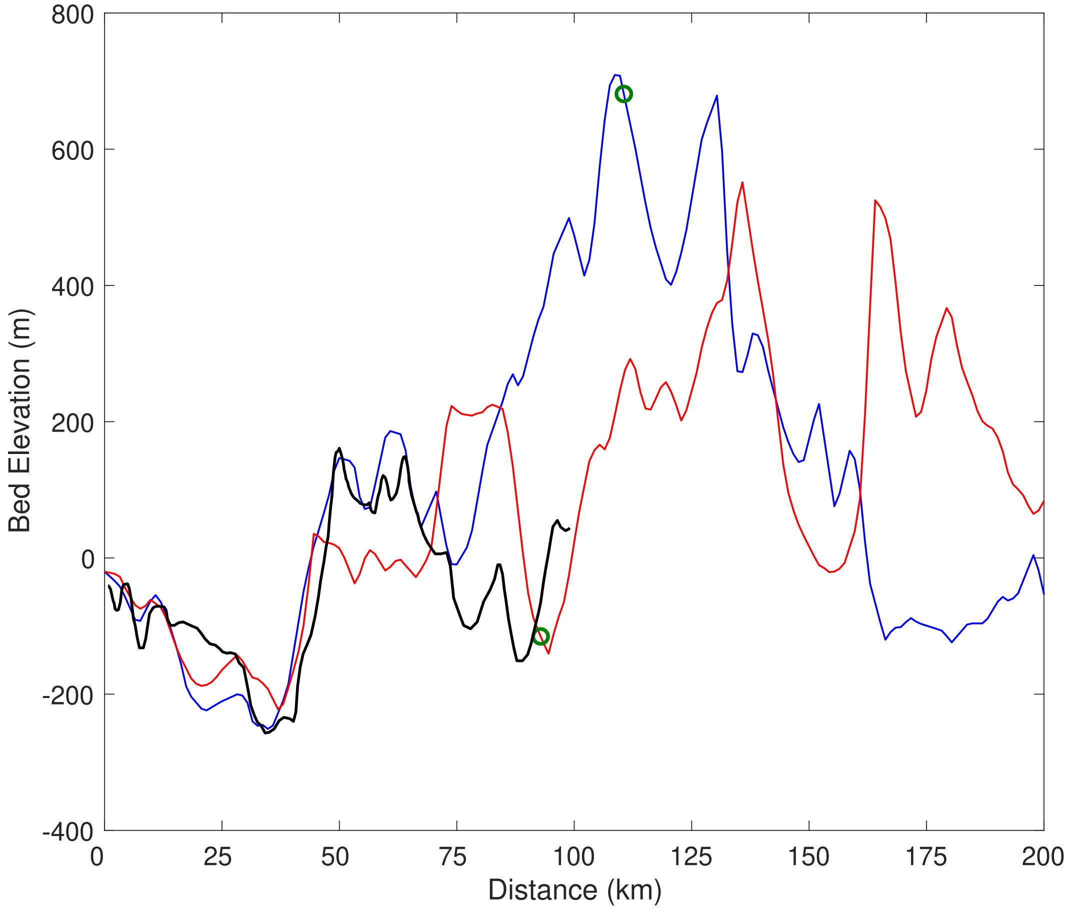


Figure S15: Profiles of bed topography upstream of the SPC14 site. Black is the bedrock measured along the modern flowline. Red is along 142.5° E and blue is along 135° E from the PolarGAP survey. Green circles mark the two points that we use to define a plausible bed feature to explain the thinning function for older ages (circles correspond to Figure S16).

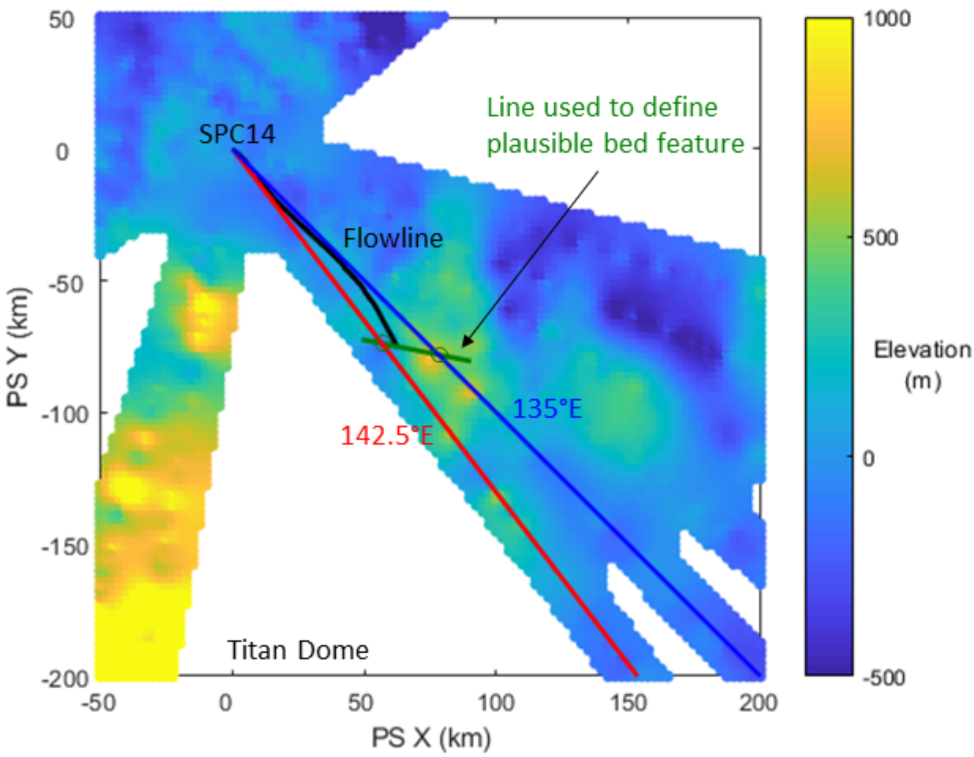


Figure S16: Map view of bed topography near SPC14. Black shows measured flowline. Red is along 142.5° E and blue is along 135° E from the PolarGAP survey. Green line shows the transect between PolarGAP lines used to guide the bed topographic feature beyond 100 km in the ice-flow modeling (circles correspond to Figure S15).

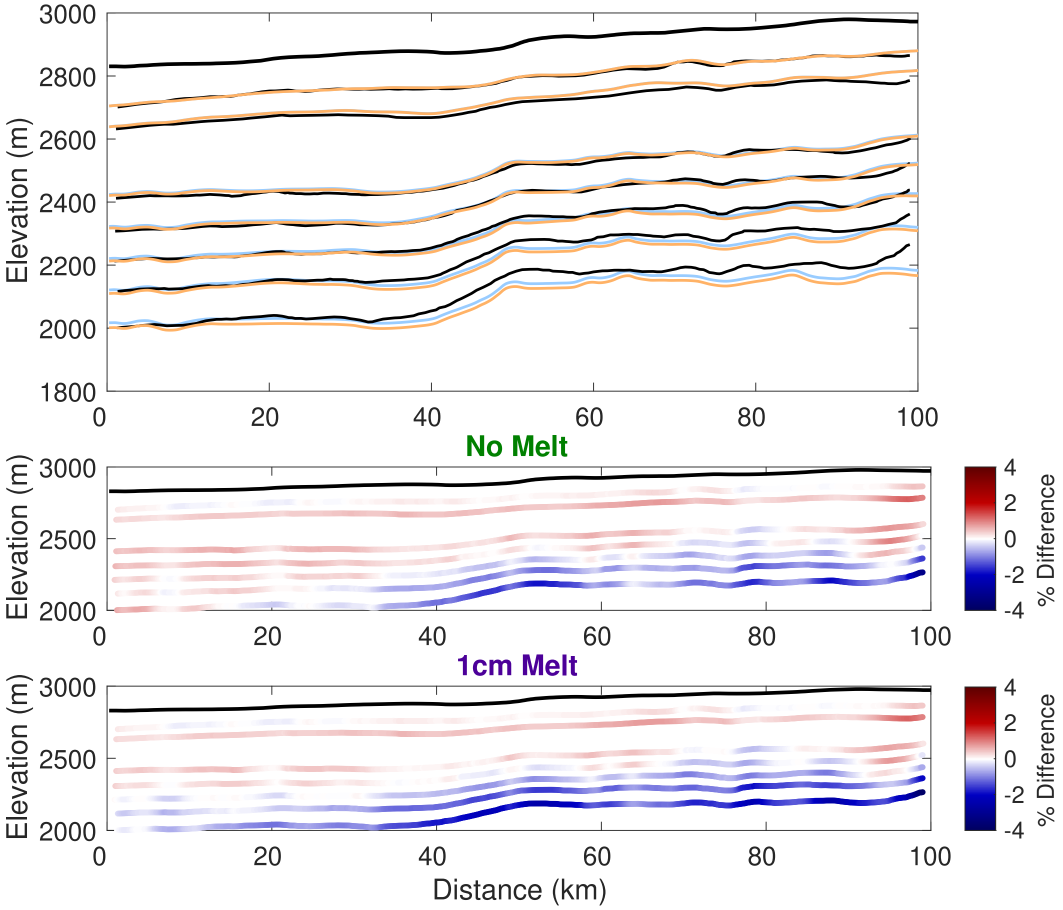


Figure S17: Comparison between modeled and measured internal layers in the flowband domain. Measured layers are shown in Figure S14. A) Observed (black) and modeled with no melt (blue) and 1 cm $a^{-1}$ melt (orange) internal layers. Observed layer ages are labeled. B) Percent misfit of layer depths for the "no melt" model. C) Percent misfit of layer depths for the "1 cm $a^{-1}$ melt" model.

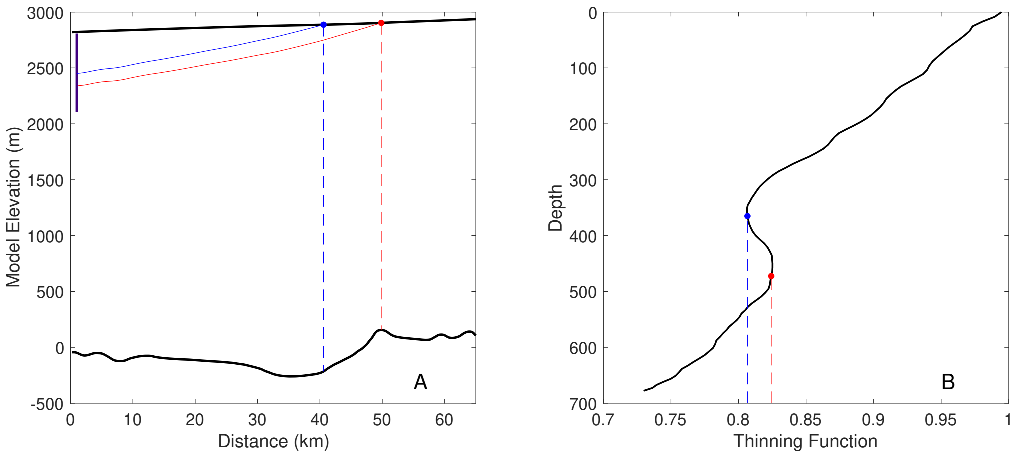


Figure S18: Illustration of the development of a reversal in the thinning function. A) Modeled particle paths with ice thickness (and corresponding bed elevation) at particle origin marked. Age of the red particle is ∼7 ka and age of the blue particle is ∼6 ka. Purple vertical line at the far left side is ice-core location and the depth of the core shows the depth range plotted in B. B) Modeled thinning function showing the reversal in thinning due to thickening of the ice sheet which the red particle experienced by the blue particle did not. The jaggedness of the thinning function is due to numerical challenges in the particle tracking.

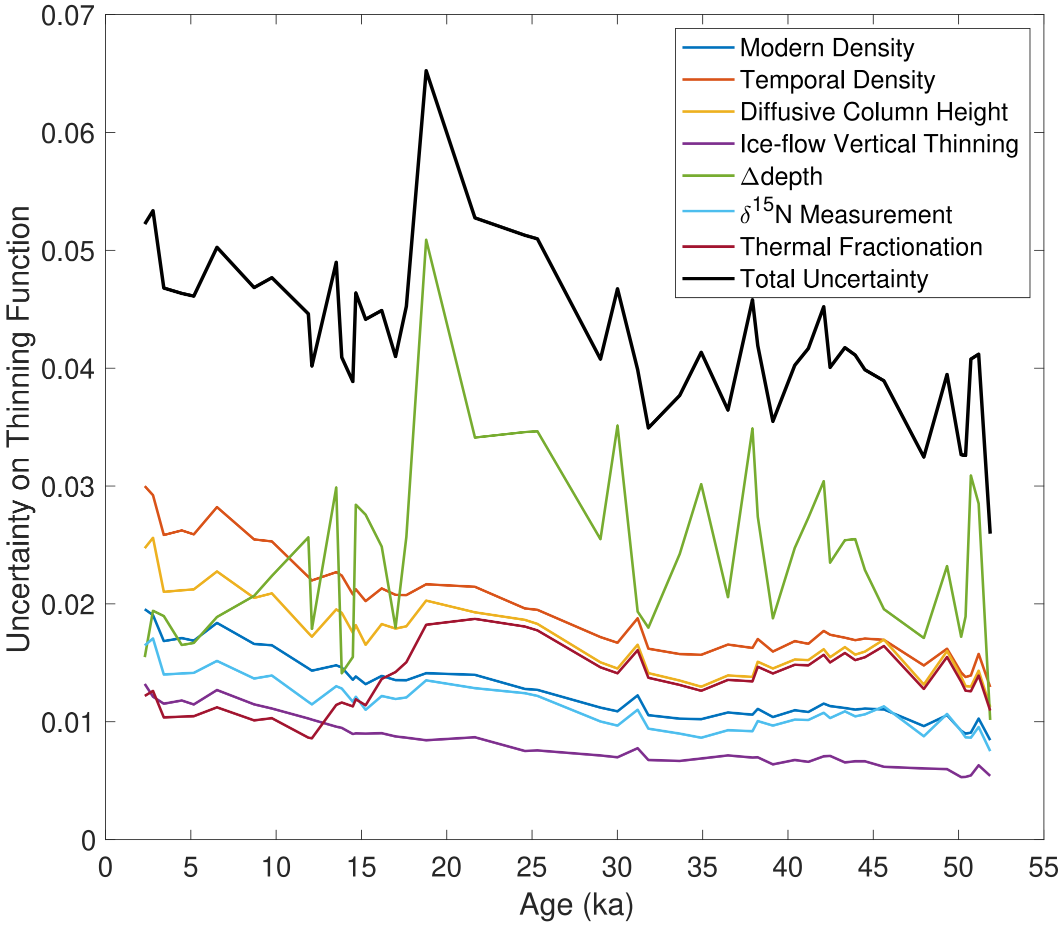


Figure S19: Uncertainty representing two standard deviations for the inferred thinning function from seven main sources described in Text S5.1.